UNIVERSITY OF THE WITWATERSRAND

School of Physics

Enhancement of Prompt Gamma Response for Treatment Planning Verification

Supervisor:
Dr. Luna Pellegri
Co-Supervisor:
Prof. Chiara La Tessa

Graduand:
Shanyn-Dee Hart

A dissertation submitted to the Faculty of Science, University of the Witwatersrand, Johannesburg, in fulfilment of the requirements for the degree of Master of Science.
2020-2021

Declaration

I, Shanyn-Dee Hart, declare that this dissertation is my own, unaided work. It is being submitted for the Degree of Master of Science at the University of the Witwatersrand, Johannesburg. It has not been submitted before for any degree or examination at any other University.

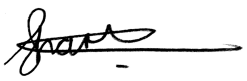

(Shanyn-Dee Hart)

23 March 2022 at Muizenberg, South Africa.

Abstract

In this project I present the results of a feasibility study on a novel strategy for real-time dose verification using secondary prompt γ-ray emissions produced by way of proton–nuclear interactions within selected materials during proton irradiation. To provide a proof-of-principle of this methodology, Monte Carlo simulations were performed using an approximately mono-energetic 70 MeV proton beam, irradiating different materials in salt and solution form. The choice of the target element is the key to obtaining a prompt γ-ray spectrum significantly different from the background produced by the human body, as well as for physiological considerations (such as uptake and toxicity effects). The promising candidates were: ^{63}Cu, ^{89}Y and ^{31}P.

I investigated the emission spectra of γ-rays exiting the target and assessed the enhancement of the γ-ray yield with respect to the background, comparing simulation and experimental results as conducted by the research group of the Trento University, Italy. I demonstrated how proton reactions with a solution containing the target elements can produce signature prompt γ-rays related to the material irradiated despite the significant background. The minimum material concentration required to obtain a significant enhancement was also studied.

The results show that the prompt γ-ray spectra differ significantly for each type of target studied. The relative intensity of the characteristic γ-rays emitted from a given solution containing the target elements was shown to be proportional to the concentration of each element in that material. Based on these results, I discuss the potential use of prompt γ-ray emission as a method to verify the accuracy and efficacy of doses delivered with proton radiotherapy.

Acknowledgements

I am pleased to express my great appreciation to my supervisor Dr. Luna Pellegri. It is thanks to her that I was able to pursue a research topic which is of great interest to me. It was her encouragement and incredible insight that assisted me in making key decisions during my work. I feel privileged to learn and grow under the supervision of such an inspiring mentor. Without her this project would not have been possible.

I would like to thank the research group at Trento University, with special thanks to my co-supervisor Prof. Chiara La Tessa, for their insight, guidance and infectious passion for the field of proton therapy. Further appreciation is due to Giorgio and Elena for their advice and friendship from afar. My MSc. has been a better experience for meeting them.

I would like to thank the Center for High Performance Computing (CHPC) for giving me access to their clusters and resources. This opportunity was invaluable as it allowed me to perform simulations I would not have otherwise had the computational power for.

I am incredibly humbled by my gratitude to the Southern African Institute for Nuclear Technology and Sciences (SAINTS), a division of iThemba LABS, who awarded me with a bursary to pursue this degree. This allowed me to focus on my studies by lifting the financial worries I would have otherwise encountered.

I would like to thank my mother for her loving support, patience and perpetual encouragement.

Finally, I would like to thank my partner, Peter, for his unwavering support, motivation and love. My life is made better by sharing it with you.

Contents

List of Figures

List of Tables

Acronyms

BP Bragg Peak

CTV Clinical Target Volume

CT Computerized Tomography

EM Electromagnetic

IC Ionization Chamber

IBC Intra-Binary Cascade

INC Intra-nuclear Cascade

LaBr Lanthanum Bromide

MC Monte Carlo

MCS Multiple Coulomb Scattering

NUDAT Nuclear Database of the NNDC

PT Particle Therapy

PBS Pencil-Beam Scanning

PDD Percentage Depth Dose

PET Positron Emission Tomography

RF Radio-frequency

TOF Time Of Flight

TPS Treatment Planning System

PTV Planning Treatment Volume

Chapter 1

Introduction

1.1 Aims

- To identify the candidate elements for the enhancement of prompt γ-rays in online treatment planning verification, specifically range verification. Proton induced reactions at tens of MeV are used to excite the nuclei and observe the relevant prompt γ-ray emissions and associated signature spectra.
- To develop a Monte Carlo model of the experimental setup for predictions regarding the prompt γ-ray spectra of the candidate elements, for comparison to final measured experimental results and perform an investigation into the physics behind the simulated results.
- To characterize the prompt γ-ray response of the background containing the most abundant elements in human tissue (^{12}C, ^{16}O and ^{14}N).
- To investigate the prompt γ-ray enhancement of these elements at different liquid concentrations to probe a more realistic therapeutic scenario.

This dissertation is composed of four main chapters. The first part is the Introduction (Chapter 1) which provides background information on the field of Proton Therapy (Section 1.2) and the various interactions of protons with matter (Sections 1.3, 1.4, and 1.5). Proton range verification and the associated sources of range uncertainties that emerge during proton therapy treatments are discussed in Section 1.6. The Introduction chapter outlines previous work performed in the field of prompt γ detection as well as the different methods employed in the field (Section 1.6.2). Details on the prompt γ method and the application in this research project are given in Section 1.7. Section 1.8 concludes the Introduction with a brief motivation for this work. Chapter 2 reports on the methodology and materials employed in the project which used a 70 MeV proton pencil beam. In

this Chapter the TOPAS Monte Carlo model developed for the prompt γ simulations is described in Subsection 2.1.5. The experiments as carried out by collaborators at Trento Proton Therapy Centre (Italy) are reported in Subsection 2.1.4, and post-processing of results is explained in Section 2.2. Chapter 3 presents the results of the research, where the simulation was validated by experiment. The first Section 3.1 reports on the main sources of background in the study: the $LaBr_3$:Ce detector internal radioactivity, and water and PMMA as human tissue equivalents. This is followed by the results of the solid target analysis in Section 3.2 and the liquid salt target results in Section 3.3 where analysis focused on the prompt γ performance of the targets at lowered concentrations. These Sections also determine the precision of the TOPAS simulations and make comparisons with the experimental data. In Chapter 4 the aims, brief methodology and overall findings of this study are concluded and attention has been drawn to ideas which may contribute to future developments in this work. The final part of this dissertation contains Appendices. Appendix .1 lists examples of codes employed in the TALYS (5) and TOPAS simulations conducted in this study. Appendix .2 provides prompt γ energy spectra for the various liquid target experimental and simulation results at different concentrations to further reference the findings presented in Subsection 2.1.3.

1.2 Proton Therapy

According to the World Health Organization (WHO) report, in 2018 cancer was the second leading cause of death globally, accounting for $\approx 17\%$ of all deaths, notwithstanding the numerous and significant developments gained in treating this pathology (10). Even if surgery was to remain the most effective treatment of solid cancer, a successful strategy combines several approaches.

The utilization of radiation has been proven most integral in the treatment of solid tumors, with over 50% of them being covered by radiotherapy. Commercial treatment facilities use X-rays, electrons, or protons to treat tumors. Proton Therapy (PT), a form of radiotherapy, is one of the most state-of-the-art methods to treat deep-seated tumors. The clear clinical benefit that ion beams provide over X-rays was first proposed over 70 years ago by the American physicist Robert Wilson, of which the first patent-based treatment was carried out in 1954 at the Lawrence Berkeley National Laboratory (LBNL), USA (11). He arrived at this end by combining the theoretical achievements of Hans Bethe, where he describes the energy loss protons and heavier ions experience when traversing a medium, with the technical developments of Ernest O. Lawrence, who pioneered the first cyclotron. Although heavier ions allow enhanced biological effectiveness when compared to protons, PT has emerged as the main ion beam radiotherapy, as Wilson proposed. This is largely due to the relatively lower cost of proton cyclotrons compared to heavier ion beam accelerators. Although relatively esoteric compared to the ubiquity of traditional photon-based radiotherapy centers, protons are a rapidly growing tool in the arsenal against cancer.

PT shares the same principle of causing damage and cell death in the diseased area as traditional radiotherapy, but with a remarkable difference due to the way charged particles and photons interact with matter. The energy deposition of radiation, known as treatment/integral dose, is measured in grays (Gy). PT can cause less damage to normal healthy tissue compared to other beam radiotherapy methods, such that it allows an increased dose to cancer cells while reducing the dose to the surrounding healthy tissues and organs at risk. This high dose conformity is due to a feature of charged particles where, to first order, the rate at which proton beams deposit dose in tissue is inversely proportional to the kinetic energy of the incident particle. Consequently, the dose delivery rate is at its minimum when the beam first enters the patient. This dose delivery rate then gradually increases as the tissue depth increases, the incident particles losing energy, culminating in the characteristic localized Bragg peak (BP), just before the beam stops (12). The typical beam energy employed in PT is in the range of 70 to 250 MeV, where higher energies are employed to reach the maximum depth of tumors which are encountered in clinical practice. PT owes its novelty to the existence of the BP as this characteristic provides a lot of flexibility in the shaping of the deposited dose distribution. The difference of the deposited dose distribution can be clearly seen in Fig 1.1(a). The depth of the sharp dose fall-off just beyond the BP, known as the beam range, is a function of the proton/ion energy used for the treatment. By precisely modulating the beam energy, clinical oncologists can determine the beam range such that the BP (where the highest dose is situated) is precisely delivered to the tumor region while important bodily components beyond the cancer are unaffected.

While there are major benefits to using radiation therapy for cancer treatment, there remain important problems. One of them is the absence of available methods to predict or monitor the proton depth-dose characteristics *in situ*. As a result, the clinical advantage afforded by the sharp distal fall-off in the depth dose profile of protons can not be fully exploited; an overestimate of proton path length could cause an undershoot of the beam, resulting in an incomplete tumor dosage and a decrease in tumor control probability, while an overestimate of the proton path length would cause over-dosages to healthy tissues. Uncertainties including Computerized Tomography (CT) artifacts, tumor shrinkage, and setup variations, are taken into account by adding a safety margin to treatment plans, *i.e.* enlarging the irradiated volume, which affects the clinical advantage of protons. Consequently, safety margins are applied in the Planning Treatment Volume (PTV) to ensure that the Clinical Target Volume (CTV) is effectively irradiated with the prescribed dose. In PT, such margins are typically 2.5 - 3% of the proton range 2 - 3 mm (13). For deep-seated tumors, this value sits at close to 1 cm. An accurate method of monitoring distal edge fall-off during treatment would help to maximize the dose to the target while minimizing damage to healthy tissues distal to the tumor. In addition, precise knowledge of the distal edge fall-off would allow clinicians to use gantry angles in which the proton beam points directly at a critical structure. Traditionally beam range uncertainties made such beam trajectories too risky to use on patients, but with confirmation of the BP position, range uncertainty would no longer present a problem (13).

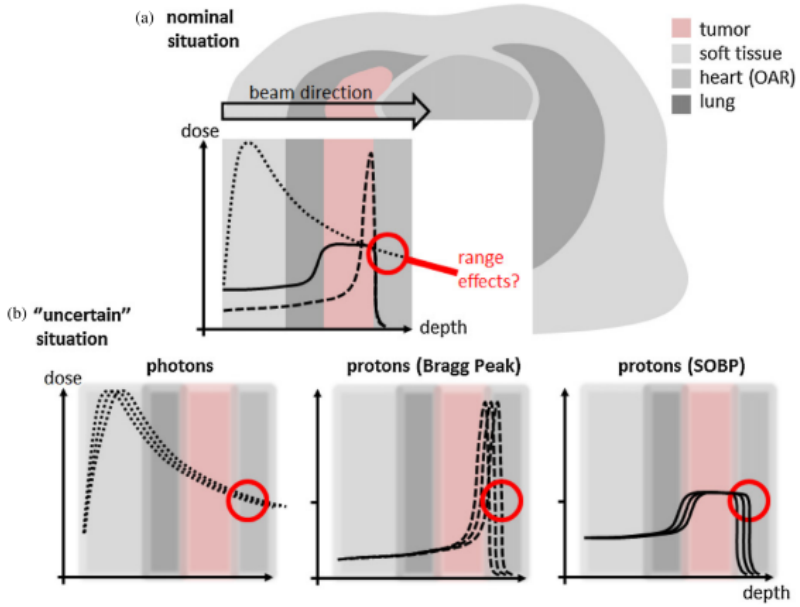

Figure 1.1: (a) Potential dose benefit of proton treatment compared to a photon treatment. The dotted line represents a photon depth dose curve, the dashed line represents a mono-energetic proton depth dose curve (known as the BP), and the solid line represents a spread out proton Bragg curve (SOBP) used to cover the whole tumour. (b) The influence of uncertainties on dose depth curves for the three treatments introduced in (a) (taken from (1)).

1.3 Energy Loss via Proton Interactions with Matter

Protons interact with the medium in three distinct ways (14):

1) **Scattering:** Electromagnetic scattering with atomic nuclei results in minute deviations of the proton from its initial direction. The observed angular spread of the beam in the medium from the central axis is caused by a stochastic combination of a very large number of small deflections. This theory is called *Multiple Coulomb Scattering (MCS)*. MCS is the significant effect of Coulomb interactions with atomic nuclei whereby incident protons travelling near enough to the atomic nuclei are deflected by electrostatic forces as a consequence of both carrying a positive charge. These primary protons are also deflected by inelastic collision directly with the nucleus. The contribution of MCS to the width of the BP has been found to be $\approx 2\%$ of the range of the BP in water (15).

2) **Nuclear Interaction:** There is a finite, however small, probability that primary protons will interact directly with atomic nuclei through nuclear interactions (see

Section 1.5 for more details). There are three categories whereby nuclear interactions may be classified according to the time-scale in which each reaction type occurs: compound, direct, and pre-equilibrium reactions. In compound reactions, the projectile and target nucleus fuse to form a compound nucleus which decays via emission of neutrons, charged particles (fragments) and/or γ-rays in relation to the excess energy/angular momentum present in the system. Direct reactions are distinguished by their very short time scale, allowing for the interaction of only few nucleons. In these direct reactions, no intermediate compound nucleus is created. As such, the nucleons involved in the reaction can experience no change in their internal states (elastic scattering), become excited or transfer a few nucleons between the target and projectile. The third type of nuclear reaction, pre-equilibrium reaction, is identified by its immediate time scale where the cascade particles have reached a lower energy limit, but where the nucleus has not yet reached thermal equilibrium. The residual nucleus is left in an equilibrium state due to the emission of fragments and the nucleons which remain share an excitation energy. These three types of interactions are not mutually exclusive, whilst their respective importance is dependant on the incident beam energy. Compound reactions tend to dominate in cases of low-energy proton beams ($\approx$ 10 MeV). As the incident beam energy is increased, more reaction channels open up. By and large, a total nuclear reaction may encompass a sequence of residual excited nuclei which originate from multiple particle emissions. The ensuing γ-ray decay is a characteristic of the properties of these residual nuclei, such as parity of the populated level, spin, intrinsic nuclear structure, neutron separation energy, etc. Short-lived radioisotopes can be created, where the production of such isotopes by proton irradiation can be directly used to deduce particle range *in vivo*. These nuclear reactions constitute the main source of secondary particles, such as γ-rays and neutrons.

3) **Stopping:** The charged particle nature of protons causes direct participation with the medium it travels through, ionization which eventually causes stopping. This is due to the inelastic scattering of protons with orbital electrons via electromagnetic interaction, where the incident proton loses more energy with each interaction until it comes to a stop. The point at which this occurs is not the same for all of the particles: the stochastic nature of a massive number of interaction collisions causes some protons to be stopped prior to, or after others. This phenomenon is known as energy straggling. Since these interactions are predominantly governed by Coulomb interactions, the energy loss is continuous and its rate increases as the depth of penetration increases.

   In a medium with density ρ, energy loss per unit path length due to Coulomb interactions are described by the stopping power $S(E)$ of charged particles with energy E, and it is formalized in the well-known equation, the *Bethe-Bloch* formula (for charged particles with masses much larger than the electron mass m_e) (1):

$$S(E) = 4\pi\rho\frac{Z}{A}N_A\Big(\frac{e^2}{4\pi\epsilon_0}\Big)^2\frac{z^2}{m_e v^2}\Big\{ln\Big[\frac{2m_e c^2}{I}\Big]+ln[\beta^2]-ln[1-\beta^2]-\beta^2-\frac{C}{Z}-\frac{\delta}{2}\Big\} \quad (1.1)$$

Where Z is the target proton number, z is the projectile charge, ρ is the density of the absorbing material, C is the shell correction, N_A is Avogadro's number, δ is the density correction, ϵ_0 is vacuum permittivity, v is the projectile initial speed, I is the mean ionization potential of the target, and β is the relativistic velocity of the projectile. From Eq 1.1, the stopping power dependency on the particle and the target can be studied independently:

- $\frac{S}{\rho} \propto \frac{z^2}{m_e v^2}$: The mass stopping power is proportional to the charge squared of the projectile and inversely proportional to its kinetic energy. When the particle stops, the maximum energy is released to the absorbing material.
- $\frac{S}{\rho} \propto \frac{Z}{A} N_A$: The projectile releases energy dependent on the characteristics of the target investigated.
- $\frac{S}{\rho} \propto ln\left[\frac{2m_e c^2}{I}\right]$: The mass stopping power is also weakly dependent on its mean ionization potential due to the logarithmic function.

The mass stopping power is related to the dose simply by a unit conversion:

$$D\ [\frac{J}{kg}] = \Phi\ [\frac{1}{cm^2}] \cdot \frac{S}{\rho}\ [\frac{J \cdot cm^2}{kg}] = 6.242 \cdot 10^9 \cdot \Phi\ [\frac{1}{cm^2}] \cdot \frac{S}{\rho}\ [\frac{MeV \cdot cm^2}{g}] \quad (1.2)$$

where Φ is the proton beam fluence.

The Bethe-Bloch equation, together with the statistical nature of MCS for protons, leads to the tell-tale depth-dose curve with its low entrance plateau and steep distal curve known as the BP.

1.4 Bragg Peak

Figure 1.2 demonstrates the correlation between the deposited-dose depth profile and the secondary vertex distributions due to inelastic interactions of the primary beams. The probability of interaction increases with penetration depth and the decreasing energy of the primary particles such that a correlation between dose and prompt prompt γ-ray vertices is observable, where the highest yield of prompt γ-rays is seen around the BP region.

PT is based on the characteristic behaviour of the energy deposition curve that is illustrated in Fig 1.2. This curve can be divided into three defined regions [1]:

[1] All charged particles deposit their energy in matter following the behaviour of the BP, whose features are independent of ion species and absorbing medium.

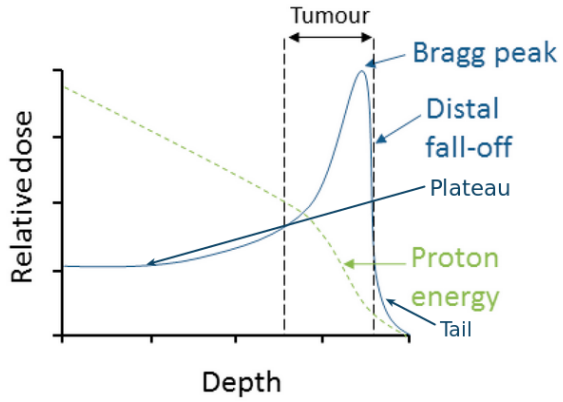

Figure 1.2: Labelled schematic representation of proton percentage depth dose regions of the BP adapted from (2).

- **Plateau:** The entrance region sees a nearly constant proton delivered dose due to the nature of stopping power at high energies. There is a low statistical probability here of ionisation events by primary protons, therefore these interactions are dominated by low-energy target fragments (16). Within the first few millimeters of the beam entrance, nuclear build-up occurs where the dose increases until it reaches the saturation point. After the first few millimeters, nuclear equilibrium [2] is reached, seen as the range of secondary particles.

- **Steep Distal Curve:** The cross section of nuclear interactions increases in the BP region, where the biological effects of this interaction are overshadowed by the ionization of primary protons. The maximum dose occurs at the stopping point of the protons. Range straggling results in the narrow width of the BP due to mono-energetic protons being only a few millimeters wide. The steep distal fall-off of the dose occurs once all of the protons have stopped; the difference between the range at which the dose is at 80% (R80) and 20% (R20) quantifies the dose fall-off beyond the peak and is known as the Distal Penumbra. This peak-to-plateau ratio is dependent on the size of the beam spot, as MCS deviates the protons in the transverse plane. This MCS results in a decrease in the proton fluence along the central axis causing a decrease in the peak-to-plateau ratio. This characteristic must be taken into account when the dose along the BP is measured, as one can use detectors much larger than beam size, even at end of range.

- **Tail:** When heavy ions (such as ^{12}C or ^{16}O) traverse matter, nuclear reactions occur producing secondary particles. These secondaries have a charge dependent on the intrinsic characteristics of the projectile and target nuclei. Resulting fragments from the target and projectile can release dose after the BP, where projectile fragments are

[2] The number of particles entering in a unit volume are compensated by other particles going away from it.

scattered at approximately the same energy as primaries in an abrasion process (17). As the mass stopping power is proportional to $\frac{Z_{eff}^2}{\beta^2}$, the range of secondary lighter fragments is larger than that of the primary beam, causing them to contribute to the tail dose. For a proton beam, the tail dose is negligible since the proton cannot fragment into other nucleons (18).

1.5 Nuclear Interactions of Protons

As highlighted in Section 1.3, charged particles can undergo collision directly with the nuclei of the material they are passing through. Even if these interactions give only a small contribution to the total amount of energy loss compared to electromagnetic interactions, they can be very important to range verification. Nuclear interactions can take the form of elastic or inelastic collisions. In elastic collisions, kinetic energy is conserved and the nucleus remains intact, and are thus not of interest here. This is similar to MCS, but due to the strong nuclear force as opposed to EM interactions. However, the nuclear reactions of interest between the incoming ions and the target nuclei are presented below.

- **Compound Nuclear Reaction:** A compound nucleus is formed as a combination of the target nucleus and the incident proton when the incident energy of the proton nuclear interaction is sufficiently low (10 - 20 MeV). While the probability of a compound nuclear interaction occurring is high at low energy, it is important to note that it is still possible at higher energies. The incident proton abides within the target nucleus, creating a *compound* nucleus, and the energy of the incoming proton is redistributed to all the nucleons of the system. Compound nuclei exist in an intermediate state after the integration of the incident particle and before the emission of outgoing particle(s). The energy of the outgoing particle, emitted by the compound nucleus, is the sum of the center of mass energy and the Q-value of the reaction. This reaction is represented symbolically as:

$$a + X \rightarrow C^* \rightarrow Y + b \tag{1.3}$$

Where a represents the projectile, X the target, C_* is the compound nucleus, Y is the reaction product, and b the outgoing particle(s).

A compound nucleus can form through various reaction processes and decays through many different channels. This compound nuclear model applies to medium and heavy-weight target nuclei, such that the interior of the target nuclei is large enough to absorb the incident proton. Particle emissions due to a compound nucleus are approximately isotropic because of the randomised interactions amongst the nucleons within the target nucleus. Emissions occur in $\approx 10^{-16} - 10^{-18}$s after the initial reaction. The decay probability of a compound reaction depends solely on the total

energy given to the system. This means that the compound nucleus essentially forgets the formation process and the decay is primarily controlled by statistical rules.

- **Direct Reactions:** Direct reactions become more probable with an increase in projectile energy (> 20 MeV). Here the incoming proton will interact with just a few of the target nucleus, after which the target nucleus can be left in its ground state/excited states or acquire/lose particles. The particle emission from a direct reaction occurs much faster than from a compound-nuclear reaction. Emissions occur in $\approx 10^{-22}$s. For this reaction type the distribution of the emitted particles is strongly related to the type of reaction.

- **Pre-equilibrium Reactions:** Pre-equilibrium reactions can be defined as intermediate reactions between direct and compound nucleus reactions. The emitted secondaries have a high energy, and specific angular distribution. As the pre-equilibrium reaction comes to an end, there is a chance that a single nucleon may have enough energy to escape an excited composite nucleus, known as an evaporation process (such as the escape of molecules of hot water).

1.5.1 Overview of γ Decay:

During PT treatment, the interaction of the proton beam with the patient's body generates a wide spectrum of charged and neutral secondary particles emitted at different energies and angles with respect to the primaries. There is a likelihood that the passage of the primary beam in the target tissue will create nuclear excited states which de-excite rapidly via the emission of γ-rays. These photons are often referred to as prompt γ-rays, where the term prompt is associated with the time scale of their production in the range of nano-picoseconds.

γ radiation is emitted when excited nuclei transition to lower-lying nuclear levels. The decay of a parent nuclide is often what creates these excited nuclear states in daughter nuclides or fragments which have short average lifetimes (which are often in the order of nano-picoseconds). This de-excitation occurs through the emission of a γ-ray whose energy value is equivalent to the energy difference between the initial and final states. The γ-rays thus appear with a half-life which is characteristic of the decay of the parent but the daughter energy mirrors its own energy level structure. An example is seen in Fig 1.3 where the ^{60}Co γ-rays decrease in intensity due to the 5.26 year characteristic half-life, they in fact arise from the ^{60}Ni nuclear transitions. The probabilities of the different de-excitation branching ratios in the decay schemes of different materials give insight into the number of γ-rays which are produced per disintegration of the parent nuclide.

Due to nuclear states having associated characteristic energies, the energies of the emitted γ-rays in these state-to-state transitions are well defined and are nearly monoenergetic. This is interesting as it means that when calibration sources (such

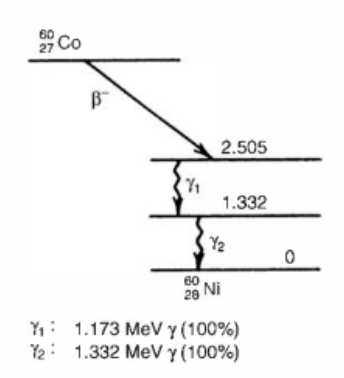

Figure 1.3: Decay scheme for the major γ-ray transitions of ^{60}Co where the disintegration energies and yields are indicated below (3).

as ^{60}Co which has been employed for that purpose in this study) are used to measure detector response, the value is indicative of the detectors' own resolution and not a variation in the incident γ-ray energy. An exception to this occurs if the emitting nuclei are of high velocity. In this case the Doppler effect can introduce an energy spread which could be significant in detectors with a good energy resolution. This is due to processes populating the high-lying nuclear states. Here the product nucleus is left in an excited state with a lifetime so short that the recoil nucleus does not have time to come to a rest before the γ-ray is emitted. This results in the resulting γ-ray energies being broadened by Doppler effects which is dependent on the orientation of the recoil velocity and γ-ray direction and which results in an energy spread of $\approx 1\%$ in the γ-ray energy (3). The underestimation of this effect in the simulated background sources is a contributing factor in this study, described in Section 3.1.

1.6 Proton Range Verification

The advantages of using protons in cancer therapy can only be fully exploited when the proton beam range in patients can be accurately predicted in the treatment planning and delivery. These ranges should be reliable in terms of both absolute value and spatial distribution inside the body. Improper quantification of the beam safety margins can outweigh any potential advantages of the technique and result in severe consequences, more so than photon therapy (13). Under-dosage of the tumor, due to a shift in the BP position, can result in healthy tissue and organs being irradiated which can cause secondary effects in time such as further malignancies. For this reason an accurate and reliable determination of penetration depth in PT is of the highest importance. Prompt γ-ray detection has the unique potential advantage of offering range verification in real-time, with just a few millimeters precision for the scale of a single proton pencil-beam spot (19). The high energy prompt γ-ray spectrum is partly induced by secondaries, where the

reconstruction of the prompt γ-rays emission point is related to the BP position, providing an online (methods which can be performed during, or immediately before treatment delivery, also known as *in vivo*) dose monitoring of the treated tissues.

The ideal beam range in the patient should be equal to the value prescribed by the Treatment Planning System (TPS). The TPS is at the heart of PT and is designed to improve patient outcomes, but indeed there are significant uncertainties at the time of irradiation. These arise due to anatomical differences between patients, anatomical body alignment, beam delivery, and dose calculation (13). The values of the safety margins are clinical protocol, therefore decreasing these uncertainties would reduce the safety margins, *i.e.* the treatment volume, and result in a superior sparing of the healthy tissue. This translates to having patients that are less predisposed to suffer post-treatment complications, making them more likely to be healed of the malignancy.

To lessen the effects of beam range uncertainty, with a focus on the tumor receiving the entire prescribed dose, safety margins in the form of an added thickness of tissue around the cancer margins are included in the TPS target volume. Range uncertainties vary between treatment centers but are generally seen to be $\approx$3.5% of the proton beam range plus an additional 2 mm, with more conservative margins implemented near critical organs (13). At this time, two principal options for proton range monitoring are undergoing development by several groups worldwide: Positron Emission Tomography (PET) and Prompt-γ Imaging. Beam range uncertainty can be attributed to two main treatment categories: planning and delivery.

- **Treatment Planning:** Prior to a patient beginning a course of cancer radiotherapy, a treatment plan is developed based on a specialised simulation known as a computerized tomography (CT) scan, coupled with other diagnostic images. These results allow radiation oncologists to accurately determine the tumor margins and to plan the treatment approach. This plan generally involves orientating between 2-4 particle beams in the direction they are intended to deliver a certain calculated dose. Uncertainties appear in the accuracy of the calculations required of the treatment plan. The exact range of treatment beams necessary to cover the entire treatment volume and the beam energy needed to produce that range can be affected by noise and CT scan image distortions. Further uncertainties are introduced in the composition and density values of patient tissues and the limitations of the algorithms relied upon to determine the dose delivery rates of the beam in various tissues.
- **Treatment Delivery:** The delivery of the treatment poses its own uncertainties. Ideally, a treatment plan is most effective when a patient is fully immobilized and positioned on the treatment seat in an exact replicate of their positioning in the CT image. Problematically, patients may shift position during the treatment, which can span several minutes from alignment to end of treatment (20). As such, the alignment and positioning of the patient for every treatment is controlled by a robotic couch and an onboard X-ray or CT imaging system to ensure that patient bodily landmarks

are aligned as in the treatment plan. This is not possible to reproduce exactly as the imaging capabilities of these systems are limited in both contrast and resolution. Another limiting factor is that over the course of an $\approx$ 30 day treatment, patient anatomy is susceptible to changes in weight, tumor shrinkage, or swelling of the normal tissue.

1.6.1 Positron Emission Tomography

PET has been around for decades and was the proton range verification method first applied in clinics, forming a staple in the field of diagnostic radiology. PET consists of imaging the decay of positron emitters created during the fragmentation of target nuclei (in any type of PT), or of the projectiles themselves (such as carbon or heavier ion therapy). These positron emitters are created when proton-rich nuclei convert a proton (p) into a positron (e^+), neutron (n), and a neutrino (ν), plus kinetic energy for the neutrino and the positron: $p^+ \rightarrow e^+ + n + \nu$. Two 511 keV annihilation photons travelling anti-parallel to one another are created when the positron annihilates. It is these back-to-back photons (known as PET photons) that are detected during the PET imaging technique (21). The link between the β^+ emitters production yield and the BP position allows reconstruction of the irradiated region by measuring the PET photons emission distribution, a method which has been applied to both protons and carbon ions treatments.

The PET scanner for use in range verification was first proposed by Maccabee *et al.* (1969) (22) and is only able to clinically implement post-treatment verification (23). Online verification using this method is limited due to the long half-lives of the reaction products ($\approx 1 - 20$ min) such that PET cannot truly be considered an online tool but rather an *a posteriori* verification (21). Parodi *et al.* (2007) (24) investigated the use of the PET scanner in post-proton treatment range verification. Limitations include image quality (number of emitted positrons limits the resolution), blood perfusion, and internal organ motion and tissue composition as in PT the production of positron-emitted isotopes is sensitive to the elemental composition of the tissue. The method does show good spatial reproducibility of the measured activity distributions (within 1 mm), however, the range can only be verified with an accuracy of $1 - 2$ mm in the most optimistic situation with low blood-perfused bony structures of the head-and-neck region and an accurate reproduction of the TPS position (24). Contrariwise, in soft tissues the blood-perfusion causes biological washout of the positron-emitted isotopes, which presents a difference between the measured and predicted spatial accuracy (up to 10 mm) (23). It is due to these reasons that the PET/CT method is seen as insufficient in range verification. Thus far, it is the sole method that can be used as an *in-vivo* proton range verification device pending a more precise method is developed (25).

1.6.2 *in vivo* Prompt γ Detection

The detection of instantaneous prompt γ-ray emissions has been put forward as a reliable alternative to PET as a means of range verification (26). Recent development in research of *in vivo* beam range verification methods focused predominantly on secondary prompt γ-rays and delayed γ-rays produced by the mechanism of inelastic proton-nuclear interactions within the patient. Prompt γ-ray radiation, typically of a few MeV energy (from 1 - 2 MeV up to about 7 MeV), has the advantage that it is produced instantaneously (picosecond (ps) time scale), and penetrates the tissue easily, mostly without any interaction on its way out. For this reason, the location of the prompt γ-ray origin is not distorted, allowing for the BP position to be pinpointed. The correlation between the different secondary particle emission vertex distributions (resulting from inelastic collisions for the instance of protons) and the deposited-dose depth-profile is illustrated in the Geant4 simulation in Fig 1.4 (4). One observes a clear correlation between the prompt γ-ray emission vertices and the deposited dose, although few prompt γ-rays are released by secondary particles such as neutrons. Figure 1.4 shows a correlation between the vertex distribution of neutrons and the depth but this information on the emission location will be obscured by scattering in the target before detection. There exist many approaches which exploit the different properties of prompt γ-rays: energy, temporal or spatial distributions. These approaches all share the common environmental constraints in which the setups must operate. prompt γ-ray detectors have to be compact and transportable to be placed in the room for treatment as online verification, as the prompt γ-rays are instantly generated.

All methods are required to detect the high energy prompt γ-rays which calls for the development of novel detector systems not unlike those invented for fundamental nuclear physics. The emission of prompt γ-rays remains, since proposed by the first study as mentioned, the most direct and real-time monitoring method of the BP position. Many studies have been performed which focused on identifying the prompt γ-ray emission in terms of its energy, abundance and associated angular distribution (27). Spectroscopy studies show that prompt γ-ray emission induced by proton bombardment of the target revealed a number of characteristic signature γ lines originating from the specific elements which interacted with the incident protons in the target. These reactions occur immediately during irradiation and are continuously emitted along the beam line where most of the prompt γ-rays accumulate in the BP region with highest cross sections. These distinct peaks provide a wealth of information that not only benefits *in vivo* beam-range monitoring but which can be employed in determining the concentrations of specific elements within irradiated tissues in PT treatments (28).

The various prompt γ-ray range verification techniques fall into two groups: imaging and non-imaging methods.

1. **Imaging Techniques:** Imaging techniques intent on range verification by analysing the spatial distribution of the prompt γ-ray vertices. This can be performed in up

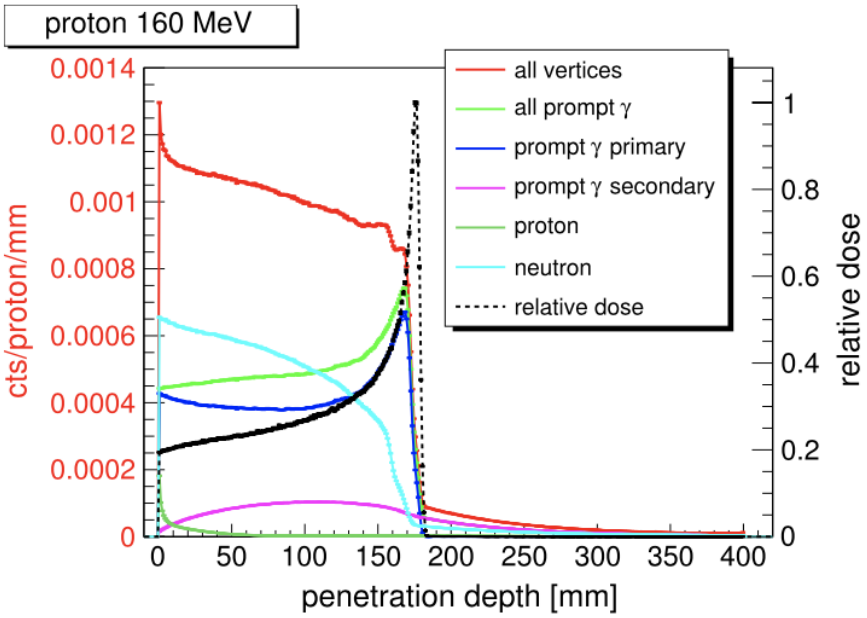

Figure 1.4: The relative vertex distributions produced by secondary radiation due to a 160 MeV proton beam incident on a water phantom target (diameter: 15 cm, length: 40 cm. These emission point vertices are scored upon the particles (energy > 1 MeV) emerging from the target surface. The longitudinal component of the dose distribution is also shown in black (4).

to three dimensions and depends on the intricacy of the detector setup and analysis.

Knife-edge slit-camera (KES): A slit shaped camera is the analogue of the common pinhole camera but with the advantage of producing one-dimensional (1D) imaging. Based on the above observations, the proton range can be monitored by examining the 1D intensity of the prompt γ-ray distribution along the beam depth using a novel mechanical collimation detector system (29) (30). The collimation setup was improved by J. Smeets *et al.* (2012)(31) by the introduction of a KES γ camera for the 1D prompt γ-ray distribution, a device which has been tested clinically on a patient with brain cancer and showed high range verification accuracy (1 - 2 mm standard deviation on proton pencil beam range estimation). The Dresden group in collaboration with IBA Group and OncoRay presented the first worldwide test of the slit-camera in a clinical setting during patient treatment (32). In this setup the camera was fixed to a mobile trolley for easy transport. The camera was made up of tungsten collimator with a knife-edge shape and an arrangement of 4 mm wide LYSO scintillating strips which were read out by silicon photo-multipliers. Variations in inter-fractional range by a passive scatter proton beam were the focused on and

were determined to be accurate to ±2 mm. The first clinical trial where prompt γ-ray range verification was employed throughout the treatment was performed with another KES prototype using pencil-beam scanning conditions (33). The results were astounding, where 6 fractions performed in brain treatment revealed that the range verification offered precision which was more accurate than the safety margins applied in TPS. Ready *et al.* (2016) (34) employed many knife-edge slits in the collimation setup which formed a two-dimensional (2D) pattern and, thus, 2D imaging detector using a position-sensitive LFS detector. This technique is not yet robust and encountered limitations regarding unrealistically close collimator distance (8 cm) with respect to treatment scenario distance, as well as beam energy.

Multi-slit camera (MPS): The MPS is a generalization of the slit-camera but which aims at extending the field of view. Experiments were performed by Smeets *et al.* (2016) (35) which, with beam energies of 100, 160 and 230 MeV, compared the performance of two collimated setups: one with a MPS and the other with their KES of the same weight and parallel slits. The KES allows for a smaller range of view and imaged only the BP region, while the MPS extended its image to the beam entrance point. In terms of statistical precision and range retrieval, the MPS required double the dose used by the KES to obtain the same statistical precision such that the authors concluded that further development would be needed for the more favourable KES.

Compton camera (CC): CC provides a direct three-dimensional (3D) reconstruction of the prompt γ-ray emission induced by irradiation. It is composed of scatterer and an absorber modules. The performance is dependent on the detection of impinging γ-rays that undergo Compton scattering in the scatterer module and then absorbed via the photo-electric effect in the absorber module. A cone of impinging γ vertices is reconstructed by registration of the γ hit positions and associated energy depositions. Tracking of the Compton scattered electron allows for further constraint to the cone. The camera image is formed by a superposition of these reconstructed Compton cones. This image, although 3D, is known to have a poor resolution normal to the detector front face but that can be remedied by using two CCs which are situated at perpendicular to the target on alternate sides.

2. **Non-Imaging Techniques:** The second technique type in beam range verification employs non-imaging techniques. These exploit the correlation between the beam range and the temporal or spectral characteristic features of prompt γ-ray emission (19).

Prompt γ-Ray Timing (PGT): A novel concept was proposed by Golnik *et al.* (36) which made use of range assessment by PGT. This is based on the certainty that ion transient time in a patient before stopping is dependent on the proton range. It

is only during this time what prompt γ-rays are produced. The excited nuclei have lifetimes which are shorter than the prompt γ-ray transient time, therefore the time of flight (TOF) distribution of the prompt γ-ray detection relative to the incident protons is also correlated to the ion range. This method is most easily approached by use of a fast detector where the direction is backward to make the TOF of the ion and the prompt γ-ray additive, as well as to make the signals of the detector and accelerator high frequency synchronous to create a stop for the TOF measurement. The difficulty is in adapting the time calibration for each change in beam energy. Another limitation is in the width of the beam pulse because the time distribution is a result of the individual ion transient times with the pulse width. Particularly, this cannot be done with long-lasting pulses delivered by synchrotrons. By taking the distribution of the elapsed time between the two signals, called the PGT spectrum, the proton range can be determined by comparison to the PGT spectrum as modelled in simulation. This setup does offer advantage in terms of simplicity.

Prompt γ-Ray Peak Integrals (PGPI): The aforementioned PGT method exploits the mean and width statistical values of the timing distributions. Krimmer *et al.* (2018) (4) investigated adding peak integrals to those features, and relaxing the time resolution constraints to 1-2 nanoseconds (ns). This allows detection of only the prompt γ-rays emitted within patient tissue, eliminates prompt γ-ray contribution from the beam nozzle and the neutron-induced background. The range verification precision was calculated as 3 mm for a proton pencil-beam.

Prompt γ-Ray Spectroscopy (PGS): This approach, proposed by Verburg *et al.* (37), exploits the spectral characteristics of the prompt γ-ray emission. A collimated spectroscopic detector is focused on the beam path region just after the BP for registration of the prompt γ-ray emission spectrum. As discussed in Subsection 1.5, the cross sections of inelastic proton interactions which traverse a material are energy dependent, and γ emission energies are independent for different discrete transitions. The yield ratios of γ-ray emissions from different spectral lines can thus be recalculated according to the mean incident proton energy in the region observed and connected to the prompt γ-ray range. These ratios further allow insight into the elemental composition of the material tissues in the region observed. The first proof-of-principle experiments performed encountered issues with small statistics. A setup using 8 $LaBr_3$ detectors with tungsten collimators and custom designed high-throughput electronics (10^7 s^{-1}) was created as a prototype, all positioned on an adjustable apparatus to customize the incident beam direction. After background suppression, the achieved range verification accuracy measured 1.1 mm precision with a water phantom target and clinically-viable current and dose values.

1.7 Prompt γ-Ray Emitters

The methodology of this study is based on the detection of prompt γ-rays whose production is artificially enhanced by using a non-radioactive element transported selectively to the tumor region via specific drug uptake. The nuclei of the selected stable isotope emit characteristic de-excitation prompt γ-ray following nuclear interactions with the primary proton beam. The nuclear interactions of the element with the beam create a signature prompt γ-ray spectrum, from which the position of the tumor can be reconstructed. The element choice is the key to obtaining a prompt γ-ray spectrum significantly different from the background produced by the body and also for physiological considerations (as uptake and toxicity effects). The reference background material considered in this project is pure water since it is the one that is commonly used in Quality Assurance in radiotherapy.

This study faces the following challenges:

i. **Selection of the non-radioactive target enriched element:** It should be non-toxic to the patient and have a low natural abundance in the human body, producing a characteristic prompt γ-ray spectrum when irradiated with a proton beam. This enables discrimination between normal tissue background (prompt γ-rays produced in the body) and the prompt γ-ray spectrum in the element-enriched tumor;

ii. **Study into the various reaction mechanisms causing prompt γ-rays:** clinically, the therapeutic proton beam irradiating the tumor region encompasses a broad range of energies, starting at just a few MeV to tens of MeV. This opens several interaction channels for the production of prompt γ-rays, whose cross section depends on the incident proton beam energy. To characterize and quantify the prompt γ-ray enhancement due to the non-radioactive element, it is crucial to investigate these reactions. It has been found that the majority of prompt γ-rays which leave the patient is as a result of inelastic nuclear excitation and light nucleon evaporation;

iii. **Element concentration in the tumor:** The element concentration inside of the tumor is related to the drug carrier uptake, which depends on its pharmacokinetic and pharmacodynamic characteristics. Further, the spatial accuracy of the tumor region reconstruction is strongly correlated to the drug carrier selectivity of the tumor, such that if margins are not upheld and diffusion occurs in healthy tissue, the uncertainty in the tumor position will increase;

iv. **Healthy tissue background characterization:** The prompt γ-ray spectrum as emitted by normal body tissue should be precisely known for both the purpose of selecting the candidate label element and for the optimization of the detection system;

v. **Statistics:** The prompt γ-ray enhancement in the treatment volume depends predominantly upon the above-mentioned points, especially the concentration of the element in the

tumor (as low as reasonably achievable). These statistics can be further controlled by ensuring that the detection system is designed to maximize the γ detection efficiency and background suppression;

Measurements should be made within a range that is compatible with a possible medical plan (i.e. 10^7 protons per spot, with 10^3 spots). The intensities of the average clinical beams are usually in the order of 10^{10} proton/s to 10^7-10^8 carbon/s. The number of incident ions per spot in an active delivery using a pencil-beam scanner can vary by up to 2 orders of magnitude. The most important area for a 2 Gy irradiation, the distal region of the treatment volume, sees the number of incident ions to be $\approx 10^8$ for protons. Thus, a few 10^7 prompt γ-rays are detected for these spots in 4π during treatment with protons, numbers which are then reduced by the detection efficiency (as well as solid angle) and the potential focus of the imaging near to the BP falloff. These clinical implementations and statistics depend further on the beam delivery mode and accelerator type.

1.8 Motivation

As I have introduced in this chapter, the detection of prompt γ-rays remains a challenge in PT, requiring the development of a device for online range verification to improve the accuracy of treatment margins. It is this challenge that drives the motivation of this work and the key aims which it encompasses. In this dissertation, I propose a novel approach for online dose verification which is based on the enhancement of prompt γ-ray production. This is achieved by introducing a non-toxic stable element to the tumor region. These elements are investigated at high and low concentrations in terms of their prompt γ-ray response and yield compared to water and PMMA background (as human tissue equivalents).

This work focuses on identifying such an element and characterization of its proton-induced prompt γ-ray spectrum. The identification of such a prompt γ-ray enhancement element (which would be drug-delivered into the human body) would assist in improving the statistics of the detectable signal, a major challenge in correlating primary ion range to secondary particle production. Monte Carlo simulations were performed of the experiments conducted for preliminary predictions regarding the measurements, for comparison to final measured results, and investigation into the physics behind the simulated results. The findings reported will contribute a new perspective to online range verification, improve treatment effectiveness and help strengthen the application of PT in the fight against cancer.

Chapter 2

Materials and Methods

This chapter reports on the methodology and post-processing of the TOPAS Monte Carlo model developed for the prompt γ-ray simulations and the experiment performed in collaboration with the Trento Proton Therapy Centre (Italy). The focus of the following methodology was to study the prompt γ-ray spectra of carefully chosen elements as a function of material concentration. The simulation focused on the scoring of the energy deposition of secondary γ-rays produced by the proton induced inelastic reactions. The candidate materials investigated for their prompt γ response were chosen to be ^{31}P, ^{nat}Cu,^{89}Y, and pure water. These elements are chosen as they are non-toxic to the human body for low molar concentrations and have a low natural abundance in the human body, thus producing a characteristic prompt γ-ray spectrum when irradiated with a proton beam. This enables discrimination between normal tissue background (prompt γ-rays produced in the body) and the prompt γ-ray spectrum in the element-enriched tumor region.

The geometry was designed to investigate the following points:

i. To investigate the background of prompt γ-rays generated inside and outside of the target human tissue tumor;

ii. To study the prompt γ-ray enhancement typical of each solid target element before re-scaling to an achievable therapeutic concentration;

iii. To quantify the enhancement of the prompt γ-rays energy spectrum for each candidate liquid target at high and low concentrations;

iv. To identify the proton-nuclei reactions yielding prompt γ-rays and to study their contribution to the overall energy spectrum. In particular, we focused on proton induced nuclear reactions, including direct emission of γ-rays or emission of γ-rays after nucleon and light fragment evaporation.

2.1 Geometry of Simulation and Experiment

To investigate the prompt γ-ray enhancement of the candidate target elements, the interaction of a 70 MeV proton pencil beam with different targets at various concentrations was both simulated and measured experimentally. The geometries of all apparatus and targets were defined by the setup used in experiment, which was reproduced by simulation. The initial beam energy was chosen such that the energy deposition maximum value was observed in the BP region in the targets, information which was obtained with simulation by scoring the incident proton energy as a function of beam penetration depth, where the range of 70 MeV in water is approximately 4 cm (see Fig 2.1). The Continuously Slowing Down Approximation (CSDA) range is obtained when one simply integrates the inverse stopping power of the particle energy to obtain the average range (r_{CSDA}) as seen in Eq 2.1.

$$r_{CSDA} = \int_0^{E_{inc}} \frac{1}{\rho} \frac{1}{S(E)} dE \tag{2.1}$$

Where $S(E)$ is the stopping power of the particle in that material, and E_{inc} is the energy of the incident particle. This is an oversimplified view which is based on no other physics being taken into consideration.

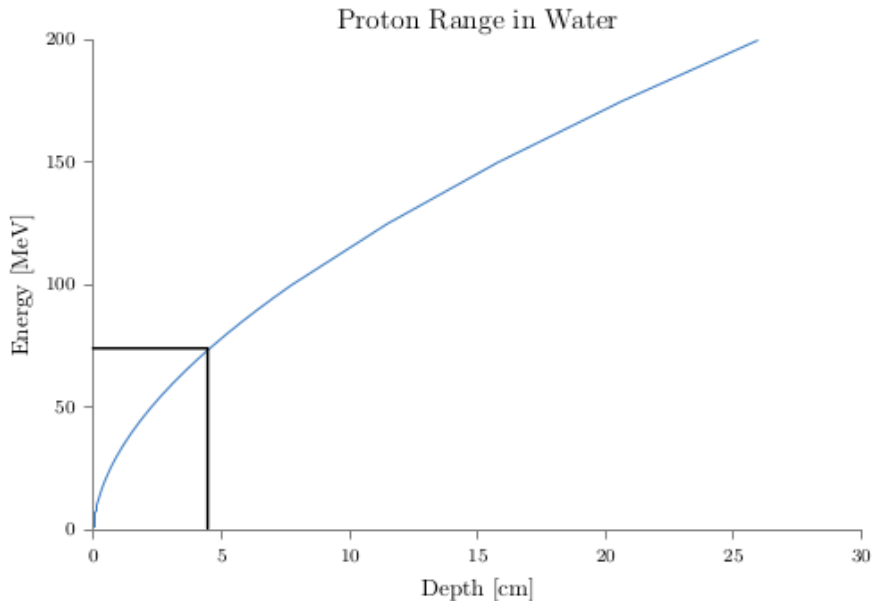

Figure 2.1: Plot showing proton range in water as a function of energy measured in MeV as computed in the Continuously Slowing Down Approximation (CSDA). The 70 MeV proton beam stops at ≈ 4 cm.

2.1.1 Targets

To explore the feasibility of the proposed methodology, three candidate materials were chosen to be investigated as prompt γ-ray enhancers: ^{31}P, ^{nat}Cu and ^{89}Y. The material elements were selected based on the selection criteria outlined in Section 1.7. The targets were first investigated for their prompt γ-ray response in their natural solid form after which the concentration of the element in the tumor was controlled by dissolving the salt form of these targets into pure water, which created more prompt γ-ray reaction channels with the introduction of additional elements in the tumor. The salts which were investigated were $CuSO_4$, NaH_2PO_4 and $Y(NO_3)_3$, of which the most probable reaction channels are discussed in Table 2.1. The decision of target candidate selection was made simpler by the use of the TALYS simulation toolkit (5).

Target Material	Parent Element	Probable De-excitation Level [MeV]
H_2O + PMMA	O	^{16}O: 6.13
		^{16}O: 2.27
		^{15}O: 5.27
	C	^{12}C: 4.44
		^{11}C: 2.00
	N	^{14}N: 2.31
		^{14}N: 1.64
$CuSO_4$	Cu	^{63}Cu: 0.962
		^{65}Cu: 1.0368
		^{65}Cu: 1.104
		^{62}Ni: 1.1712
		^{63}Cu: 1.3248
	S	^{32}S: 2.231
		^{32}S: 2.127
$Y(NO_3)_3$	Y	^{87}Y: 0.797
		^{88}Sr: 0.866
		^{89}Zr: 0.947
		^{88}Zr: 1.075
		^{88}Y: 1.275
NaH_2PO_4	P	^{31}P: 1.1328
		^{31}P: 1.2672
		^{31}P: 1.3728
		^{30}P: 1.4496
		^{30}Si: 1.5168
		^{28}Si: 1.7856
		^{30}P: 2.0256
		^{23}Na: 2.639

Table 2.1: The de-excitation levels of interest for the various elements as found in the solid and/or liquid targets. Obtained using the NUDAT database (7).

TALYS (5) is a modern simulation code dedicated to nuclear reaction calculation of target nuclei A $\geq$ 12 and incident energies up to 200 MeV. It makes use of numerous models to calculate the reaction chains of possible nuclear reactions as well as their associated cross sections. The discrete γ decay of the isotopes present in the proton irradiated targets was calculated with a 70 MeV proton beam using TALYS v1.95 to gain insight

into the possible decay fragments and their associated cross sections. The proton, γ-ray, and neutron particle production cross section were also scored at the same beam energy for the target materials after interaction with the proton beam. The user specifies the projectile type, mass, element, the beam energy (in MeV) and the scored quantities of interest.
The following TALYS scoring flags were applied:

i. **outspectra:** This flag includes the output of the angle-integrated emission spectra.

ii. **filespectrum g:** This creates a file for the output of the composite particle spectrum for the γ-ray particle type. The file contains the emission energy and 5 columns with the total, direct, pre-equilibrium, multiple pre-equilibrium and compound spectrum.

iii. **outgammadis y:** Flag for the output of discrete γ-ray intensities. All possible discrete γ transitions for all nuclei are followed. In the output they are given in tables per nuclide and for each decay from state to state.

iv. **outpopulation y:** Flag for the output of the population, as a function of excitation energy, spin and parity, of each compound nucleus in the reaction chain before it decays

v. **outdiscrete y:** Flag for the output of cross sections to each individual discrete state. This is given for both the direct and the compound component.

vi. **adddiscrete y:** Flag for the addition of energy-broadened non-elastic cross sections for discrete states to the continuum spectra.

TALYS cross section analyses were performed to determine the probability of prompt γ-ray production. When comparing these isotope cross sections obtained with a 70 MeV proton beam, the (p,xγ) reaction of interest as seen in Fig 2.2 demonstrates that the probability of producing prompt γ-rays is higher for ^{89}Y, ^{31}P, ^{65}Cu and ^{63}Cu than for reactions involving ^{16}O in terms of cross section. This shows promise as it suggests that once the solid targets are dissolved in a water solvent, a γ enhancement should be visible when the solution is compared to water, especially in the low energy region which attributed to the fact that the mass of these elements is greater than the background elements. These elements can therefore be used as γ enhancers.

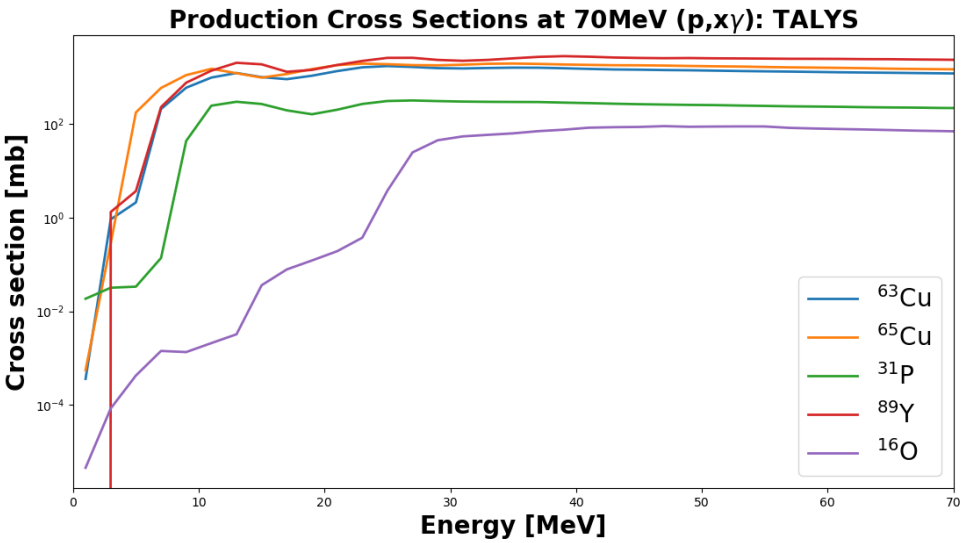

Figure 2.2: The prompt γ-ray production (p,xγ reaction) cross sections of target elements vs proton beam energy as calculated by TALYS (5).

Furthermore, Fig 2.3 shows that in the low energy region, γ production probability is particularly high for ^{89}Y, ^{31}P, ^{65}Cu and ^{63}Cu when compared to the secondary neutron signal. The salt form of the solid targets (NaH_2PO_4, $CuSO_4$ and $Y(NO_3)_3$) investigated (in Subsection 3.3) contribute additional elements which open up more reaction channels in the prompt γ-ray spectrum. It is not expected to see significant γ contribution from the salt constituents ^{32}S and ^{14}N, however, the ^{23}Na plot shows a discernible probability of a peak emerging.

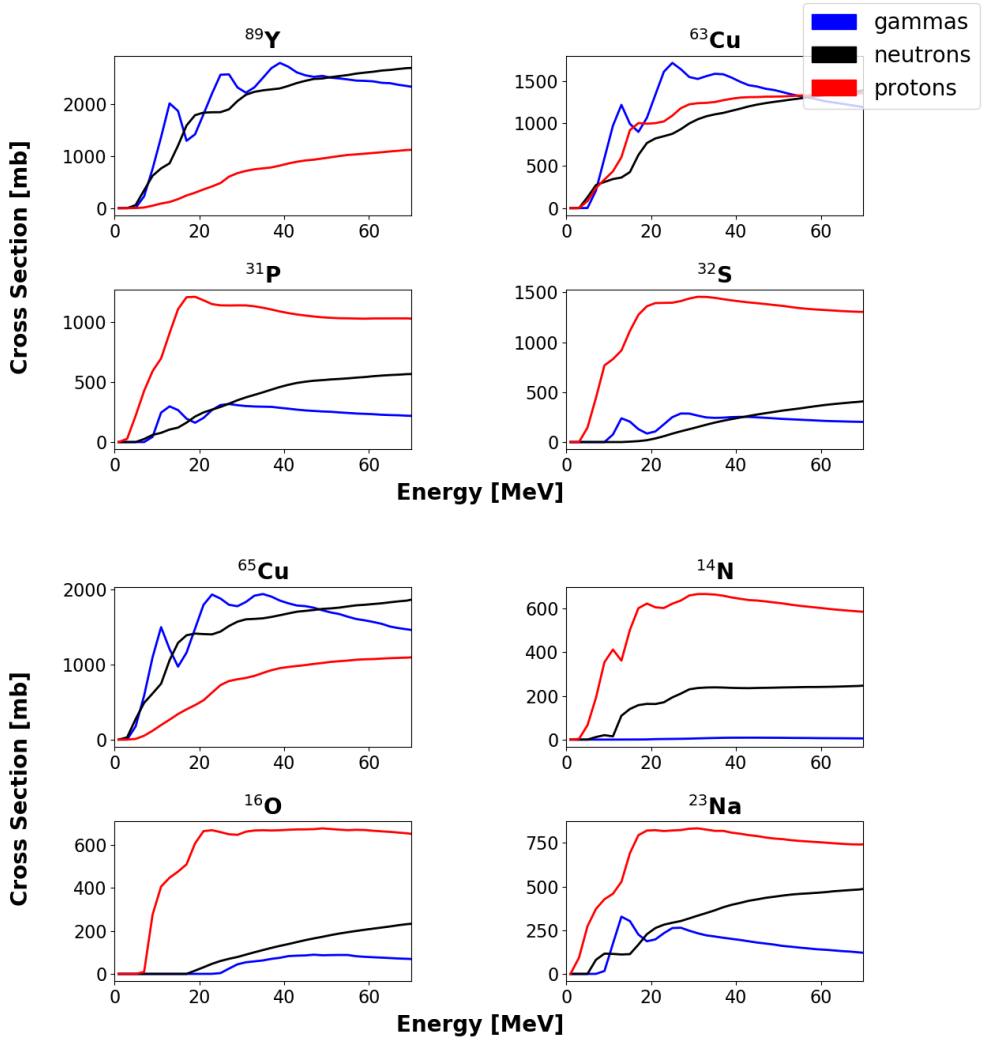

Figure 2.3: TALYS (5) generated plots of the proton, neutron and γ-ray production cross sections of the various elements present in the salt and solid targets.

2.1.2 Solid Targets

The solid targets investigated for their prompt γ-ray response were ^{nat}Cu, ^{nat}P and ^{nat}Y. The targets were all composed of a highest natural abundance of their respective isotope: copper has a natural composition of both ^{63}Cu (69.345%) and ^{65}Cu (30.365%), yttrium has a natural abundance of 100% ^{89}Y, and phosphorus with a 100% natural abundance of ^{31}P. Phosphorus in its elemental form is highly reactive and, as such, phosphorus is not found as a free element on Earth, but occurs rather in the form of phosphate. A solid target of phosphorus could not be manufactured for experiment as the element ignites with air to produce phosphoric acid. The solid target form would thus have had dangerous health risks in the experiment and would ignite quickly, losing its target dimensions (38). Therefore, the only target for which experimental results were not obtained was solid phosphorus, although simulations were conducted with phosphorus in its elemental form with a 100% abundance of ^{31}P to understand its prompt γ-ray response. Although concentrations as high as these are not realistic, it provides an estimate of the prompt γ-ray enhancement typical of each element, the value of which can then be re-scaled to the achievable therapeutic concentration in a tumor.

The solid targets had a solid cylindrical geometry, with varying heights and radii, with the exception of ^{31}P, which had a solid box geometry in simulations (for which the dimensions were chosen such that the proton beam stops within the target volume). A summary of the materials properties is reported in Table 2.2, while an illustration of the simulation geometry is shown in Fig 2.7(a) and experimental geometry is pictured in Fig 2.4(b). A challenge was encountered with the geometry of the solid targets in the experiments, where the beam spot at 70 MeV had a FWHM of 1.6 cm at the target, a value which was larger than the heights and widths of the solid copper and yttrium targets. Therefore, an estimate of where the proton interacts with the target in the experiment had to be considered and was then normalised for in post-processing.

Material	ρ **[g/cm^3]**	**A [g/mol]**	**Geometry**	**Dimensions [cm]**
^{nat}Cu	8.96	62.929597	Cylinder	H:3, R:0.475
^{31}P	1.82	30.97380	Box	X:2.5, Y:2.5, Z:2.5
^{89}Y	4.472	88.90584	Cylinder	H:0.635, R:0.3175
Water	1	-	Box	X:5, Y:5, Z:5

Table 2.2: Characteristics of candidate solid targets as employed in TOPAS simulations.

2.1.3 Liquid Targets

To reproduce a more realistic medical scenario, simulations and experiments were performed measuring the γ emission of the selected materials using different concentrations resembling the uptake of the elements in the tumor. The liquid target here refers to two salt solution filled PMMA ($C_5H_8O_2$) flasks (to simulate the most abundant elements of the human body:

carbon, oxygen, and nitrogen) which were placed with their largest surfaces in contact (to ensure the beam stopping in the target volume). This is pictured for experiment in Fig 2.4(a) and shown for simulation in Fig 2.7(b). The targets were created by using salts of the solid targets investigated, namely: NaH_2PO_4, $Y(NO_3)_3$ and $CuSO_4$. This study was first performed with copper and yttrium as solid targets with as high an abundance as naturally possible (^{nat}Cu: 69.345% ^{63}Cu and 30.365% ^{65}Cu, ^{nat}Y: 100% ^{89}Y, and ^{nat}P: 100% ^{31}P) to understand their prompt γ-ray response at the highest natural concentration before they were then dissolved in a homogeneous solution of pure water and salt to create liquid targets of the marker elements. Phosphorus was only investigated in liquid form since manufacturing a solid target is very complicated due to the characteristics of this material. The chosen salts of these isotopes were: NaH_2PO_4, $Y(NO_3)_3$ and $CuSO_4$. These liquid targets were placed in PMMA flasks and the prompt γ-ray response at various concentrations was then studied. These flasks had dimensions $5 \times 5 \times 2.5$ cm with an internal thickness of 0.226 cm. The γ response of the element at concentrations of $\approx 5\%$, $\approx 1\%$, and $\approx 0.5\%$ in water were investigated. These targets have an average beam-penetrating thickness of 5 cm. The background response of the pure water solvent was characterized, allowing quantitative analysis into the prompt γ-ray enhancement of these elements. A summary of the liquid targets at different concentrations and their associated properties can be found in Table 2.3. The molar mass percentages of the main elements studied were adjusted to be as close as possible to one another so that accurate evaluations between salts at high, medium, and low concentrations could be undertaken.

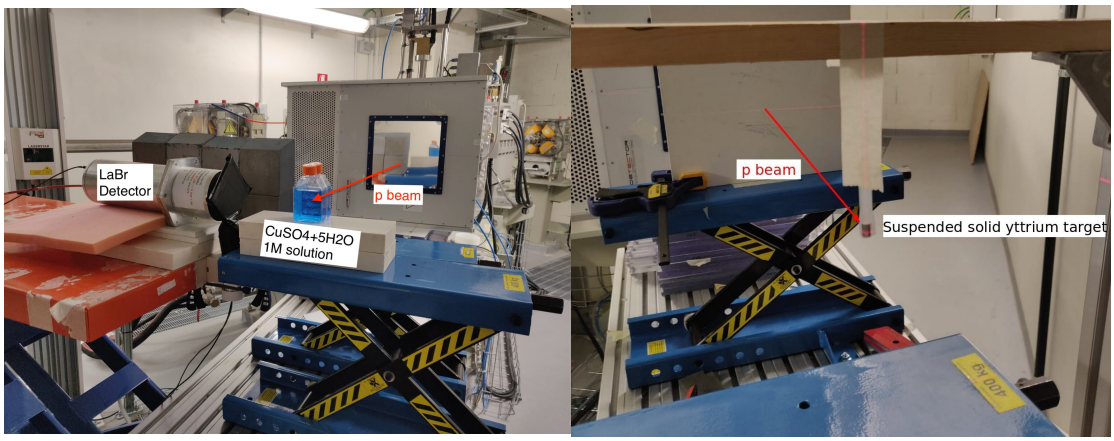

(a) (b)

Figure 2.4: Labelled photographs of the experimental setup with red arrow representing the approximate direction of the incident proton beam line for (a) Liquid targets, where the pictured target is $CuSO_4 + 5H_2O$ target (as dissolved in 100ml H_2O and placed in two PMMA flasks). (b) Solid targets, where the pictured target is solid ^{89}Y suspended by tape.

Material	Mole [M]	ρ [g/cm^3]	O	H		
H_2O	-	1.00	88.8144	11.1856	-	-
					Cu	**S**
$CuSO_4$+5H_2O	1	1.2490	82.59	9.76	5.08	2.57
	0.2	1.0499	87.36	10.85	1.19	0.6
	0.1	1.0102	88.04	11.01	0.63	0.32
					Y	**N**
$Y(NO3)_3$+6H_2O	1	1.38292	81.58	8.95	6.43	3.04
	0.17	1.065113	87.21	10.70	1.42	0.67
	0.1	1.0383	87.85	10.89	0.86	0.40
					P	**Na**
NaH_2PO4+H_2O	2	1.275989	82.14	9.40	4.86	3.60
	0.5	1.068997	86.81	10.64	1.48	1.07
	0.2	1.027599	87.99	10.96	0.60	0.45

Table 2.3: Characteristics, including elemental composition percentages, of salt targets dissolved in 100ml of H_2O, as employed in TOPAS simulations.

2.1.4 Experiment

Experiments were performed by collaborators at the University of Trento, Italy. Experiments were conducted to gain insight into the prompt γ-ray response of the elements of interest as well as to check the reliability of the prompt γ-ray response predicted in the simulation in terms of cross section. A proton pencil beam was accelerated to 70 MeV by the cyclotron at the Proton Therapy Centre in Trento (Italy) (39). The beam was initially accelerated by the cyclotron to a maximum energy of 228 MeV which was then reduced to its minimum value of 70 MeV shortly after the cyclotron exit via a coarse energy selection by a range modulation wheel composed of different materials and thicknesses. The beam energy was pseudo-monoenergetic, with an energy spread of 0.9%. The beam intensity was chosen at the exit of the cyclotron, where 1 nA yields a count rate of 10^6 particles produced in the ionization chamber. The proton beam current is modulated by a 50% duty-cycle square wave, with a 100 ms period (39). Protons exit the beam pipe by traversing a 70 μm thick layer of titanium. Lasers and adjustable tables were used to ensure that the target was situated at the beam isocenter. The experimental set-up is depicted in Fig 2.5.

Experiments were performed with solid ^{nat}Cu and ^{89}Y targets, pure water in a PMMA box, and various concentrations of liquid salt (NaH_2PO_4, $CuSO_4$, and $Y(NO_3)_3$) targets. All targets were placed with their center 120 cm from the beam exit along the beam line. The methodology pertaining to the solid and liquid targets is described in Subsections 3.2 and 3.3 respectively, where the proton beam was incident normal to the target surface for all target geometries. After interaction with the target, the secondaries (γ-rays, protons, neutrons, etc.) were detected by a 3" by 3" $LaBr_3$:Ce detector. The $LaBr_3$:Ce detector

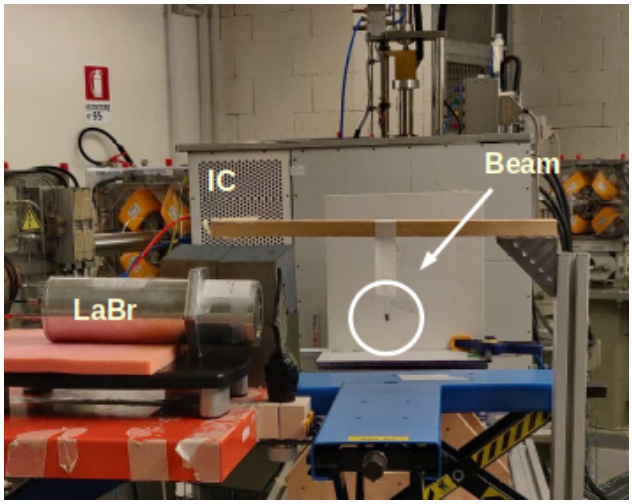

(a)

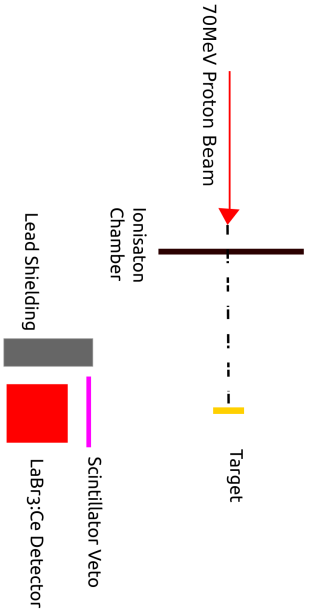

(b)

Figure 2.5: Experiment set-up used for all target measurements. In panel (a) is shown a photograph of the experimental set-up using the solid target taken along the beam line, looking upstream. The target (circled) is located at the isocenter. In panel (b) is a labelled top-view schematic of the experimental set-up.

was situated 18.5 cm from the target position and at 90° to the beam axis. In front of the $LaBr_3$:Ce detector a 5 mm thick EJ-200 plastic scintillator was positioned to allow for charged particle discrimination in the post-processing analysis. The total proton flux delivered to the targets was measured using an ionisation chamber. Experimental data was acquired by a VME based Data Acquisition (DAQ) system which was triggered by the $LaBr_3$:Ce detector. A schematic representation of the DAQ system is depicted in Fig 2.6(a).

The received analog signals of the $LaBr_3$:Ce detector and plastic scintillator were passed to the CAEN 792N Charge-to-Digital Converter (QDC) of 12-bit resolution using an integration gate of 500 ns for the $LaBr_3$:Ce detector and 100 ns for the veto scintillator. The QDC performed a gated integral of the pulse shape proportional to the energy deposited by the particle inside the detector, seen in Fig 2.6(b). The pulses from the two detectors were discriminated through a CAEN N843 leading-edge discriminator which generates a NIM logic signal when the amplitude of the pulse exceeds a defined threshold. The discriminated signals were then sent to the CAEN V1190B multi-hit time-to-digital converter (TDC) and CAEN V830 scaler. The TDC opens a time window of $\pm 1\mu$s around the DAQ trigger time

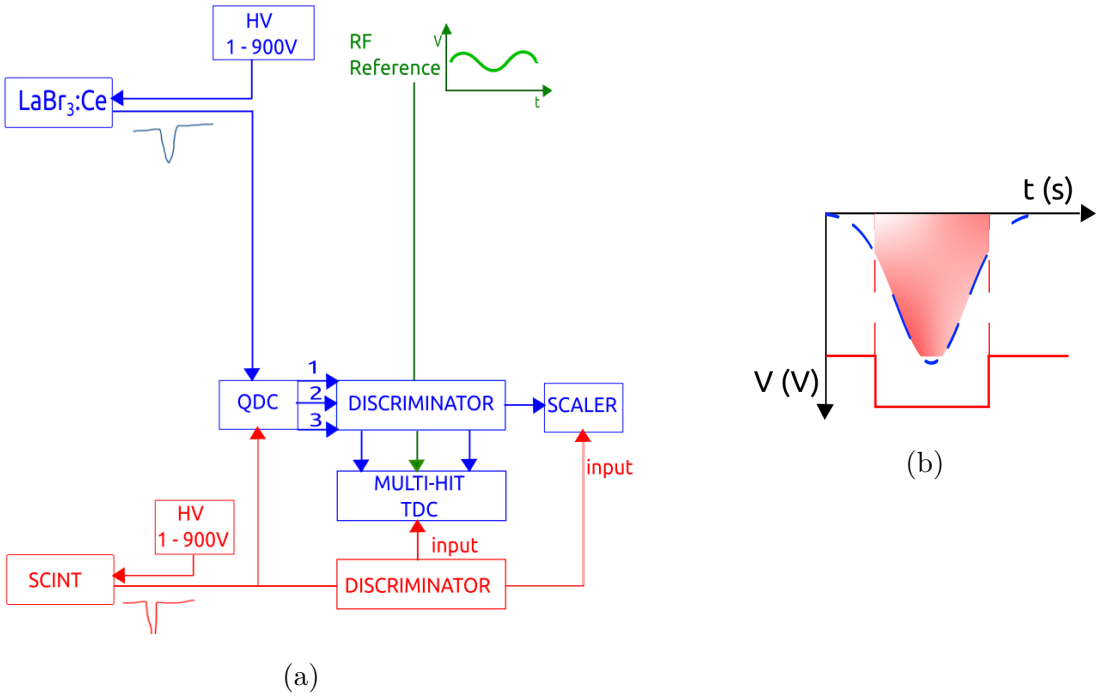

(a) (b)

Figure 2.6: (a) Schematic diagram of the data acquisition set-up for the DAQ system: HV - High Voltage, PREAMP - Pre-amplifier, AMP - Amplifier, QDC - Charge to Digital Converter, TDC - Time to Digital Converter, SCINT - Plastic Scintillator. The scintillator is situated in front of the detector, however it is pictured separately to demonstrate the DAQ. (b) QDC module: blue curve represents the input energy signal, red region represents gate.

and it registers all the arrival times of the detector signals within the window, counting the number of events seen by the $LaBr_3$:Ce detector and plastic scintillator, as well as the number of the DAQ accepted triggers. In fact, while the DAQ is processing and sending the data from the modules it does not accept new events. The ratio of accepted to total triggers was used to characterize the acquisition dead time. The dead time was used in post-processing to correct the energy spectra of the measured prompt γ-ray yield. A summary of the component geometries is reported in Table 2.4. Figure 2.5(a) shows the photographed beam-line setup of the experiment, seen schematically in Fig 2.5(b). The simulation geometry was set to match this configuration.

The $LaBr_3$:Ce triggered multi-hit TDC received input from the detector, cyclotron radio-frequency signal (RF), and the scintillator veto, outputting an array of time values in nanoseconds for each input. This TDC is performed by opening up a time window of $\pm 1\mu$s with respect to the trigger signal. For each input, it stores the time at which the signal arrives within the window with a resolution of ≈ 100 ps. The use of the cyclotron

Component	**Material**	ρ [**g/cm**^{3}]	**Composition** (%)	**Dimensions** [**cm**]	**Position** (**x,y,z**) [**cm**]
Veto Scintillator	EJ-200	1.032	C:91.53,H:8.474	X:0.25,Y:5,Z:5	(20,0,-120)
$LaBr_3$:Ce Casing	Aluminium	2.6989	100	R:8.98,H:4.32	(26,0,-120)
$LaBr_3$:Ce Detector	$LaBr_3$:Ce	5.08	La:36.69,Br:63.61	R:4.2,H:8.38	(0,0,0)
Lead Shield	Lead	11.35	100	X:8.38,Y:8.04,Z:6	(26,0,-105)

Table 2.4: Characteristics of simulation components.

RF reference signal allowed discrimination between prompt and background events (see Subsection 2.2.3).

2.1.5 TOPAS Simulations

The Monte Carlo method is a numerical solution to a problem that models objects interacting with other objects and/or with their environment. The physical process is described in terms of probability distributions. (Pseudo)random numbers are used to sample the probability distribution and to score the quantities of interest. Among the most utilized Monte Carlo tools in the PT community is TOPAS (TOol for PArticle Simulation). TOPAS (40) is an optimised tool that was developed to enhance the user-friendly capability of the Geant4 simulation toolkit by wrapping and extending it for use by medical physicists. The TOPAS MC software is structured into four main components, namely: Geometry, Particle Source, Scoring, and Physics. The geometry aims to best reproduce an experimental set-up. These parameters come together to form the heart of the simulation. Once the experimental geometry has been constructed, the scoring quantity is chosen and physics lists set, the simulation starts. Particles are tracked until they reach E = 0 eV. The particle trajectory is the sum of the particle steps determined by interactions or geometric boundaries.

All simulations were performed using TOPAS version 3.6.1 and using the computing resources as provided by the Centre for High Performance Computing (CHPC) Lengau Cluster. The simulation environment was designed to replicate that of the experiment. All simulations were computed using the TOPAS default physics lists, detailed in Table 2.5, which is highly documented as the best option for proton therapy dose calculation applications. This list incorporates physics models which control all secondary particles, not only protons. It is adapted to the latest Geant4 release to render results that closely match those described in Jarlskog . (2008) (41).

Interaction	**Constructor**
Electromagnetic	Standard_Opt4
Hadronic	G4HadronPhysics_QGSP_BIC_HP G4IonBinaryCascadePhysics G4HadronElasticPhysics_HP
Decay	G4StoppingPhysics
Stopping	g4stopping

Table 2.5: Summary of the Geant4 physics constructor modules used in the TOPAS default physics list.

The world environment into which all geometries were placed was $1\times1\times1.5$ m^3 ($x\times y\times z$), filled with the predefined material Air with the beam positioned at its center. Figure 2.8 shows the simulation set-up with the components visible and the proton beam (visualised as blue) on and incident on the target center. Solid and liquid targets were investigated in both simulation and experiment. The solid materials ^{nat}Cu, ^{31}P and ^{89}Y were defined in simulation by using the TOPAS predefined materials from literature (the same materials available in Geant4). While simulations were conducted for the solid phosphorus isotope,

this material could not be obtained for experimental investigation and, as such, is the only material that does not have both simulation and experimental results. In the case of the liquid targets, the targets were placed in PMMA flasks of density 1.19 $\frac{g}{cm^3}$, composed of carbon, hydrogen, and oxygen with mass fractions of 59.9848%, 8.0538% and 31.9614% respectively. The percentage composition of the flask is in agreement with the flasks used in the experiment. Liquid target solutions of $CuSO_4$, NaH_2PO_4 and $Y(NO_3)_3$ dissolved in 100ml of pure water were placed in two flasks for each concentration investigated. The concentrations implemented in the simulation replicated those in the experiment, as explained in Subsection 3.3 and summarized in Table 2.3. The solution containing flasks were placed with their front faces in contact as illustrated in Fig 2.7(b).

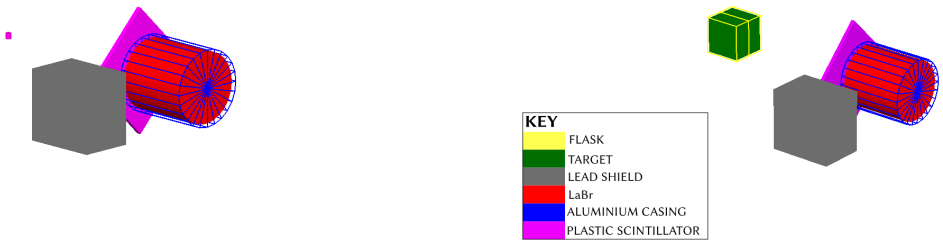

(a) ^{89}Y (b) Liquid Target

Figure 2.7: TOPAS Simulation Setup. Common geometries found in both solid and liquid target set-ups: scintillator (seen as the magenta 45° box), $LaBe_3$:Ce detector with its aluminium casing (seen as red cylinder), lead shield (seen as grey box).

Targets were irradiated by a proton pencil beam of energy 70 MeV. The beam had an energy spread of 0.9 %, Gaussian angular distribution, and a beam angular spread of 0.0057 rad in both the x and y directions, as calculated in experiment. The number of protons simulated for each material is mentioned in the corresponding results of that material and ranges from 10^9 to 10^{11} incident protons.

The detection was such that a plastic scintillator of density 1.032 $\frac{g}{cm^3}$ (composed of 8.474% hydrogen and 91.526% carbon) acting as a charged particle veto was situated in front of the $LaBr_3$:Ce detector. The $LaBr_3$:Ce detector was encased in aluminium and shielded by a solid block of lead. The lead shielding was simply used to shield from scattered protons and to attenuate γ-rays not originating from the target. The full simulation set-up is illustrated in Fig 2.8, more information on the simulation geometry can be found in Table 2.4.

The scoring of the energy deposition in simulation occurred in two parts. The first code, as can be seen in the Appendix Listing 2, scored a quantity defined as phasespace. This is a feature used in TOPAS that saves a screenshot of the space-time of the particles of

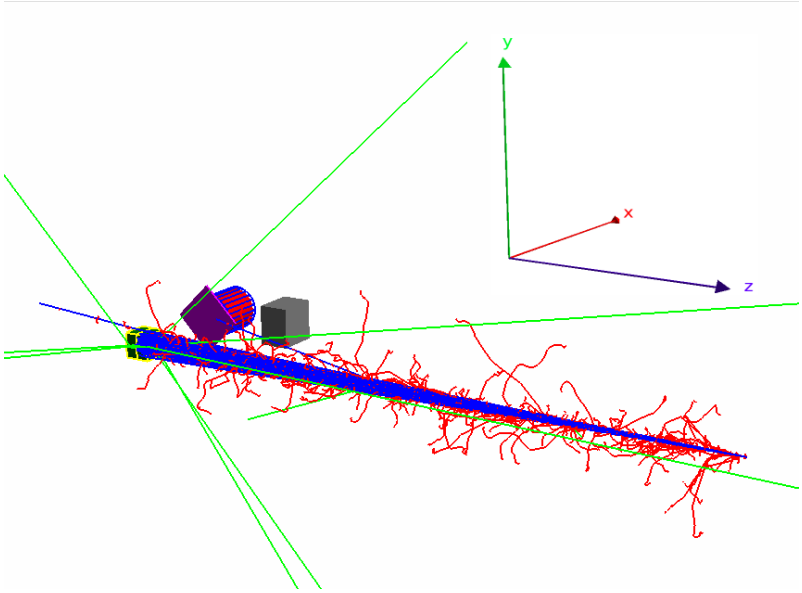

Figure 2.8: Pictured is a schematic of the full TOPAS simulation environment showing the proton-target interaction when the beam is on. The proton source is situated 1.2 m from the targong the z-axis.

interest such that the simulation can be replayed from this point in space-time, allowing one to increase the simulation statistics while reducing computational time. The phasespace files for the first set of simulations run for each material of interest and/or at each concentration scored the particles (protons, neutrons, and γ-rays) originating from the target and seen by the z-surface (flat face) and curved surface of the $LaBr_3$:Ce detector. Four independent sets of phasespace files were stored in this first run, however, only the particles originating from the target were used for the next stage of the simulation. The second stage of the simulation, for which the code can be seen in Appendix Listing 3, was again conducted using TOPAS v3.6.1. Here the information regarding only the γ-ray particles as originating from the targets and seen by the surface of the $LaBr_3$:Ce detector was used and the time-stepped energy deposition of γ-rays on the surface of the $LaBr_3$:Ce detector was calculated. This energy deposition was calculated by reading in a user-defined macro called TsEnergyDeposit to calculate the time-stepped energy deposition (Appendix Listing 4 and 5) which was not otherwise available as a scoring quantity in TOPAS. The time scored in the phasespace file was calculated starting from the interaction of the incident proton with the target surface. Prompt γ-rays were then discerned from other secondary particles by gating on the γ-rays produced in the nanosecond (ns) time-scale.

For the case of the liquid targets, it should be noted that the scoring of the energy deposition was such that it originated from the liquid target volume and thus did not include the interactions of the incident beam with the PMMA flask. The PMMA spectrum is thus not included in the simulation results, however, the PMMA prompt γ-ray response

is present in the experimental results. Once the energy deposition was obtained, energy smearing of the $LaBr_3$:Ce detector efficiency response was applied to the simulation results to increase the accuracy of comparison between results obtained in simulation and those from the experiments. The details regarding this energy smearing is explained in Subsection 2.2.2. The application of smearing showed results with less noise than those for which smearing was not applied. All simulation results discussed in Chapter 3 were obtained using the smearing techinque. All data have been processed using MATLAB R2021a. Further, the results obtained have been plotted with a binning of ≈ 10 keV per bin.

2.2 Post-processing of Results

2.2.1 Characterization of the $LaBr_3$:Ce Detector

The Cerium doped Lanthanum Bromide scintillating detector, or $LaBr_3$:Ce, is one of the new generations of inorganic scintillation γ-ray detectors. The LaBr detector was chosen for this experiment as the crystal exhibits excellent properties. For example, it has the best energy resolution among all the scintillators (2.7–3.3% FWHM at the 661.6 keV emission peak of ^{137}Cs), a fast light decay time (the signal goes to zero in $\approx$ 100 ns), an almost perfect light yield proportionality (at as low as about 100 keV) and good stability of the emitted light with temperature (42) (43). Efficiency and calibration measurements were made for the cylindrical 3" $\times$ 3" detector procured from the University of Milan/INFN-Milan group.

Calibration

The experimental data spectra acquired with the $LaBr_3$:Ce detector were calibrated between each use. In fact it is of importance to account for the variation in experimental conditions such as temperature change, HV settings etc. In order to obtain from the raw data the information of the γ-ray energy detected, known γ-ray sources should be used to established the relation between the value recorder by the ADC and real energy of the γ-rays emitted. For the first characterization, the $LaBr_3$:Ce detector was calibrated using a ^{60}Co source. The ^{60}Co spectrum was obtained by fitting the peaks in the spectrum corresponding to the emitted 1173 and 1332 keV γ-rays via a first-order polynomial as per Eq 2.2.

$$E = a_0 + a_1 \times ch \tag{2.2}$$

The parameters a_0 and a_1 were computed to be 54.8 and 1.039 respectively by applying Eq 2.2 to the nominal energy values (E) of two known peaks (1173 and 1332 keV) in the spectrum of the standard calibration source (see Fig 2.9) which was plotted to observe the energy response linearity of the $LaBr_3$:Ce detector. These calibration values were then used to transform all spectrum channel numbers into keV energy values. Figure 2.10 shows the calibrated results of ^{60}Co.

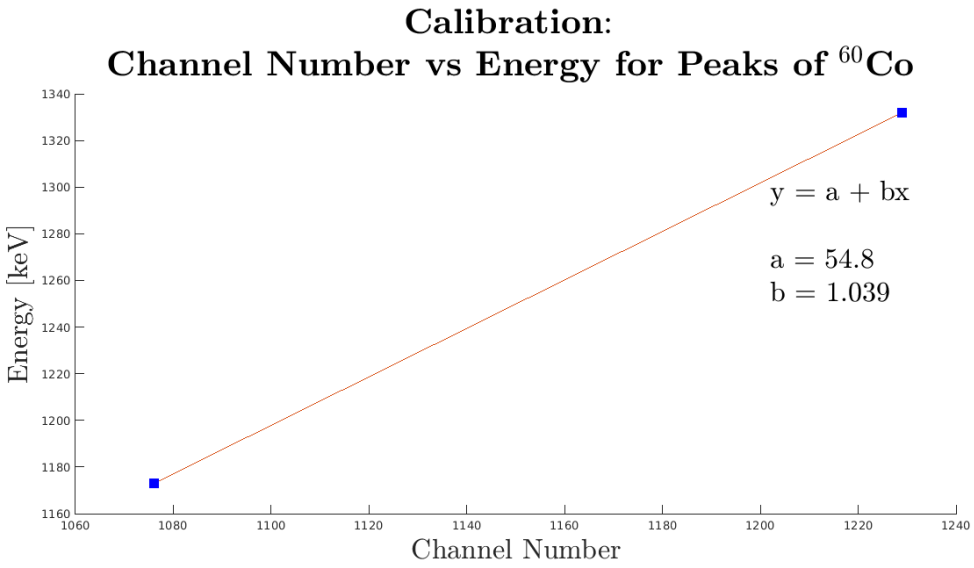

Figure 2.9: Plot of Channel Number vs Energy for the two known peaks (1173 and 1332 keV) in the spectrum of the standard calibration source: ^{60}Co for a 3" × 3" $LaBr_3$:Ce detector. The calibration values obtained were used to transform all spectrum channel numbers into keV energy values. The straight line fit is $y = 1.039x + 54.8$, where x represents the detector output channels.

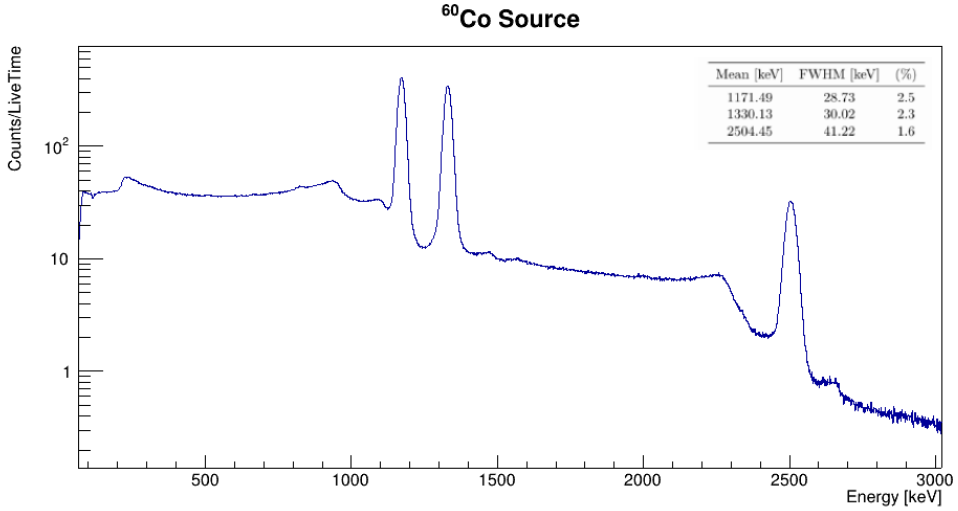

Figure 2.10: The calibrated ^{60}Co spectrum with the obtained fit parameters.

The energy values of the peaks, as seen in the corresponding table are in agreement with known values. Calibration was performed before each experimental measurement session. After the first calibration, the signature prompt γ-ray emission peaks of water were used to re-calibrate all experimental measurements as radioactive sources were no longer available in the experimental area. The peaks in water that were used to pass from channel to energy were 6.13 MeV, 4.44 MeV, 5.27 MeV, and 1.64 MeV, these peaks are discussed in detail in Section 3.1. This formed a more robust calibration than that performed with just the ^{60}Co source and was used to calibrate all liquid target results. In fact, the HV power supply of the PMT could fluctuate around the set value of -900 V and since the collected signal is proportional to the HV, shifts in the channel position arise. This HV power supply has two main reasons resulting in its fluctuations: (1) Each time the power it turned on it reaches a set value with some uncertainty, and (2) Once it is switched on, the stability of the measurement is dependant on the temperature conditions at that time.

Energy Resolution of the $LaBr_3$:Ce Detector

The energy resolution of the detector is of interest as it gives insight into the statistical uncertainty of an individual energy measurement, where the resolution is a measure of the sharpness of a peak. A good energy resolution allows one to distinguish between two closely positioned peaks. The full width at half maximum (FWHM) is a commonly used way of classifying peak widths. It is a measure of the distance between two points on a peak when the counts are at half of the height of the maximum counts. A high-resolution detector has a small FWHM. Typically, photo peaks that have a standard Gaussian shape (Eq 2.3) are characterized by a relationship with a standard deviation of σ, as seen in Eq 2.4.

$$g(\epsilon) = \frac{A}{\sigma\sqrt{2\pi}} exp(-\frac{(\epsilon - E)^2}{2\sigma^2}) \tag{2.3}$$

Where $g(\epsilon)$ is the Gaussian function centered at the incident γ-ray energy E, ϵ represents the broadened energy and A is the normalization constant.

$$FWHM = 2.35\,\sigma \tag{2.4}$$

The important factor affecting energy resolution in scintillation detectors such as this one is the statistical fluctuation in the quantity of photo-electrons produced in the PMT which is seen in the variation in the amplitude between successive events. The energy resolution was obtained for four peaks in the energy range 0.6 to 3 MeV. The first peak was the 661.6 keV emission peak of ^{137}Cs, a standard calibration point source, where

the energy spectrum was collected and the central channel number of the full energy peak determined visually via the peak report on the MCA. See Fig 2.11, where the corresponding table reports the following data after applying a Gaussian fit to the known peaks: energy of the peaks, resolution of the peaks in energy, relative resolution of the peaks in percent ($\frac{FWHM}{PeakMeanEnergy}$). The three peaks of a ^{60}Co point source were also considered, which emits two γ-rays simultaneously that generate two full-energy peaks and a third peak due to the sum of the two main γ-rays at $\approx$ 2501 keV (see Fig 2.10). Gaussian fits were independently applied to the point source peaks, with the obtained mean of $\sqrt{E}$ and σ values then used to calculate the detector energy resolution trend function. By plotting the ratio of $\frac{FWHM}{E}$ as function of $\sqrt{E}$ for each of the four peaks measured in 4π, the data points in Fig 2.12 were obtained. Fig 2.12 is plotted with the model data values that were obtained from the detector manufacturer (refer to Table 2.6). This plot is then fitted with a linear energy function, showing a good correlation between measured data and the desired model values. This function will be used for the smearing procedure.

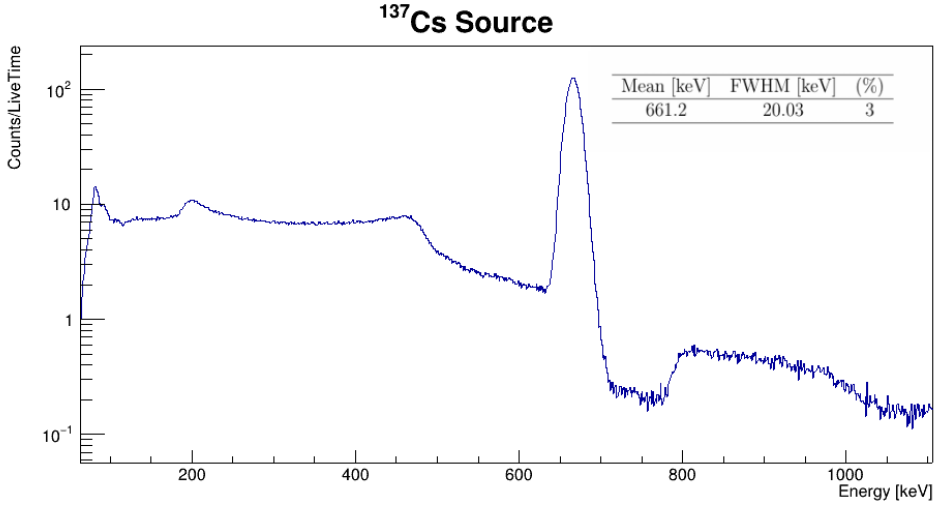

Figure 2.11: The calibrated ^{137}Cs spectrum with the obtained fit parameters.

Element	γ Energy [keV]	FWHM [keV]	Resolution [%]
^{133}Cs	302	13.2	4.4
	356	14.7	4.1
^{137}Cs	661	19.5	2.9
^{60}Co	1173	26.7	2.3
	1332	28.7	2.2
AmBeNi	4400	100.9	2.3
	8997	82.4	0.9

Table 2.6: Table describing the model detector calibration data which, for each of the sources, report the following data: energy of the peaks, resolution of the peaks in energy, resolution of the peaks in percent (8).

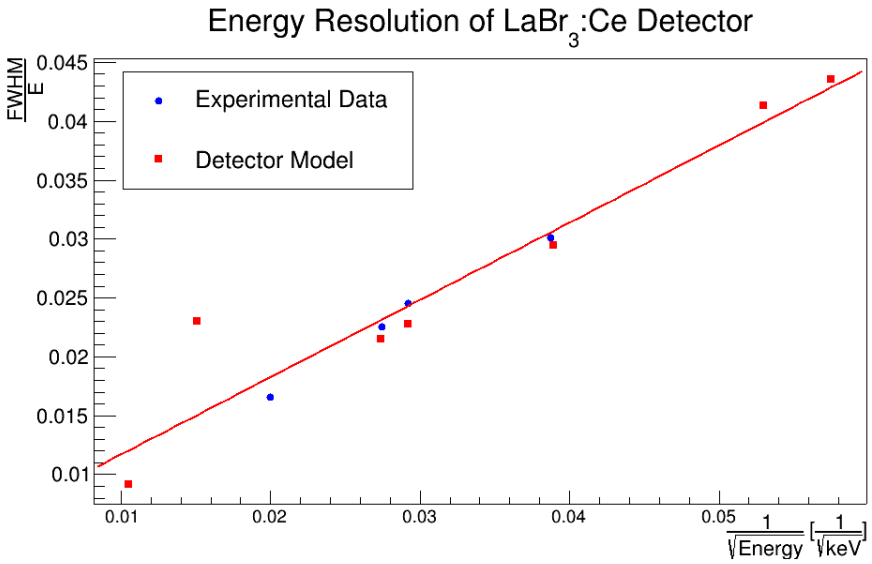

Figure 2.12: Energy resolution, from ^{60}Co and ^{137}Cs spectra and expected values for LaBr detector (inorganic scintillator) model data obtained from the detector manufacturer.

Detector Photopeak Efficiency

The photopeak efficiency is defined as the ratio of the number of counts in the photopeak, N_p, to the number of γ-rays produced, N_0, of the photopeak energy emitted by the source. The value of the efficiency depends on the distance from the radiation source to the scintillator detector and the solid angle subtended by the front surface of the crystal detector as well as the target material itself. It can be used to evaluate the properties of the detector to fully stop or absorb impinging γ radiation by the photoelectric effect or a series of Compton interactions resulting in complete absorption of the γ-ray energy. To obtain the efficiency, simulations were performed using Geant4 toolkit version 10.5.01, where a proton beam of energies of 0.5 MeV and 1 to 10 MeV in increments of 1 MeV (see Fig 2.13) was generated at the target position with an isotropic angular distribution over 4π. The same detector construction was employed as in the TOPAS simulations and experiments (Subsection 2.1.5). Gaussian fits were applied to the photopeak in each spectrum, and the mean peak energy and counts were obtained, as seen in Table 2.7. The data were then plotted and fitted with a power function fit as seen as the intrinsic photopeak vs energy in Fig 2.13. The photopeak efficiency was calculated as the ratio of these counts to the total number emitted by the source. Fig 2.13 shows the behaviour of the $LaBr_3$:Ce detector where the plot is well fitted by the power fit function. This is predicted as at 662 keV, the photopeak efficiency is 2.617%, which is two times better than that of the 3" $\times$ 3" Sodium Iodide (NaI) detector at the same distance from beam exit and target (44). The $LaBr_3$:Ce efficiency is considered a high efficiency detector and is attributed to the homogeneity and high light output of the crystals.

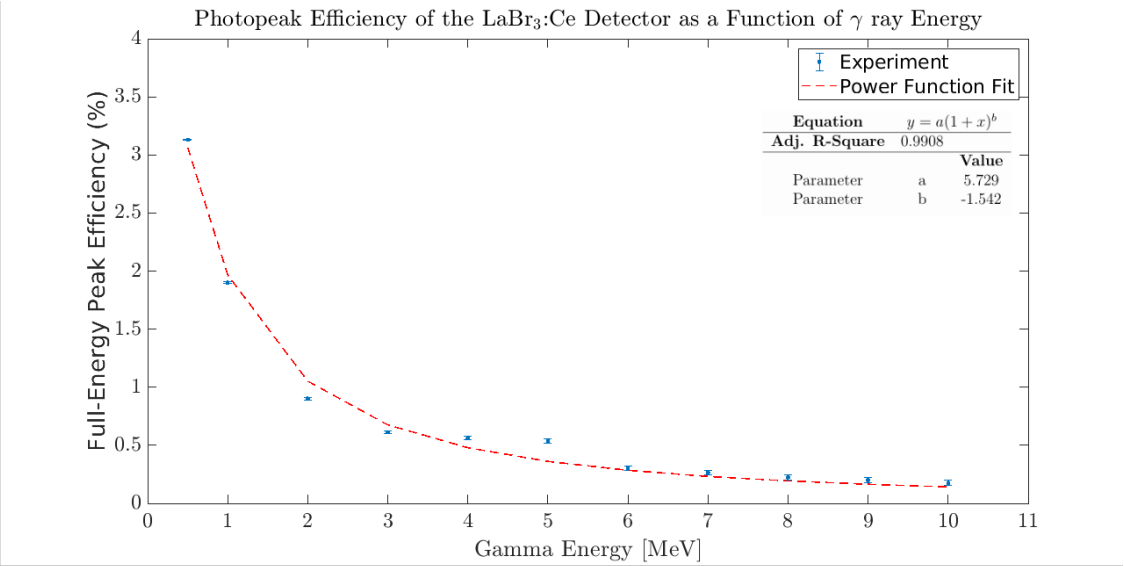

Figure 2.13: Plot of γ Energy vs Photopeak Efficiency of the $LaBr_3$:Ce as measured with a proton beam incident on a ^{60}Co target.

Energy [MeV]	**Photopeak Efficiency (%)**	**Error ($\frac{1}{\sqrt{Counts}}$)**
0.5	3.13	0.00565
1	1.90	0.00725
2	0.902	0.0105
3	0.614	0.0128
4	0.562	0.0147
5	0.536	0.0165
6	0.305	0.0181
7	0.263	0.0195
8	0.225	0.0211
9	0.199	0.0224
10	0.176	0.0238

Table 2.7: Table of photopeak efficiency values as obtained with the $LaBr_3$:Ce detector due to a proton beam at various energies incident on a ^{60}Co target.

2.2.2 Energy Smearing of Simulation Results

Smearing of the energy measurement in the scintillator and readout was applied to the simulation results of energy deposition on the surface of the $LaBr_3$:Ce detector using the detector energy resolution determined in the experiment. The smearing constants were obtained by applying a linear fit to the calibrated energy spectrum of ^{60}Co. Smearing was performed to smooth the energy deposition spectra produced in the TOPAS simulations to take into account the intrinsic characteristics of the $LaBr_3$:Ce detector and electronics used in the experiment. This also allows for more accurate comparisons between data sets (simulation and experimental). This was achieved by finding the sigma value of the energy deposition:

$$\sigma = \frac{a + b\sqrt{E \times 1000}}{1000} \tag{2.5}$$

Where E is energy deposition in keV. The smearing was then calculated by finding the Gaussian spread in the sigma values obtained due to the relative energy resolution of the detector. These smearing values were then added to the initial energy deposition matrix and calculated as seen in Appendix Listing 6. The smearing constants and their associated errors are seen in Fig 2.14.

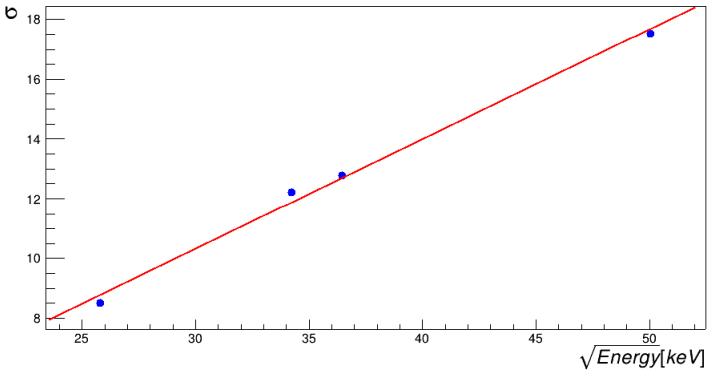

$a = -0.69335 \pm 0.712766$

$b = 0.367334 \pm 0.0189277$

Figure 2.14: Plot of $\sqrt{E}$ vs σ (in units of $\sqrt{keV}$) for the calibrated spectrum of ^{60}Co. The linear fit is seen in red.

2.2.3 Cyclotron Radio-frequency for Detector Noise Reduction in Experimental Measurements

The only drawback of the $LaBr_3$:Ce detector is the background introduced as a result of the internal radioactivity of the detector crystals. This radioactivity is seen in the large peak at 1.436 MeV and the continuum of β and γ attenuation pictured in Fig 2.15. This could limit the prompt γ-rays detection in the low energy region between 1 and 2 MeV if the statistics are very low. This $LaBr_3$:Ce internal radioactivity introduces another source of background to the measured spectra of the experiments alongside the constant source of water background present in the liquid targets due to the interactions of the proton beam.

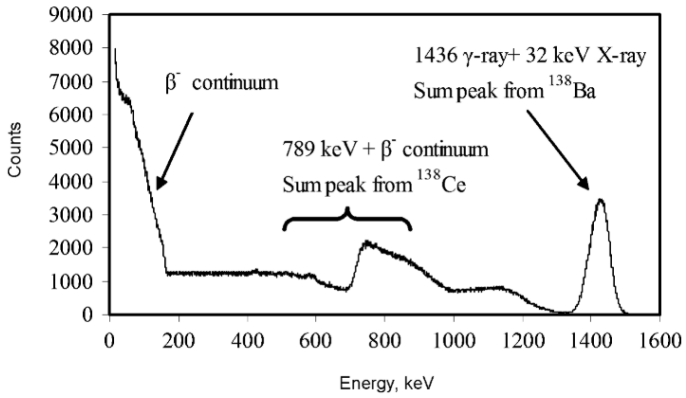

Figure 2.15: Background spectrum of the $LaBr_3$:Ce detector due to its internal radioactivity (taken from (6)).

This can be overcome if the time difference between the event and the RF signal from

the cyclotron is measured. The proton beam is accelerated by the cyclotron such that it is not delivered as a continuous beam, but rather as bunches with a well-defined time structure. In our measurements, the radio-frequency of the cyclotron was set to 106.3 MHz, implying the time structure of the beam to have 9.4 ns intervals between bunches. The prompt γ-rays of interest to this study are emitted in coincidence with the beam when it impinges upon the target.

The detector sees three main signals: (1) the $LaBr_3$:Ce internal radioactivity which is random emission and uncorrelated to the beam (black spectrum), (2) the delayed γ-rays as a result of the beam-target interaction which are emitted in a random time frame such that they are random in the acquisition and uncorrelated to the beam, and (3) the in-sync prompt γ-ray signal which are emitted in a very short time frame ($\approx 10^{-16}$ s) after the interaction of the proton with the target (blue spectrum). Figure 2.16 shows the time in nanoseconds of the detector trigger signal relative to the cyclotron RF signal, plotted against the energy (in keV) of the detector γ rays. One can see blue bunches of in-sync events at a period of 9.4 ns. The green spectrum shows a final prompt γ-ray spectrum without the $LaBr_3$:Ce radioactivity contribution, obtained by subtracting the blue from the red spectrum. All liquid target results to follow in Chapter 3 have this cyclotron RF subtraction implemented.

2.2.4 Data Normalisation

Both experiment and simulation were normalised for both the number of incident protons and bin width. For the experiment, the dead time due to the data acquisition system was $\approx 0.536\%$, which has been corrected for in post-processing. The number of incident protons was calculated for each beam time by using the fact that the cyclotron produced 10^6 particles in the ionisation chamber per 1 nA of current (described in Subsection 2.1.4). A further normalisation which was applied was to the experimental results of the solid targets investigated (^{89}Y and ^{63}Cu) where the geometry issue (beam spot exceeded target geometry) was considered for the normalisation of the spectra (descriibed in Subsection 3.2).

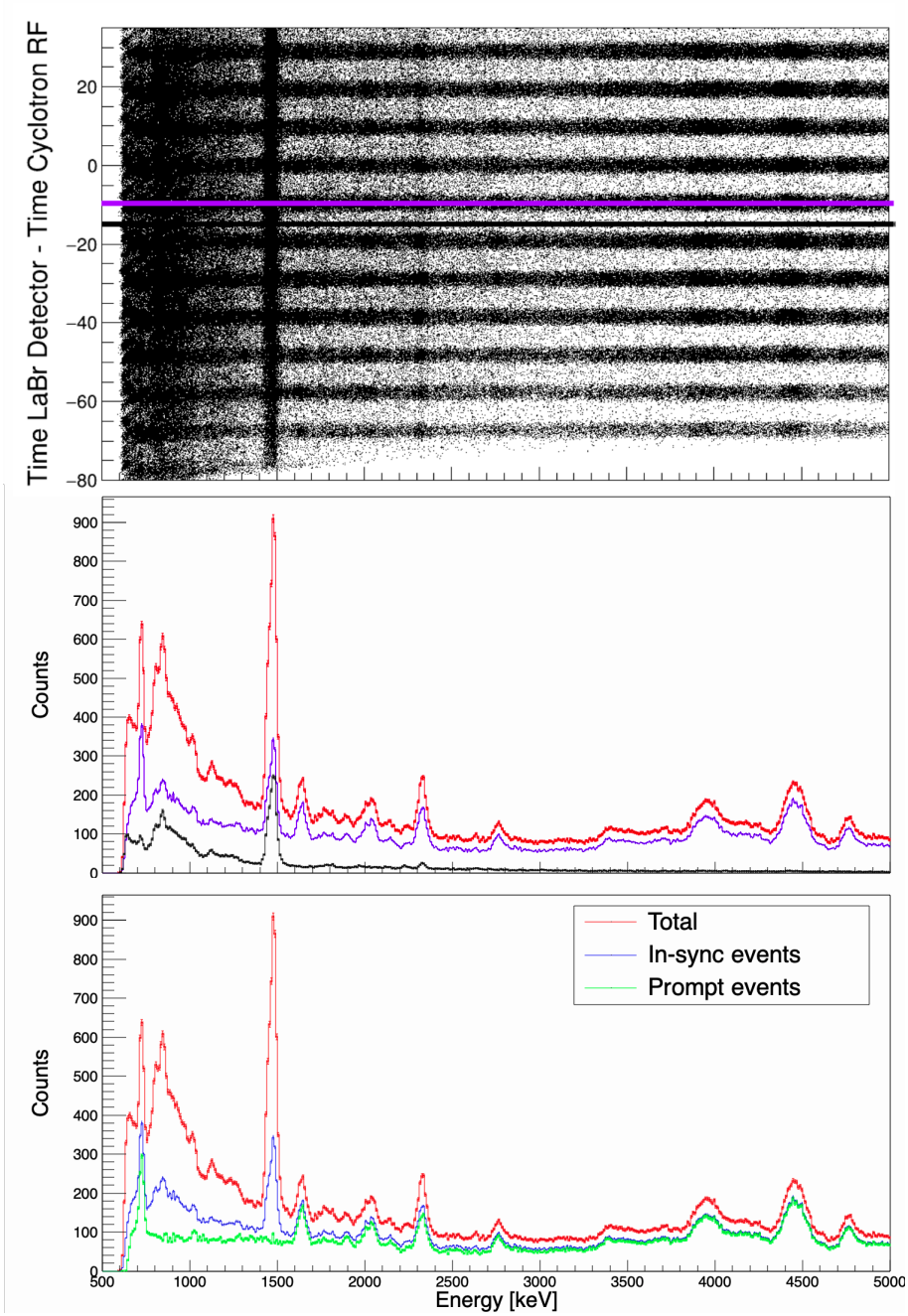

Figure 2.16: Plots showing the blue in-sync, black out-of-sync and the red total energy spectra as seen by the $LaBr_3$:Ce detector when the proton beam is turned on and incident on a water target. **Top**: shows the 2D histogram plots of the signals, where the x-axis shows the energy of the particle from 500 to 5000 keV, and the y-axis shows the time signal subtraction of the cyclotron RF signal from the time at which the $LaBr_3$:Ce sees the event (when it is triggered) in nanoseconds. The blue and black drawn lines correspond to the in-sync and uncorrelated bunches respectively. **Middle**: is the result of integrating the above 2D histogram in time to produce this energy spectrum of the main signals showing the black uncorrelated, blue in-sync and red total spectra. **Bottom**: The green plot shows the prompt γ-ray final spectrum after the black spectrum has been subtracted from the blue spectrum above.

Chapter 3

Results and Discussion

All simulation results presented in this work have been obtained with TOPAS MC v3.6.1 and are validated by experimental data for the selected materials. The accuracy of the TOPAS default physics lists, which is highly documented as the best option for proton therapy dose calculation applications, was investigated by simulating experimental measures performed at Trento Proton Therapy Center, Italy (41). The first idea was to see whether the elements chosen produce characteristic γ-rays which are different from those of water. This was done using solid targets. The idea was then to see if the characteristic prompt γ-ray emission spectrum would remain observable when the concentration of the element was reduced. This was done in the form of liquid targets by loading a water flask tumor volume with this element in a salt form which is known to emit a signature prompt γ-ray spectrum when irradiated with protons, and to then lower the concentration of the element and observe the γ response. The γ energy spectrum generated by the interaction of an approximately mono-energetic 70 MeV proton beam with selected materials was measured experimentally using a $LaBr_3$:Ce detector. Simulations reproducing the experimental set-up were performed and the energy deposition of prompt γ-rays generated by the TOPAS de-excitation models were compared with experimental data.

The methodology employed (see Section 2) made use of PET-like principle (use of markers) such that a non-toxic stable marker was carried in the target volume and then activated by therapeutic radiation. Maximum absorption from the tumor of the marker is key, and detection of the γ-rays emitted by the marker aimed at the production of a signature γ spectrum induced by the proton beam which was different from the background (PMMA and H_2O). This spectrum was generated such that upon arrival of the proton beam, the target nucleus was struck, creating different nuclear reaction products which are left in excited bound states. The excited nucleus will return to its ground state by emitting one or more γ-rays. These γ-ray ultimately interact with the detector volume to produce a measurable signal. They are not considered to interact with the target volume. These γ-ray are then used to determine if the target element/enhancer element was present

in the target volume. Three main elements were studied for this prompt γ-ray response: yttrium, copper, and phosphorus. For a full description of the targets and the associated methodology see Section 2.1.1.

The primary aim of this chapter is to analyse the feasibility of the enhancement element loaded tumor which would not only enhance the production of prompt γ-rays but also emit a signature spectrum. The desired outcome of this enhancement is the existence of defined signature γ-ray peaks at low element concentration. Further, the performance of the TOPAS physics models is assessed by comparing the simulation results to the experimental results. It is important to understand how well the TOPAS MC models perform as the TPS need extensive knowledge of the physical processes to accurately model the interactions of the primary beam with the elements of interest in patient treatments.

The simulation and experimental data plots show the energy deposition of prompt γ-rays originating from the target and seen by the surface of the detector measured in MeV on the x-axis, and the counts are normalised per incident proton number, deadtime and bin width on the y-axis. The bin widths are all calibrated to have 10 keV per channel across all beam times. To reduce computational time, the simulation phase-space environment was stored for neutrons, protons, and γ-rays emitted originating from the liquid target and interacting on the surfaces of the detector (see Appendix, Listing 2). The kinetic energy of the γ-rays as stored in the phase-space files was then used to compute their energy deposition in TOPAS (see Appendix, Listing 3) by means of a user-defined macro (see Appendix, Listings 4 and 5) as explained in Subsection 2.1.5, the spectra of which are seen in the simulation results to follow.

3.1 Background Sources

The $LaBr_3$:Ce internal radioactivity introduces a source of background to the obtained spectra of the experiments alongside the constant source of water background present in the liquid targets due to the interactions of the proton beam. The internal radioactivity is due to naturally occurring radioisotopes ^{138}La and ^{227}Ac, where the main features of this are explained in Subsection 2.2.1.

The experimental energy spectrum shown in red in Fig 3.1 shows the prompt γ-rays emitted due to a 70 MeV proton beam with a large $5 \times 5 \times 5$ cm^3 water box target in a PMMA holder experimentally, plotted against the internal radioactivity of the detector with the proton beam switched on and incident on no target. The range of a 70 MeV proton beam in water is ≈ 4 cm, such that the beam deposits all of its energy in the water box target. The choice of the LaBr3:Ce detector for this analysis is supported by the fact that the characteristic peaks (labelled) of the water+PMMA target are well separated and clearly identifiable. The drawback of the $LaBr_3$:Ce detector is the sharp sum peak due to ^{138}Ba at 1.4 MeV, clearly visible in the black spectrum of Fig 3.1 The presence of this

peak can compromise the detection of γ-rays of energy ≈1.3 to 1.5 MeV. This necessitated the use of the cyclotron radio-frequency for detector noise reduction, which successfully allowed the signal to be discriminated from the background and the $LaBr_3$:Ce noise to be subtracted from the experimental results. This cyclotron RF subtraction is described in Subsection 2.2.3. Furthermore, this allowed for a better comparison between simulation and experimental results.

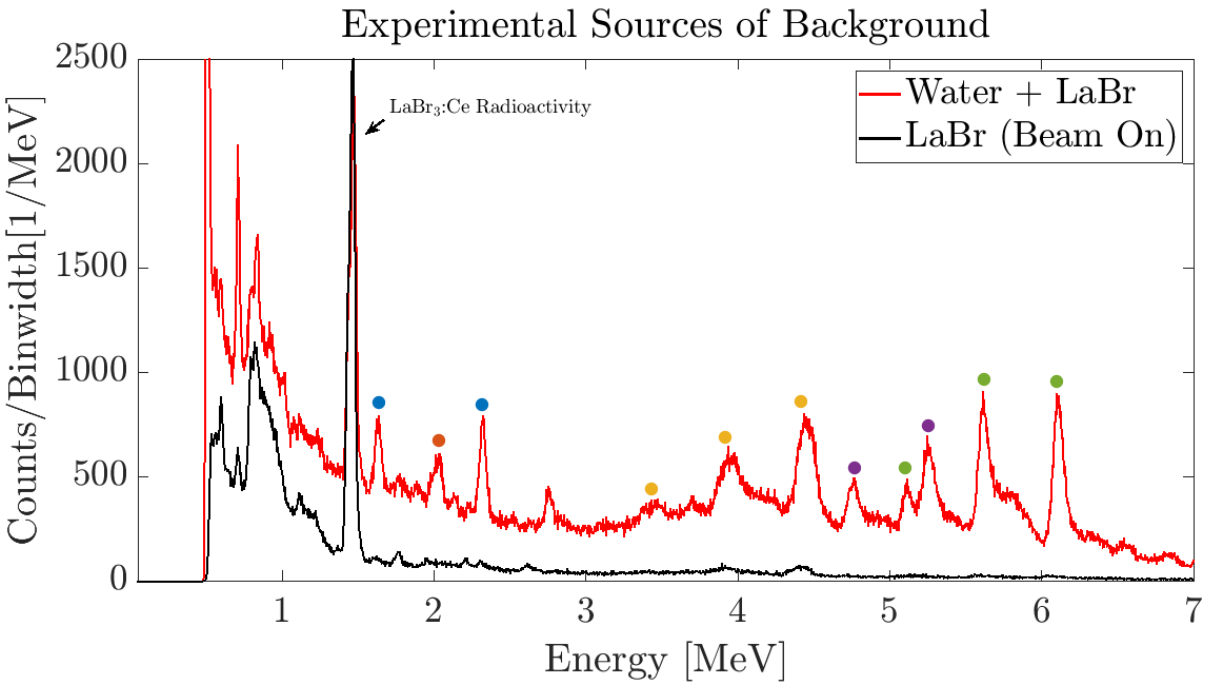

Figure 3.1: Labelled γ energy spectra for the 70 MeV proton beam of the background sources contributing to the experimental background. The red shows the $LaBr_3$:Ce detector radioactivity and water target spectrum, and the black shows the $LaBr_3$:Ce detector beam on without a target present. The labels for each peak are as follows: • $^{14}N^*$, • $^{11}C^*$, • $^{12}C^*$, • $^{15}O^*$, and • $^{16}O^*$.

Water in a PMMA holder was considered in this study as a tissue-equivalent material, as generally used in nuclear medicine experiments, having discrete γ emission peaks from the excited nuclei of ^{12}C, ^{16}O and ^{14}N, the most abundant elements in human tissue. For the liquid target analysis, the water background solution was placed in a 0.226 cm thick PMMA flask and irradiated with the 70 MeV proton beam to quantify the prompt γ-ray spectrum. The prominent discrete prompt γ-ray emission lines are labelled in Fig 3.2. Note that for this measurement the cyclotron RF was used during the experiment to remove the random coincidence background (see Subsection 2.2.3 for a full description of the methodology employed). The TOPAS simulation was generated of the experimental set-up, taking into account the molar mass fractions of the water and the PMMA material.

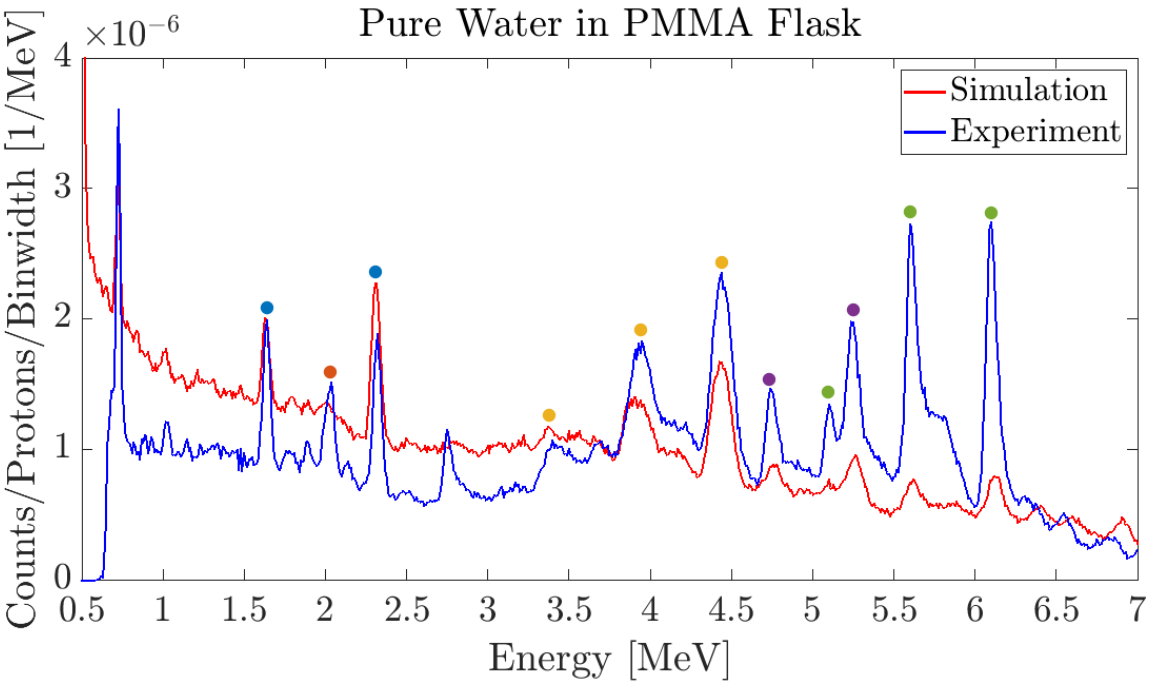

Figure 3.2: Comparison of simulation results and a background subtracted experimental spectrum for the 70 MeV proton beam of the γ energy spectrum of the liquid water target in the PMMA flask. Labelled are the prompt γ-ray emission lines and their single and double escape peaks from the major constituent elements (nitrogen, carbon and oxygen) of the water. The labels for each peak are as follows: • $^{14}N^*$, • $^{11}C^*$, • $^{12}C^*$, • $^{15}O^*$, and • $^{16}O^*$.

Figure 3.2 shows a good correlation between the simulation and experimental results which are more distinguishable and with a greater yield of peaks in the 3 - 8 MeV region of the experimental results. The prominent 4.46 MeV γ-ray from the $^{12}C(p,p')^{12}C^*$ reaction is shown, emitted by the de-excitation of the first excited state of the element, the only known particle-bound excited state of ^{12}C (45). The $^{12}C^*$ single escape peak at 3.96 MeV shows a similar trend for both spectra. The double escape peak at 3.42 MeV shows a weak intensity in the simulation results when compared to the peak of the experimental results. Furthermore, the inelastic nuclear scattering between the oxygen nucleus present in water and a proton ($^{16}O(p,p'\gamma)^{16}O^*$) produces a known peak at 6.11 MeV, which is observed in both spectra. The prompt γ-ray emission lines at 5.62 MeV (first escape peak) and 5.11 MeV (double escape peak) are seen in both spectra, with the double escape peak exhibiting a smoother distribution in the simulation results. The 2 MeV emission peak is due to the reactions $^{12}C(p,X)^{11}C^*$ and $^{16}O(p,X)^{11}C^*$ originating from the interaction of the incident proton beam with the water target. As described in the methodology (see Subsection 2.1.5), the PMMA energy deposition spectrum is not included in the simulation spectrum and thus this peak does not appear in the simulation results as it does not originate from

water (46). The $^{14}N^*$ peak at ≈1.6 MeV shows good agreement between simulation and experiment as this peak originates from the interaction with the incoming beam with the water as $^{16}O(p,x)^{14}N^*$. Further data is provided in Table 3.1 on the γ emission due to a water target.

Another attribute observed in Fig 3.2 is the width of the carbon peaks when compared to the other characteristic peaks. This is due to the ^{12}C nuclei being lighter in mass, resulting in larger recoil velocities (47). Further, the half-life of the ^{12}C 2^+ state is approximately 0.43 ps, much shorter than that of the ^{16}O 3^- state which gives rise to the 6.11 MeV emission of 18.4 ps. This allows for more decay to occur in-flight at higher velocities, resulting in an elevated Doppler broadening in the carbon emissions when compared to those of oxygen. This broadening seems to be accurately predicted by the TOPAS MC model. There is a discrepancy between the simulation and experimental results seen in the higher experimental prompt γ-ray yield after 3.5 MeV which is not predicted in the simulation. The mass fractions for water and PMMA are in agreement in both data sets, suggesting that there is a possible inaccuracy in the TOPAS physics list in predicting the prompt γ-ray response at higher energies. What was found was the cross section of carbon and oxygen as implemented in the TOPAS physics lists were not in agreement with experimental data, which is demonstrated by the differences in the absolute yield, a difference factor of ≈ 2.

Overall, in terms of the emission peaks, energy deposition, and the response of the detector, the simulation and experimental results are in good agreement in the low-energy region of interest. This is emphasized in Table 3.2 where, when taking the percentage ratio of their normalised counts, the 1.64 MeV water peak in simulation and experiment agree within 1.64%. This agreement worsens as the energy increases, with a discrepancy of 70.186% at 6.13 MeV.

Although not a source of background, the dead time of the detector due to the DAQ system was 0.536% for the experimental results where the cyclotron RF signal was used for background subtraction. The dead time is, however, not to be attributed to the difference in yield obtained when comparing simulation and experiment as the dead time has been corrected for in the post-processing.

3.2 Prompt γ-Ray Response of Solid Targets

The prompt γ-ray response of the elements of interest was investigated by irradiating solid targets with a 70 MeV proton beam. The goal of this part of the project was to determine the prompt γ-ray yield of each element at a very high concentration to characterise the emission spectra and to estimate the viability of its performance once the concentration is reduced. These non-toxic isotopes are already utilized in various ways for diagnostic or beam therapy in clinics. Copper has many radiotherapy applications

Target	Emitted Residual	E_γ [MeV]	Transition
^{12}C	^{12}C*	4.44	2^+ 4.44 $\rightarrow$ 0^+ g.s.
	^{11}C*	2.00	$\frac{1}{2}^-$ 2.00 $\rightarrow$ $\frac{3}{2}^-$ g.s.
^{16}O	^{16}O*	6.13	3^- 6.13 $\rightarrow$ 0^+ g.s.
		6.92	2^+ 6.92 $\rightarrow$ 0^+ g.s.
		7.12	1^- 7.12 $\rightarrow$ 0^+ g.s.
		2.74	2^- 8.84 $\rightarrow$ 3^- 6.13
	^{12}C*	4.44	2^+ 4.44 $\rightarrow$ 0^+ g.s.
	^{15}N*	5.27	$\frac{5}{2}^+$ 5.27 $\rightarrow$ $\frac{1}{2}^-$ g.s.
^{14}N	^{14}N*	1.64	1^+ 3.95 $\rightarrow$ 0^+ 2.31
		2.31	0^+ 2.31 $\rightarrow$ 1^+ g.s.
		5.11	2^- 5.11 $\rightarrow$ 1^+ g.s.
		0.73	3^- 5.83 $\rightarrow$ 2^- 5.11
		3.38	1^- 5.69 $\rightarrow$ 0^+ 2.31
		2.79	2^- 5.10 $\rightarrow$ 0^+ 2.31
		3.89	1^+ 6.20 $\rightarrow$ 0^+ 2.31

Table 3.1: A list of candidates for γ rays detected originating from a water target and inside PMMA flasks (g.s. = ground state) (9).

	Normalised Counts		
Water Peak [MeV]	Simulation	Experiment	Disagreement [%]
1.64	2.0205×10^{-6}	1.9958×10^{-6}	1.24
4.44	1.6907×10^{-6}	2.3537×10^{-6}	28.17
5.27	9.5802×10^{-7}	1.9766×10^{-6}	51.53
6.13	8.18125×10^{-7}	2.74412×10^{-6}	70.186

Table 3.2: Counts for the main peaks of water and their associated agreement as measured in simulation and experimental results.

including characterization of tumor hypoxia in PET therapy, and phosphorus and yttrium isotopes, especially ^{90}Y, are utilized in radioisotopic therapy and well as for radioimmunotherapy (48).

Experiments were performed on a ^{89}Y rod and ^{nat}Cu solid targets at the Trento PT Center in Trento, Italy (see Subsection 2.1.2 for information regarding target geometry and set-up). An experimental analysis could not be performed on ^{31}P as the isotope is difficult to manufacture (see Section 3.2). The TOPAS simulations performed implemented the experimental set-up and geometries, except for the target holder which was not included in the simulation. Simulations were performed using ^{89}Y, ^{nat}Cu and ^{31}P solid targets. Although experiments could not be conducted with the phosphorus isotope, it was valuable to obtain simulation results of the prompt γ-ray spectrum as the ^{31}P target was identified as a candidate element early in this study when research demonstrated its

known therapeutic application, as well as the abundance of low energy prompt γ-ray peaks (49) (50). Energy smearing (see Subsection 2.2.2) was applied to the energy deposition of the prompt γ-rays on the surface of the detector to account for the resolution of the detector and improve the comparison between data sets. This was done by using the response function of the FWHM of the detector as a function of energy as obtained in the calibration of the detector, ensuring that the simulation accurately portrays the energy deposition of a $LaBr_3$:Ce detector. The good performance of this procedure can be seen in the agreement of FWHM between the peaks of simulation and experiment in the results to follow. The experimental and simulation results are presented for each element (^{nat}Cu Subsection 3.2.1, ^{89}Y Subsection 3.2.2 and ^{31}P Subsection 3.2.3) while the comparison of the results obtained is discussed in Subsection 3.2.4.

3.2.1 Natural Copper Solid Target

A solid copper rod of material density 8.96 $\frac{g}{cm^3}$ was irradiated by 21.86×10^9 70 MeV protons in the experimental room and 2×10^9 protons in simulation. Copper has a natural composition of both ^{63}Cu (69.345%) and ^{65}Cu (30.365%), therefore both isotopes of copper contribute to the overall signature present. The results are shown in Fig 3.3. To best perform an absolute comparison between data sets the counts were normalised by the number of incident protons and a bin width of $\approx$ 10 keV. Unfortunately, for these experimental results, it was not possible to implement the correlation of the event with the cyclotron RF, resulting in more low energy background which engulfs the corresponding low energy signal originating from the target. The peak at 1.44 MeV in Fig 3.3 (top) corresponds to the $LaBr_3$:Ce detector internal radiation which has not been subtracted from solid target experimental results. The production of prompt γ-rays, as seen in Fig 3.3, shows no distinct prompt γ-ray production after 1.4 MeV nor at higher energies. For the purpose of this study, high energy ($>$ 8 MeV) would have been preferred as the signal-to-noise ratio in this region would be high when discriminating from the background peaks originating in water in human tissue. High energy prompt γ-rays would, however, be less favourable from a detection efficiency point of view.

The low energy ($<$ 2 MeV) region of the plot demonstrates a signature of peaks due to the ^{63}Cu and ^{65}Cu isotopes present in the material, namely: ^{63}Cu* at 0.979 and 1.33 MeV, ^{65}Cu* at 1.04 and 1.11 MeV, and ^{65}Cu(p,α)^{62}Ni* at 1.17 MeV. These peaks were identified using the NuDat database (7) and cross-checked using TALYS (5) by simulating the nuclear reaction of the secondary γ-ray fragments, seen in Figs. 3.3 (middle) and 3.3 (bottom). These TALYS simulations were also conducted at the 20 MeV beam entrance value to gain understanding into all energies of the proton interactions with the target in the experiment. This is due to the fact that in experiment there are several energy values of the beam for which reactions take place. The peaks produced, as predicted by TALYS, at 20 MeV were consistent with those at the 70 MeV BP position, but with lower cross section population. As the populated peaks are the same, only the 70 MeV results are

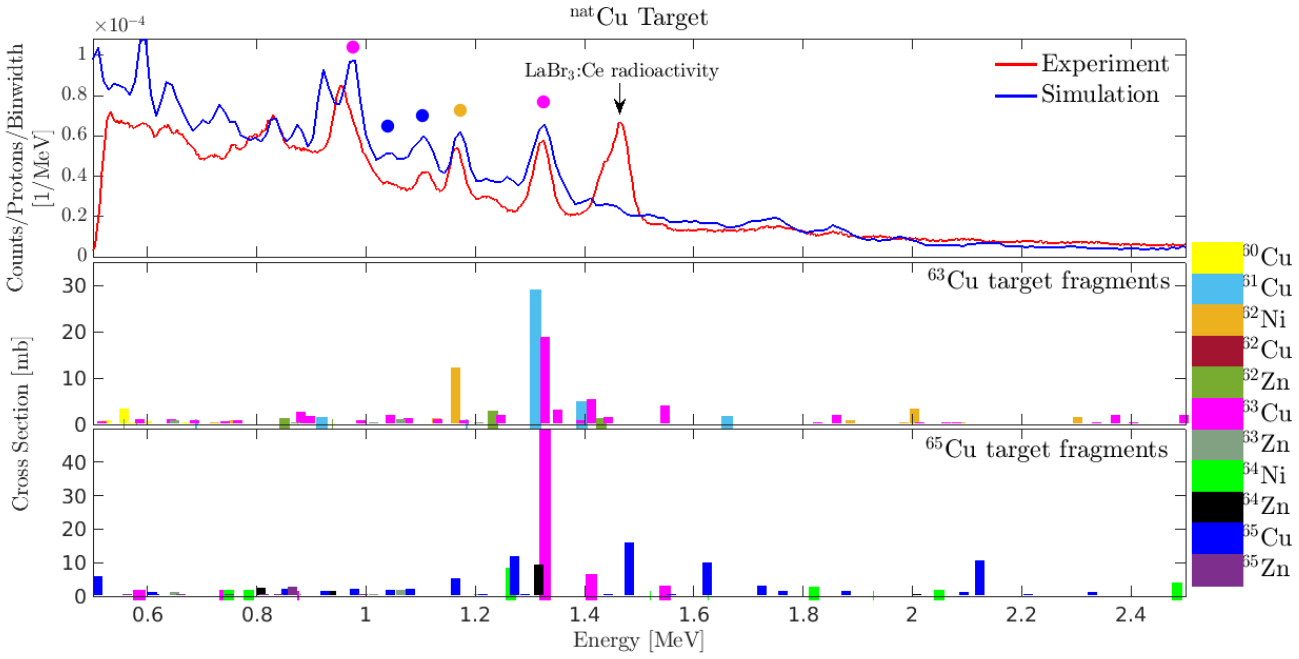

Figure 3.3: Plots pertaining to the prompt γ-ray peaks present in the low energy range of ^{63}Cu. Top: Results obtained for solid target of natural copper. Labelled are the γ emission lines of the isotope. The labels for each peak are as follows: • ^{63}Cu* , • ^{65}Cu* , and • ^{62}Ni*. Middle: TALYS results of the γ-decay fragments due to the irradiation of a ^{63}Cu target by a 70 MeV proton beam. Bottom: TALYS results of the γ-decay fragments due to the irradiation of a ^{65}Cu target by a 70 MeV proton beam.

shown. The largest enhancement contributions originate from two of the first three excited states of copper at 0.9 and 1.3 MeV which show a good correlation in both yield and cross section, demonstrating that the TOPAS MC model is accurate in predicting the discrete γ-ray population. Further, these peaks are also in the region where the water background is less prominent making the natural copper element a good marker candidate.

3.2.2 Natural Yttrium Solid Target

A solid yttrium rod of material density 4.472 $\frac{g}{cm^3}$ was irradiated by 14.5×10^9 70 MeV protons in the experimental room, and 2×10^9 protons in simulation. The results are shown in Fig 3.4. The investigated tracer, ^{89}Y, is the only stable isotope of yttrium with a 100% natural abundance. To best perform an absolute comparison between data sets the counts were normalised by the number of incident protons and a bin width of ≈ 10 keV. Background subtraction of the radioactivity of the detector was not performed for the experimental results of this target, resulting in more low energy background which

engulfs the corresponding low energy signal originating from the target. The prompt γ-ray response of the yttrium target is quite different from that seen in the copper target. There are distinguishable peaks that are seen in both the simulation and experiment, however, the cross section of these peaks is low, as is the resolution seen in the experimental results. Although the overall spectrum does not show a very good agreement between simulations and experiments, some characteristic peaks of Y were identified. The signature prompt γ-ray peaks, as labelled in Fig 3.4 (top) with colors which correspond to the legend on the right hand side, are ^{89}Y(p,t)^{87}Y* at 0.797 MeV, ^{89}Y(p,2p)^{88}Sr* at 0.866 MeV, ^{89}Y(p,nγ)^{89}Zr* at 0.947 MeV, ^{89}Y(p,2nγ)^{88}Zr* at 1.07 MeV, and ^{89}Y(p,p'γ)^{89}Y* at 1.275 MeV. These peaks correspond to those predicted by the TALYS plot, seen in Fig 3.4 and verified with NuDat database (7). These TALYS simulations were also conducted at the 20 MeV beam entrance value to gain understanding into all energies of the proton interactions with the target in the experiment. This is due to the fact that in experiment there are several energy values of the beam for which reactions take place. The peaks produced, as predicted by TALYS, at 20 MeV were consistent with those at the 70 MeV BP position, but with lower cross section population. As the populated peaks are the same, only the 70 MeV results are shown.

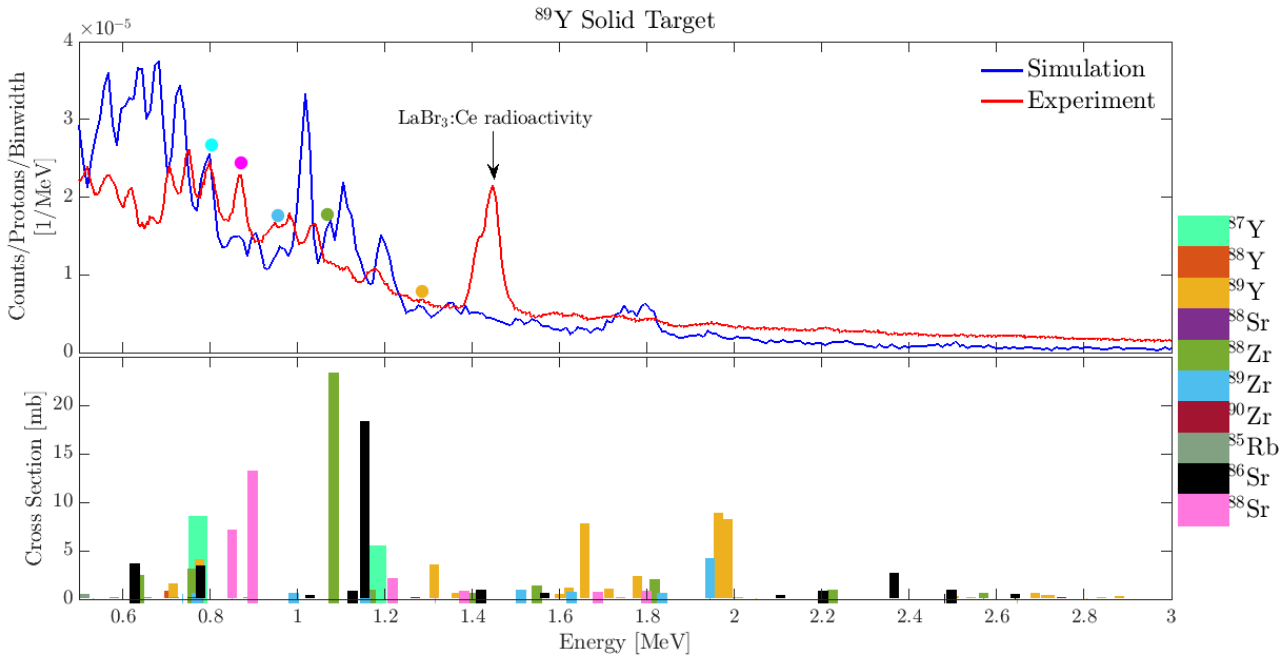

Figure 3.4: Plots pertaining to the prompt γ-ray peaks present in the low energy range of ^{89}Y. Top: Results obtained for solid target of natural copper. Labelled are the γ emission lines of the isotope. The labels for each peak correspond to the legend. Bottom: TALYS calculation showing the γ decay fragments resulting from the irradiation of a ^{89}Y target by a 70 MeV proton beam.

The ^{89}Y target produced a high number of peaks densely populating the low energy region. This is due to the probability of p + ^{89}Y producing heavy fragments from which a greater yield of prompt γ-ray is expected. The discrepancy between simulation and experimental results could be related to the high level density of ^{89}Y, allowing a general enhancement of the prompt γ-rays production while hindering a clear distinction of individual γ-ray peaks. The information from sources such as the NuDat database (7) might not provide comprehensive information on all of the decay products which contribute to the peaks seen in the plots. High energy peaks were not observed with the yttrium target.

3.2.3 ^{31}P Solid Target

A solid phosphorus box ($5 \times 5 \times 5$ cm^3) of material density 1.82 $\frac{g}{cm^3}$ was irradiated by 2×10^9 70 MeV protons in simulation. Experimental measures were not performed in correspondence with the simulations for reasons explained in Subsection 3.2. There are many isotopes of phosphorus, however, only ^{31}P is stable and was selected for its 100% natural abundance. The labelled simulation results are shown in Fig 3.5(top).

The TALYS calculation results of this isotope (see the bottom panel of Fig 3.5) pointed toward many individual γ-ray peaks of high cross section in the low energy region. The 70 MeV TALYS calculation did not provide a complete portrayal of the prompt γ-ray energy spectrum illustrated in the simulation. For this reason, the 20 MeV entrance energy value of the beam was investigated in comparison to the 70 MeV energy at the Bragg peak position. This is due to the fact that in experiment there are several energy values of the beam for which reactions take place. The peaks of interest identified in the simulation were ^{31}P(p,p'γ)^{31}P* at 1.14, 1.278 and 1.395 MeV, ^{31}P(p,nγ)^{30}P* at 1.4592 and 2.0256 MeV, ^{31}P(p,pγ)^{30}Si* at 1.54 MeV and ^{31}P(p,α)^{28}Si* at 1.783 MeV. The peak at 2.23 MeV is due to the reaction ^{31}P(p,γ)^{32}S*, where the second state decays via the first state ^{32}S(p,p'γ)^{32}S* at 2.23 MeV 3.5(top). The majority of these peaks have good intensity and a high cross section at high concentration.

The ^{31}P target exhibits many low energy prompt γ-ray emission lines, making it a good candidate for prompt γ-ray enhancement calculations. When comparing the prompt γ-ray response of yttrium to that of phosphorus, although both spectra obtained via simulation show promising cross section in their peaks, the peaks of the phosphorus target are more separated, suggesting that they are likely to remain distinguishable once the concentration has been reduced.

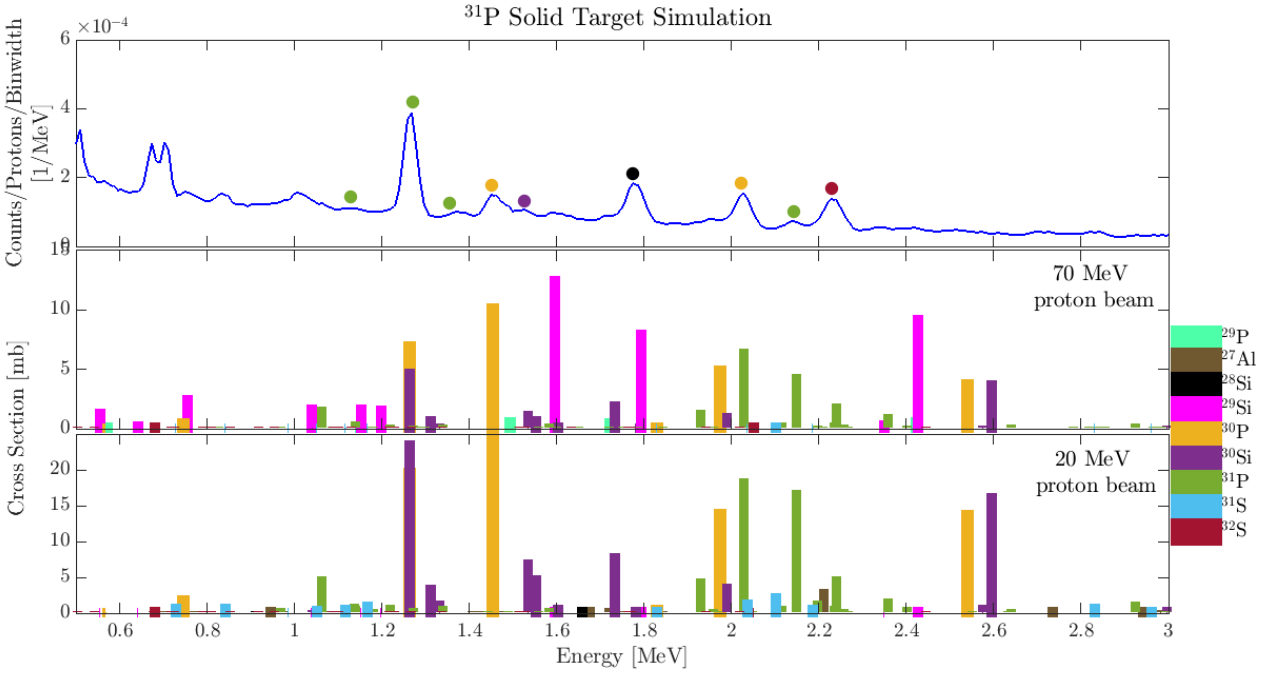

Figure 3.5: Plots pertaining to the prompt γ-ray peaks present in the low energy range of ^{89}Y. Top: Results obtained for solid target of natural phosphorus. Labelled are the γ emission lines of the isotope. The labels for each peak are as follows: ● ^{31}P*, ● ^{30}P*, ● ^{30}Si*, ● ^{28}Si*, and ● ^{32}S*. Middle: TALYS calculation showing the γ decay fragments resulting from the irradiation of a ^{31}P target by a 70 MeV proton beam. Bottom: TALYS calculation showing the γ decay fragments resulting from the irradiation of a ^{31}P target by a 20 MeV proton beam.

3.2.4 Overview of Solid Target Results

The solid targets investigated at their natural concentration for their prompt γ-ray enhancement were ^{nat}Cu, ^{89}Y and ^{31}P. The rationale for this investigation was to obtain insight into the feasibility of using the prompt γ-ray response of these targets as enhancement elements in tumors. Figures 3.6 and 3.7 show the spectra of the solid targets plotted with that of the water target for experiment and simulation respectively. The $\approx$ 1.4 MeV peak which is observed in experimental spectra is due to the internal radioactivity of the $LaBr_3$:Ce detector. All three isotopes exhibited ideal signature spectra that can be distinguished from the water background response and, as such, are investigated further in selected salt form in the following Section 3.3.

It is observed that although all three materials performed as desired, the ^{nat}Cu and ^{31}P targets showed prompt γ-ray peaks which are easier to distinguish from one another than those observed due to ^{89}Y. This behavior offers foresight into what one may expect at a

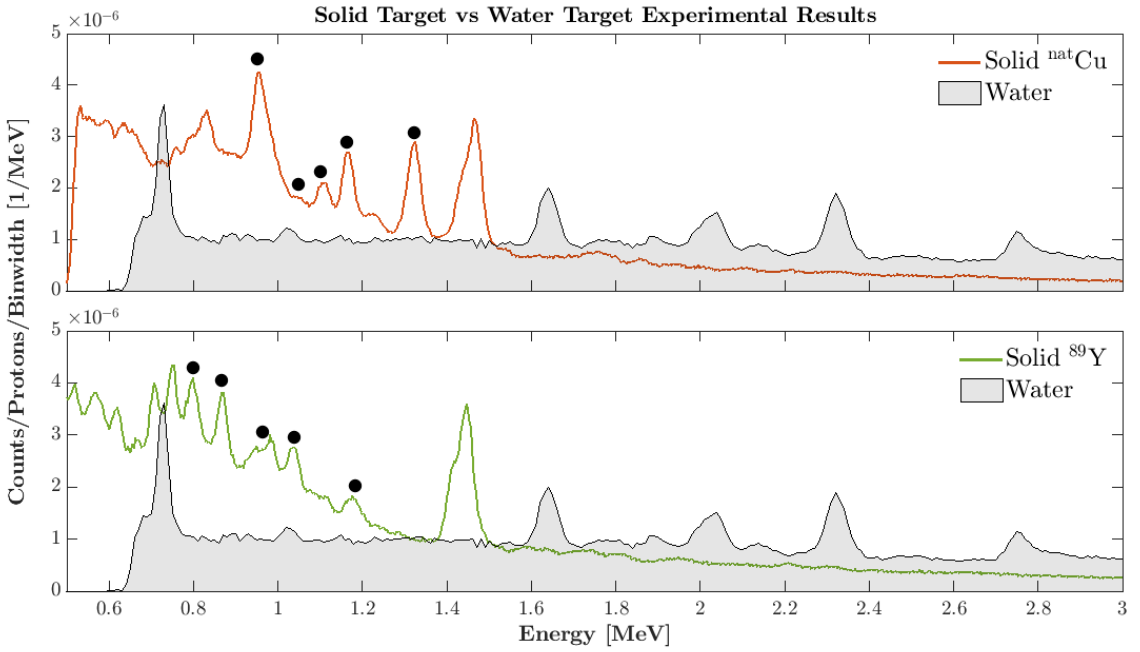

Figure 3.6: Experimental results of solid target spectra (^{nat}Cu and ^{89}Y) vs water. The black dots (•) represent the identified signature prompt γ-ray peaks of interest for each target. The spectrum of ^{nat}Cu has been scaled by a factor of 20 and ^{89}Y by a factor of 3 for comparison purposes.

much lower concentration, implying that the yttrium peaks, although present, may become more difficult to observe. All three targets experience the highest cross sectional prompt γ-ray yield in the region between ≈0.8 and 1.4 MeV. This region will be investigated in performing a quantitative comparison between prompt γ-ray enhancement in the liquid salt form of these targets in the results to follow. The regions, as obtained in the experiment, of the highest cross sectional prompt γ-ray response identified are highlighted in Figs. 3.6 and 3.7 by the black dots labelling the signatures of interest for each material. The simulation results for ^{31}P predicts a very high cross section signature at 1.27 MeV. Although some of the signature peaks of ^{31}P are situated in the region $>$ 1.4 MeV, there exist sufficient peaks and with good cross section in the 0.8 to 1.4 MeV region. Figures 3.6 and 3.7 show that if the region of interest was extended, it would begin to include strong background signal originating from water and PMMA such as the ^{16}O(p,x)^{14}N* and ^{14}N(p,p')^{14}N* peak at ≈ 1.64 MeV.

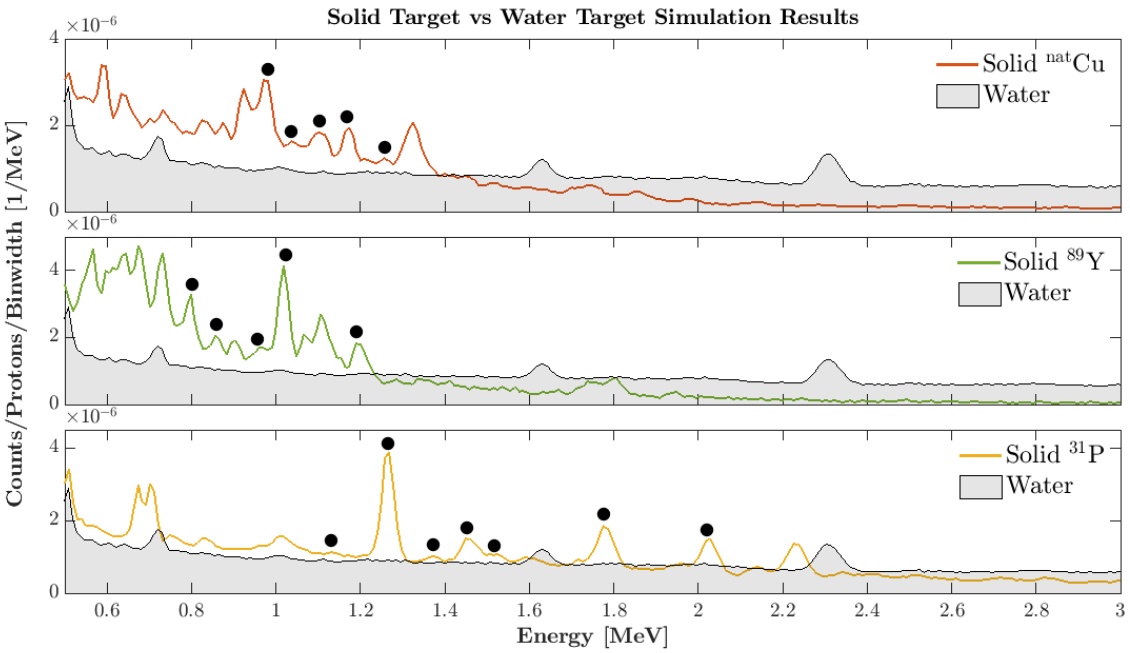

Figure 3.7: Simulation results of solid target spectra (^{nat}Cu, ^{89}Y and ^{31}P) vs water. The black dots (•) represent the identified signature prompt γ-ray peaks of interest for each target. The spectrum of ^{nat}Cu has been scaled by a factor of 1.6, ^{89}Y by a factor of 0.8 and for comparison purposes.

3.3 Prompt γ-Ray Response with Liquid Salt Targets

The prompt γ-ray response of the elements of interest was investigated by irradiating liquid salt targets with a 70 MeV proton beam. Copper sulfate pentahydrate ($CuSO_4$+$5H_2O$), Yttrium(III) Nitrate Hexahydrate ($Y(NO_3)_3$+$6H_2O$) and Sodium Dihydrogen Phosphate Monohydrate (NaH_2PO_4+H_2O) were chosen as the non-toxic salt compounds of the isotopes of interest, discussed in Section 2.1.3. The molar mass fractions of these salts at $\approx 5\%$, $\approx 1\%$ and $\approx 0.5\%$ was calculated and they were then dissolved in 100ml of pure water. The solutions at the three concentrations for each of the three salts were placed in two face-to-face PMMA flasks each containing the same solution.

The simulations were performed to reproduce the experimental set-up (see Subsections 2.1.4 and 2.1.5 for information regarding experiment and simulation methodologies respectively). An absolute comparison of the TOPAS MC simulations and the prompt γ-ray experimental measurements is presented in this section. An aspect of this work is to provide validation of the simulations, therefore a comparison of results was done using the number of discrete prompt γ-rays detected per incident proton hitting the target. In the TOPAS simulation, scaling the results by prompt γ-rays is straightforward as the proton number is provided in the simulation set-up. The number of primary incident protons in the experiment was obtained by using the ionisation chamber to count, and cross checked by the fact that the cyclotron produced 10^6 protons per 1 nA of current as measured in the ionisation chamber.

At the highest concentration, the mass fraction is just over 5%, making more or less 5% of the tumor composition the tracer isotope of interest. Although this mass fraction would be not be realistic in a therapeutic measurement, it is a good benchmark to observe the γ response of the salts before investigating lower concentrations. The high concentration was to demonstrate the observable γ response of the salts such that when the concentrations were reduced, there would be an understanding of the signal lost. The concentrations were scaled down by ten percent, and then scaled down further to gauge a minimum concentration at which a prompt γ-ray signature can still be detected. The lowest concentrations studied were between $0.6 - 0.8\%$ of the isotope of interest.

3.3.1 $CuSO_4$+5H_2O Liquid Target

The $CuSO_4$+5H_2O salt was dissolved at molar concentrations of 1M, 0.2M and 0.1M in 100ml of H_2O, where the corresponding mass fractions are shown in Fig 3.8. The aim was to characterise the prompt γ-ray response of the salt at a high concentration ($\approx$ 5% ^{nat}Cu), after which the concentration was lowered and the feasibility of using the tracer was quantified by its enhancement capabilities.

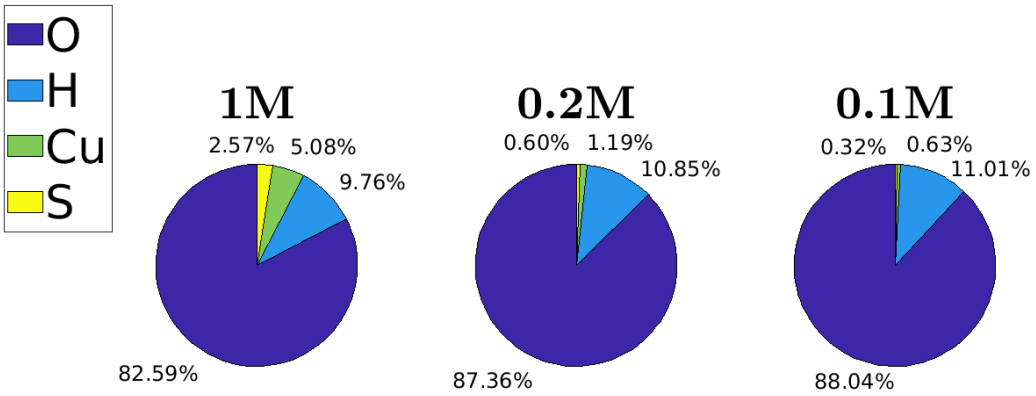

Figure 3.8: Mass fractions for the three investigated molar masses of $CuSO_4$+5H_2O in 100 ml of pure water.

Figure 3.9 shows the experimental and simulation results of all three concentrations of $CuSO_4$, the water plus the element being studied in salt form. The dead time is apparent in the low energy range difference seen when comparing the simulation results to the experimental results. The identified peaks correspond to prompt γ-ray signatures which are present in both the solid target with the highest natural abundances of ^{63}Cu and ^{65}Cu isotopes, and the 1M solution with a ^{nat}Cu mass fraction percentage of 5.08%. The majority of the observed γ-rays are attributed to the transitions from the excited states of ^{63}Cu and ^{65}Cu which were abundant in both the solid and 1M liquid target. These peaks were brought about by the inelastic scattering of protons. The peaks which exhibit the highest prompt γ-ray response are labelled by colour, where the associated reactions are: ^{63}Cu(p,p'γ)^{63}Cu* at 0.965 and 1.34 MeV, ^{65}Cu(p,p'γ)^{65}Cu* at 1.025 and 1.125 MeV and ^{65}Cu(p,α)^{62}Ni* at 1.175 MeV by decay of the two most abundant isotopes of copper in the molecule. These five signature peaks are of good FWHM (the first and second peak are not easily discernible from one another as two peaks have merged to create one larger peak) are present in the 1M solution due to the de-excitation of the two isotopes of copper at high mass fraction, where the presence of these peaks guarantee that the proton has

interacted with the tracer element within the tumor region. The sixth peak, seen in red at 2.23 MeV is due to the excited state of ^{32}S, originating due to its presence in the salt molecule. The de-excitation levels were cross-checked against the NuDat database (7) and TALYS simulation results (seen in Subsection 3.2.1). The number of incident protons in simulation and experiment can be seen in Table 3.3.

	Concentration		
	1M	**0.2M**	**0.1M**
Simulation	2×10^9	4×10^9	1×10^{11}
Experiment	8.73×10^9	2.45×10^{10}	2.47×10^{10}

Table 3.3: Number of incident protons as used in simulation and experiment for the $CuSO_4$ targets.

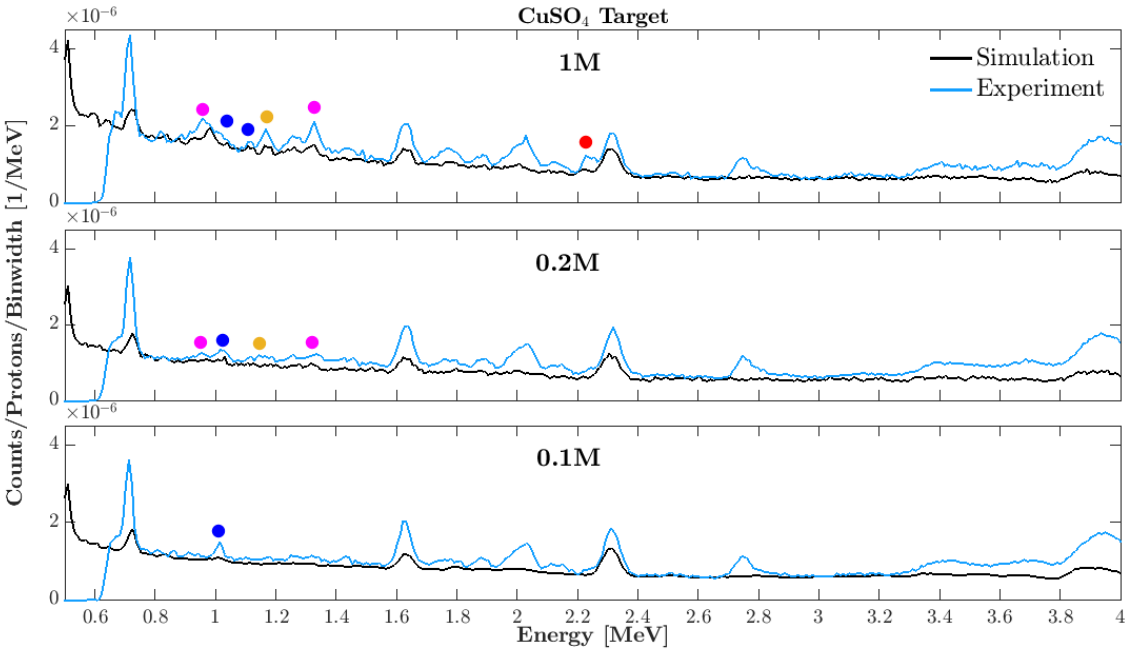

Figure 3.9: Simulations vs background subtracted experimental results for the $CuSO_4$ liquid target at high, medium and low concentration. The labelled peaks correspond to the following fragments: • ^{63}Cu*, • ^{65}Cu*, • ^{62}Ni*, and • ^{32}S*.

The agreement between the experimental and simulation results is best seen in the 1M high concentration of the solution (top panel of Fig 3.9). Here, each of the five peaks identified in experiment are predicted by the TOPAS physics lists and with a good agreement in cross section and FWHM, suggesting that the TOPAS MC model has a good grasp of the nuclear structure. The middle panel of Fig 3.9 shows the results of the experiment and simulation once the concentration has been reduced by $\approx 10\%$. Four of the signature peaks are seen labelled, where one observes that only the first excited states

of ^{63}Cu and ^{65}Cu remain as discernible peaks in the experiment. The other identified peaks retain their high cross section but are seen as an energy continuum at 0.17M are are not easily distinguishable in experiment. Comparing this medium concentration to the spectrum predicted by simulation, one sees that only the first excited state of ^{65}Cu remains as a small peak. At 0.1M, seen as the bottom panel in Fig 3.9, only the first excited state of ^{65}Cu at 1.025 MeV remains as a sharp peak in experiment. Overall, the reduction in concentration saw the agreement between simulation and experiment worsen in predicting the FWHM and yield of the peaks of interest. At the lowest yield the prompt γ-ray signature is nearly indiscernible from the background, behaviour which was not seen in the experimental results. The physics lists are not robust for this target at low mass concentrations.

Figures 3.10 and 3.11 show the prompt γ-ray spectra of the solid ^{nat}Cu rod target plotted with the results of the 1M solution of $CuSO_4$ (with the PMMA flask for experiment) and the water background (with the PMMA flask for experiment). The water background is pictured as a grey shaded region to better differentiate the prompt γ-ray response of the ^{nat}Cu tracer element from that of water. The middle and bottom panels of each of these Figs. 3.10 and 3.11 show the prompt γ-ray spectra of the middle and low concentration solutions of $CuSO_4$ (with the PMMA flask for experiment) and the water background (with the PMMA flask for experiment).

In the first panel of the experimental results plotted in Fig 3.10, the identified ^{nat}Cu peaks at highest natural concentration have reduced considerably in FWHM when compared to those of 1M concentration $CuSO_4$ solution. The 1M solution is a very high concentration of the copper tracer element, an unrealistic scenario in PT, however it is interesting to quantify the prompt γ-ray response at high concentrations before reducing the concentration to gauge the prompt γ-ray response at lower concentrations of the isotope. In the high energy range (> 3.5 MeV) of Fig 3.9 the presence of the prompt γ-ray signature is low as the water dominates the spectrum and, thus, prompt γ-ray enhancement is not easily observed. The exception to this is seen at 2.23 MeV as the ^{32}S peak originating due to its presence in the salt molecule. The region where the prompt γ-ray signature is most distinguishable from the water background is between 0.9 and 1.5 MeV, as was identified in Fig 3.9, where one observes that the yield is the highest observable for this solution. The high concentration 1M solution retains the peaks identified in the solid target, where the enhancement of the tracer element, seen as the white space between the spectrum of the salt and the background spectrum, is great. At highest concentration, the prompt γ-ray response of the tracer in the solution shows sharp distinguishable peaks which are easily discriminated from the background spectrum.

The middle panel shows the prompt γ-ray spectrum of the 0.2M $CuSO_4$ solution compared to the background, and the bottom panel shows the prompt γ-ray spectrum of the 0.1M $CuSO_4$ solution compared to the background. It can be seen in these middle and low concentration spectra that the first excited state of ^{63}Cu at 0.965 MeV has a very high yield at 1M, and which is still prominent at 0.2M, but which is indistinguishable from the

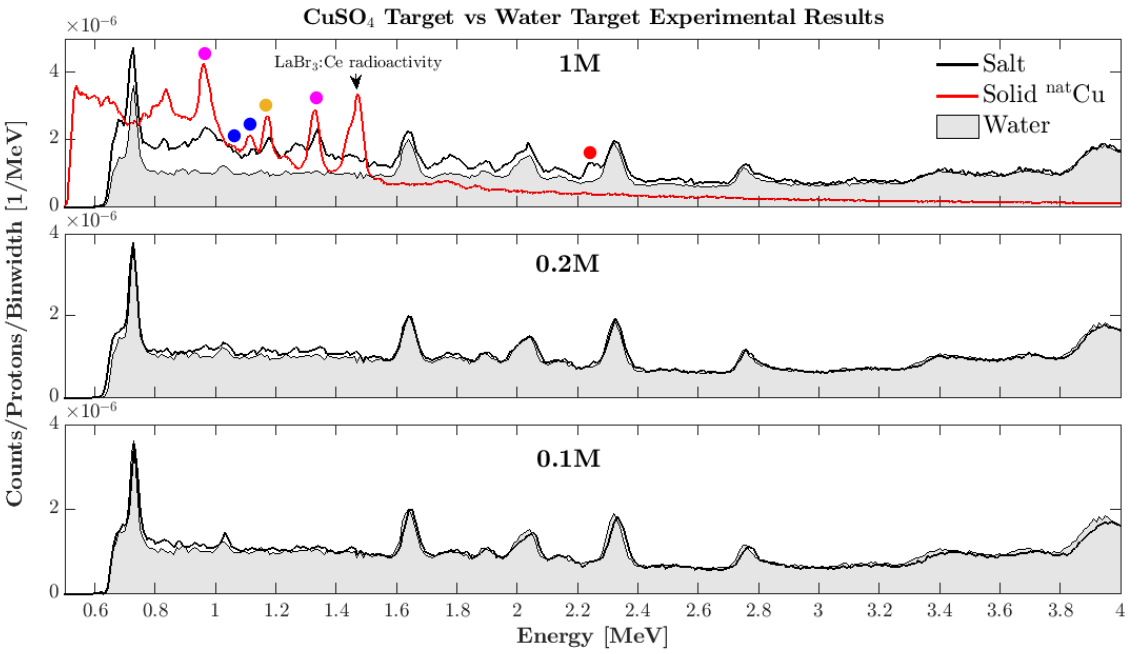

Figure 3.10: Experimental spectra of solid ^{nat}Cu, high, medium and low concentration results for the $CuSO_4$ liquid target plotted with the water spectrum in PMMA flasks. The liquid target experimental results have been background subtracted. The labelled peaks correspond to the following fragments: • ^{63}Cu*, • ^{65}Cu*, • ^{62}Ni*, and • ^{32}S*.

water background at 0.1M. Further, the 0.2M solution shows a good FWHM for the first excited state of ^{65}Cu at 1.025 MeV. For the 0.1M solution, it can be seen that there is an overall reduction of the signal due to the prompt γ-ray signature in the low energy region between 0.8 and 1.4 MeV when one compares the response of the 1M, 0.2M and 0.1M spectra. The peaks which exhibit the highest prompt γ-ray response at low concentration are the peak due to ^{65}Cu* (1.025 MeV) and ^{63}Cu* (1.34 MeV). These peaks retain a high yield and shape in regions which contain low water background signal. The peak which shows the most potential for use as a prompt γ-ray enhancement is the ^{65}Cu emission, however, this peak is situated in a region where the background too exhibits a prompt γ-ray response and would therefore be difficult to distinguish in a treatment plan. It is observed that had there been signature copper peaks present between 1.3 and 1.5 MeV in the experimental spectra of the solutions, that this signature would have been lost to the detector internal radioactivity (seen as the labelled $LaBr_3$:Ce peak) (see Subsection 2.2.3 for a description on the methodology). This peak is present in the spectrum of the solid target and not that of the liquid target because the cyclotron RF signal was not used to subtract background noise from the solid targets.

The top panel of 3.11 shows the simulation results of the highest natural concentration

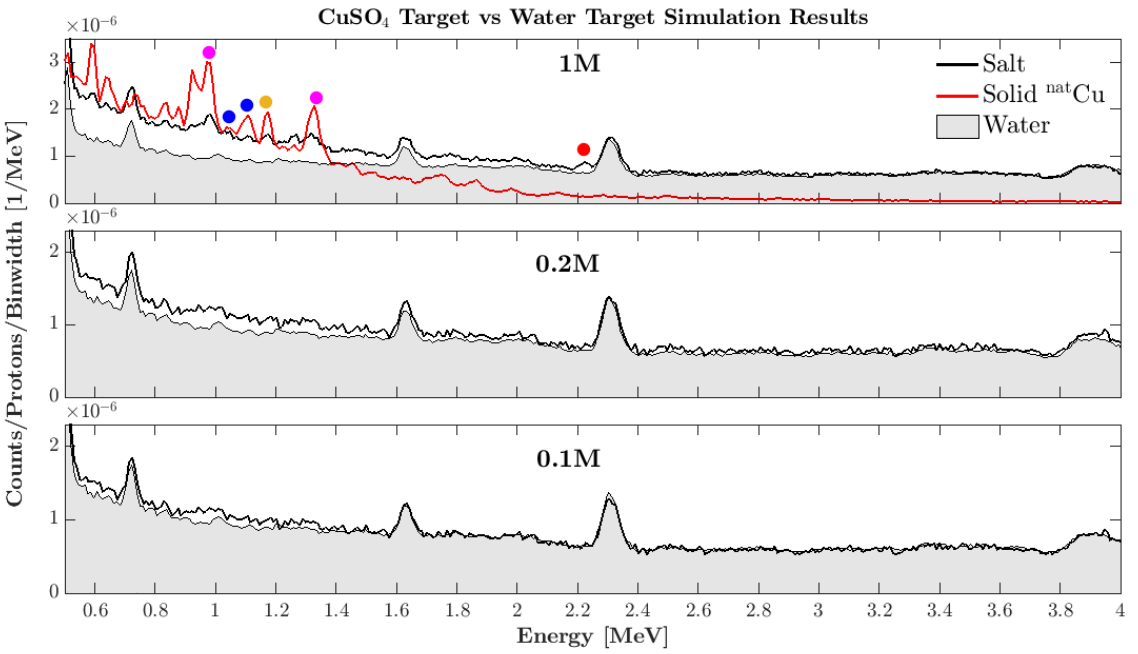

Figure 3.11: Simulation spectra of solid ^{nat}Cu, high, medium and low concentration results for the $CuSO_4$ liquid target plotted with the water spectrum. The labelled peaks correspond to the following fragments: • ^{63}Cu*, • ^{65}Cu*, • ^{62}Ni*, and • ^{32}S*.

solid ^{nat}Cu target spectrum with that of the 1M liquid target and the water background spectrum. It is seen that the lower concentration of copper present in the solution causes a reduction in the signal-to-noise ratio of the peaks. However, the simulation predicts the emission fragments accurately when compared to the experimental results. The 1M solution shows a good enhancement in prompt γ-ray response with a signal which is easily discernible from the background spectrum. One observes in the bottom panel of Fig 3.11 that at 0.1M, where the mass fractions of both copper and sulphur have been reduced by $\approx$ 10% when the concentration was reduced from 1M to 0.1M, that the signature prompt γ-ray yield, labelled in the plot, has reduced considerably with the reduction in concentration. The 0.2M solution shows an enhancement of tracer prompt γ-ray signature, but where the simulation does not account for the shape of the peaks adequately and the signature is seen more as a noisy continuum than defined peaks. The identified signature peaks are of overall lower intensity in the simulation data, however, the ^{63}Cu* is visible at 0.965 MeV and contributes to the majority of the enhancement in this region. The simulation also accurately accounts for the ^{63}Cu* signature at 1.34 MeV and the ^{65}Cu* at 1.125 MeV which are seen as two closely spaced peaks at even the lowest concentration. Due to the potential inadequacies of the TOPAS physics lists in predicting the cross section of the fragments, the simulation shows a continuum of signal rather than a strong prompt γ-ray response, with the aforementioned ^{65}Cu* at 1.025 MeV peak exhibiting the only

distinguishable signature.

3.3.2 $Y(NO_3)_3$+$6H_2O$ Liquid Target

The $Y(NO_3)_3$+$6H_2O$ salt was dissolved at molar concentrations of 1M, 0.17M and 0.1M in 100ml of H_2O, where the corresponding mass fractions are shown in Fig 3.12. The investigated tracer, ^{89}Y or ^{nat}Y, is the only stable isotope of yttrium. The aim was to characterise the prompt γ-ray response of the salt at a high concentration ($\approx$ 5% ^{89}Y present in the solution), after which the concentration was lowered and the feasibility of using the tracer was quantified by its enhancement capabilities.

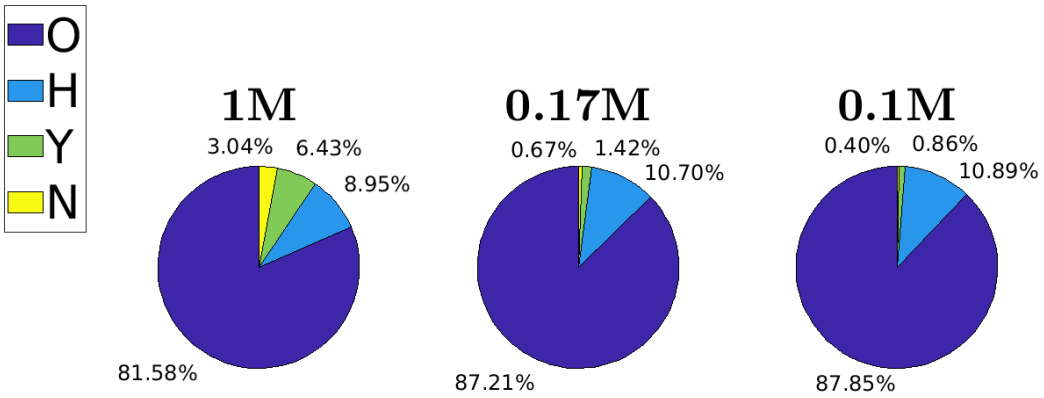

Figure 3.12: Mass fractions for the three investigated molar masses of $Y(NO_3)_3$+$6H_2O$ in 100 ml of pure water.

Figure 3.13 shows the experimental and simulation results of all three concentrations of $Y(NO_3)_3$, the water plus the element being studied in salt form. It can be seen in Fig 3.13 that the ^{89}Y isotope produces many residuals via discrete γ decay, residuals which exhibit a high cross section in the low energy region ($<$ 2 MeV) where there is a low background signal originating from the oxygen isotopes present in both the salt and water. These prompt γ-ray peaks were brought about by the inelastic scattering of protons. The peaks which exhibit the highest prompt γ-ray response are labelled by colour, where the associated excitation levels observed in the bombardment of this liquid target with a 70 MeV beam are: $^{89}Y(p,t)^{87}Y^*$ at 0.797 MeV, $^{89}Y(p,2p)^{88}Sr^*$ at 0.866 MeV, $^{89}Y(p,n\gamma)^{89}Zr^*$ at 0.947 MeV, $^{89}Y(p,2n\gamma)^{88}Zr^*$ at 1.075 MeV, and $^{89}Y(p,p'\gamma)^{89}Y^*$ at 1.275 MeV. These de-excitation levels were cross-checked against the NuDat database (7) and TALYS simulation results (seen in Subsection 3.2.1). The number of incident protons in simulation and experiment are found in Table 3.4.

Figure 3.13 provides insight into the performance and accuracy of the TOPAS simulation

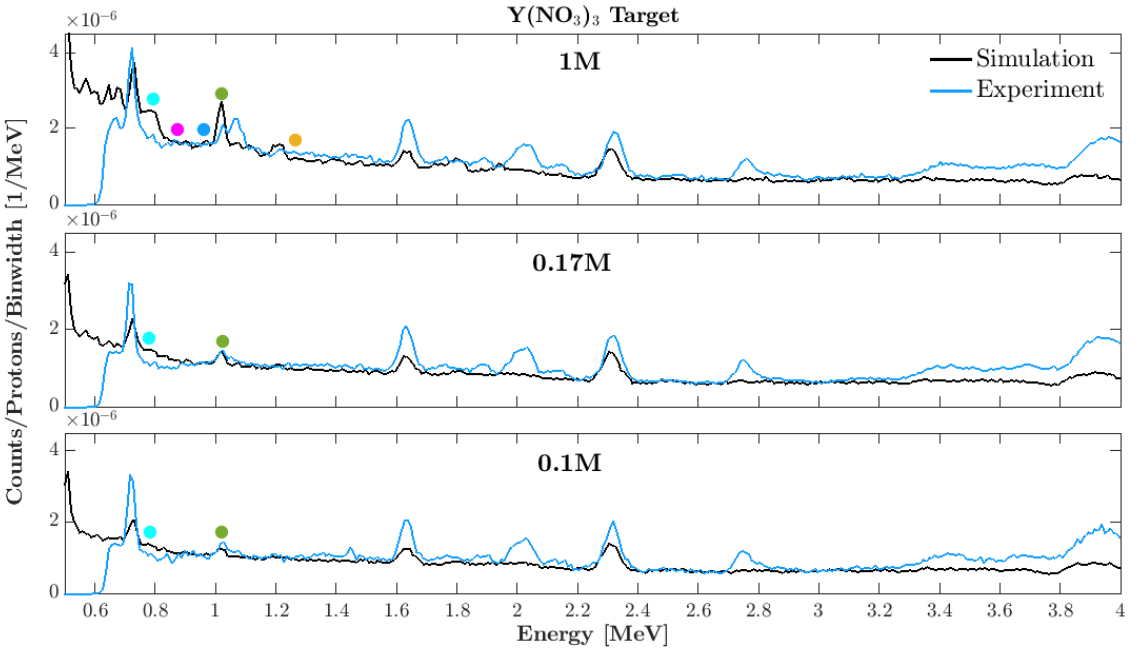

Figure 3.13: Simulations vs background subtracted experimental results for the $Y(NO_3)_3$ liquid target at high, medium and low concentration. The labelled peaks correspond to the following fragments: • $^{87}Y^*$, • $^{88}Sr^*$, • $^{88}Zr^*$, • $^{89}Y^*$, and • $^{89}Zr^*$.

	Concentration		
	1M	**0.17M**	**0.1M**
Simulation	4×10^9	4×10^9	4×10^9
Experiment	1.45×10^{10}	2.12×10^{10}	7.28×10^9

Table 3.4: Number of incident protons as used in simulation and experiment for the $Y(NO_3)_3$ targets.

physics lists in predicting the prompt γ-ray spectrum obtained in experimentation. One can easily observe how quickly the labelled prompt γ-ray signature is reduced in cross section as the concentration of the solution is reduced. Here, the 1M solution carries 6.43% ^{89}Y, where the 0.17M contains 1.42% and the 0.1M only 0.86%. The top panel of Fig 3.13 shows the prompt γ-ray results obtained in simulation and experiment for the high concentration $Y(NO_3)_3$ target. This solution shows a large discrepancy between the peaks predicted by simulation and those obtained in experimentation. The peak corresponding to the fragment ^{87}Y at 0.797 MeV is predicted with a higher cross section by simulation than what is seen in experiment. The experimental results show a high cross section for the ^{88}Y peak at 1.22 MeV. The $^{88}Zr^*$ peak at 1.075 MeV is predicted by TOPAS with a cross section which is double of that obtained in experimentation. The peak alongside

the zirconium emission in the experimental data originates from the 1.07 MeV PMMA ^{12}C(p,x)^{10}B*, ^{12}C(p,x)^{10}C $\rightarrow$ ^{10}B*, ^{16}O(p,x)^{10}B* state. This PMMA emission is not present in the simulation results as the prompt γ-rays were scored in the liquid target without including the flasks in simulation (see Section 3.3 for a detailed description of the methodology) (46). Further, the ^{89}Y* excited state, that exhibited a high cross section in the simulation results for the solid yttrium target, is absent in both simulation and experimental results at 1M and has thus been lost in the decrease of concentration. This state remains labelled in the plot for reference.

The middle panel of Fig 3.13 shows the middle or medium $Y(NO_3)_3$ target solution. This is a $\approx$ 10% decrease in tracer concentration from 1M to 0.17M. At middle concentration the prompt γ-ray spectrum has decreased considerably. The ^{88}Zr* peak at 1.075 MeV shows a similar cross section in the spectrum of both simulation and experiment, retaining its FWHM and with a distinguishable cross section appearing over the background spectrum. This peak remains a prompt γ-ray signature at 0.1M, just 0.86% of ^{89}Y present in the solution, seen in the bottom panel of Fig 3.13. The reduction in concentration of the solution results in an overall improvement of the agreement between the simulation and experimental results. This prompt γ-ray ^{88}Zr* signature is obscured by PMMA signal in the experimental results, where the simulation suggests that without the PMMA signal this peak might be more defined.

Figures 3.14 and 3.15 show the prompt γ-ray spectra of the solid ^{89}Y rod target plotted with the results of the 1M solution of $Y(NO_3)_3$ (with the PMMA flask for experiment) and the water background (with the PMMA flask for experiment). The $LaBr_3$:Ce detector background is present in the red solid target spectrum and has been subtracted from the liquid target spectra, as described in Subsection 2.2.3, which contributes a background continuum and the $\approx$1.4 MeV labelled peak. The water background is pictured as a grey shaded region to better differentiate the prompt γ-ray response of the ^{89}Y tracer element from that of water. The middle and bottom panels of each of these Figs. 3.14 and 3.15 show the prompt γ-ray spectra of the middle and low concentration solutions of $Y(NO_3)_3$ (with the PMMA flask for experiment) and the water background (with the PMMA flask for experiment).

In the first panel of the experimental results plotted in Fig 3.14, the identified ^{89}Y peaks at highest natural concentration have reduced in FWHM when compared to those of 1M concentration $Y(NO_3)_3$ solution. The reduction in cross section from solid to liquid target causes the ^{88}Sr* and ^{89}Zr* peaks to be lost in the background spectrum, even at the high 1M liquid concentration. The ^{87}Y* peak is barely visible at 1M and is nearly absorbed into the ^{12}C(p,x)^{10}B*, ^{16}O(p,x)^{10}B*, ^{12}C(p,x)^{10}C $\rightarrow$ ^{10}B* peak at 718 keV produced in the water and PMMA materials. The 1M solution is a very high concentration of the yttrium tracer element, an unrealistic scenario in PT, however it is interesting to measure the prompt γ-ray response at high concentrations before reducing the concentration to gauge the prompt γ-ray response at lower concentrations of the isotope. In the high energy range ($>$ 3.5 MeV) of Fig 3.14 the presence of the prompt γ-ray signature is low as the water

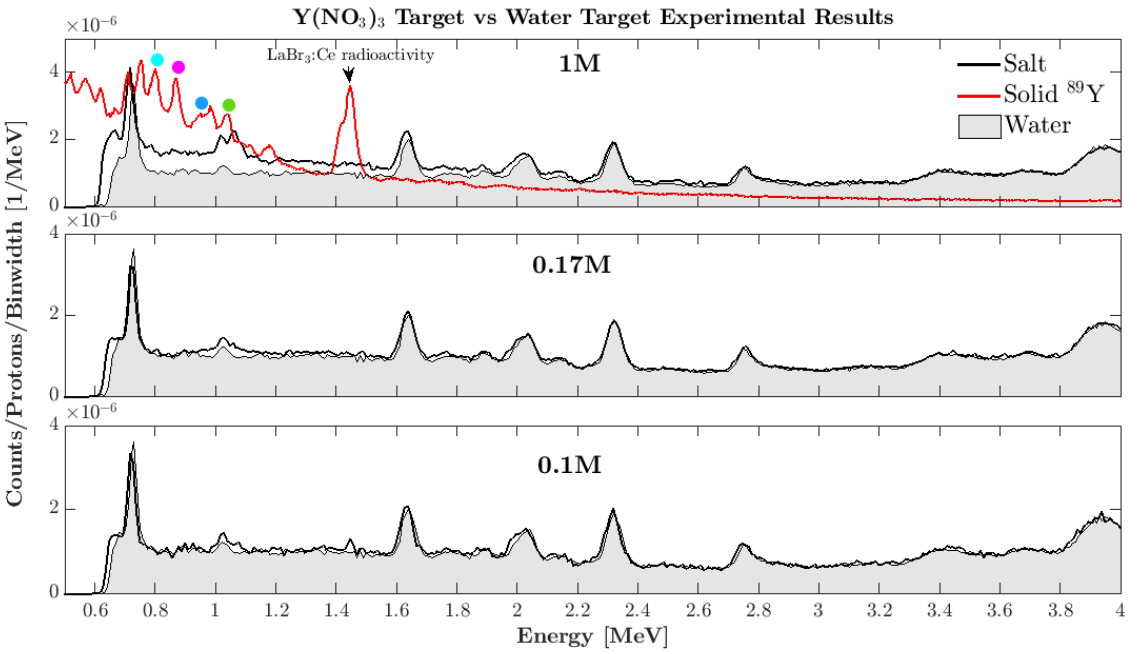

Figure 3.14: Experimental spectra of solid ^{89}Y, high, medium and low concentration results for the $Y(NO_3)_3$ liquid target plotted with the water spectrum in PMMA flasks. The liquid target experimental results have been background subtracted. The labelled peaks correspond to the following fragments: • ^{87}Y*, • ^{88}Sr*, • ^{88}Zr*, • ^{89}Y*, and • ^{89}Zr*.

dominates the spectrum and, thus, prompt γ-ray enhancement is not easily observed. The region of the $Y(NO_3)_3$ solution spectrum at high concentration where the prompt γ-ray response is most distinguishable from the background spectrum is seen as the white space region between the salt solution and the water background spectra. This enhancement is greatest between $\approx$ 0.79 and 1.3 MeV. The 1M solution was expected to retain the high cross section of peaks as predicted with the solid target, however the prompt γ-ray yield reduced substantially. The peak due to ^{88}Zr* is the only distinguishable peak at high concentration seen in the experimental results, where the PMMA and water background spectrum contribute to the FWHM, as a double peak, with the aforementioned peak at 1.07 MeV.

The middle plot of Fig 3.14 shows the 0.17M $Y(NO_3)_3$ solution, and the bottom plot shows the 0.1M concentration. There is a large decrease in the enhancement due to the prompt γ-ray signature when compared to water, where the range of the enhancement contribution is reduced to the region $\approx$ 0.95 to 1.15 MeV. The ^{88}Zr* emission peak is the only definitive evidence that the proton beam has interacted with the tracer element within the target tumor region. This peak shows a good prompt γ-ray signature at the lowest concentration of 0.1M, however, the cross section of this peak does not originate

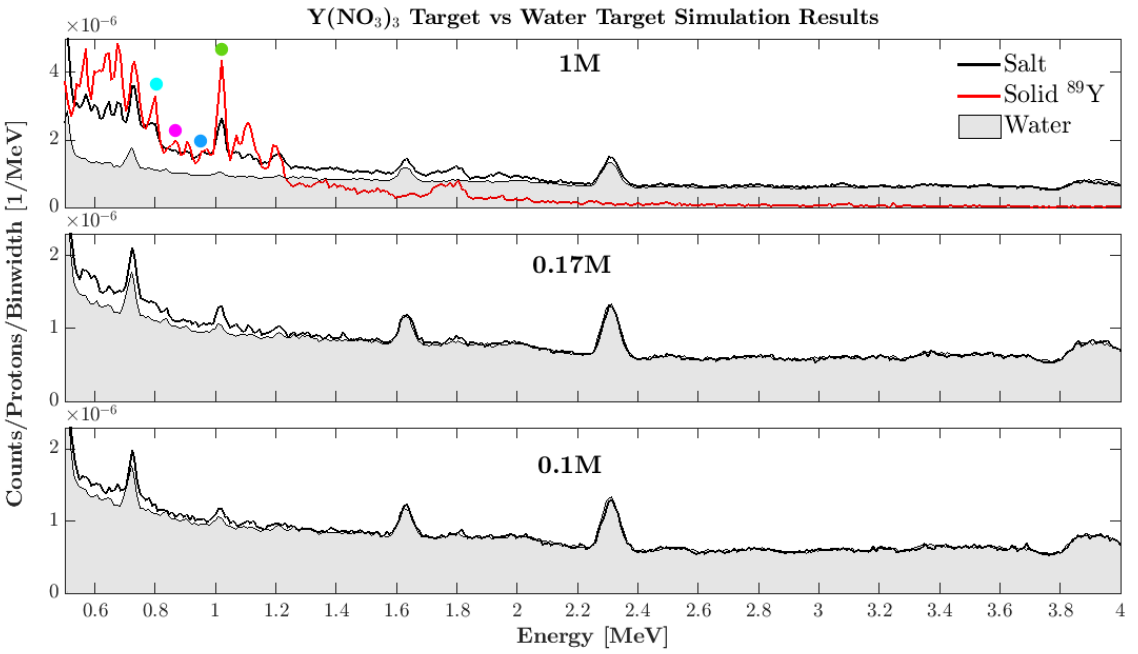

Figure 3.15: Simulation spectra of solid ^{89}Y, high, medium and low concentration results for the $Y(NO_3)_3$ liquid target plotted with the water spectrum. The labelled peaks correspond to the following fragments: • ^{87}Y*, • ^{88}Sr*, • ^{88}Zr*, • ^{89}Y*, and • ^{89}Zr*.

soley from the yttrium element but is comprised of the PMMA and water emission at that energy too. This is unfortunate as the ^{88}Zr* peak appears to be the only prompt γ-ray signature of the ^{89}Y target tracer element and it would be indistinguishable from the background spectrum due to human tissue in a PT treatment. It is therefore noted that when the mass fraction of yttrium in the target volume is 0.86%, the only signature peak which was visible has disappeared and the spectrum is only distinguishable from that of water by a continuous enhancement, as was the case with the liquid copper target at low concentration. Without a visible peak, there is no signature evidence of the element of interest in the water. In this instance at 0.1M the continuum is due to the presence of the element, but in a realistic scenario it can be caused by the presence of organic human tissue, bone, or the anatomical fluctuations between patients. Thus, only the presence of an enhancement is not proof of the presence of the element but it is desirable to see a peak which is emitted by the element. It is interesting to take into account that at the lowest concentration in the yttrium solution, the solution contains $\approx 0.2\%$ more of the element of interest than the copper and phosphorus solutions. Although ^{89}Y produces many prompt γ-rays and in the low energy region of interest, there is very little spreading between the peaks. This increases the susceptibility of the γ emission peaks being lost to a more continuous energy distribution.

Figure 3.15 shows the targets plotted in panels in the same manner as those investigated in Fig 3.14 but the results pertain only to simulation. Here the red spectrum once again represents the solid ^{89}Y target rod. When comparing the overall behaviour of the simulation results to the experimental results, one observes the greater sharpness in the peaks obtained with TOPAS simulation. There are two explanations for this behaviour. Firstly, the solid target spectrum obtained in experiment is contaminated with the $LaBr_3$:Ce detector internal radioactivity spectrum and the simulation results do not have this contaminant. This addition of $LaBr_3$:Ce internal radioactivity causes an overall increase in the background of the low energy experimental results of the solid target spectrum. Secondly, when comparing the solution results of simulation and experiment, the simulation did not score for the prompt γ-ray interactions of the proton beam with the PMMA flask which housed the liquid targets. For this reason, and particularly for the $Y(NO_3)_3$ target solution where the peaks are situated near to one another, there appears to be a greater energy spread between consecutive peaks in the simulation when compared to the background. The background spectra include the PMMA contribution and for this reason the energy spreading is more of a continuous spectrum due to the background. This is interesting as the simulation results gain insight into the FWHM of the predicted prompt γ-ray signature peaks, which are then compared to experiment for accuracy. This comparison with experiment allows one to gauge the extent of the background contribution which would inevitably be encountered in a treatment plan.

The simulation results for the high concentration targets in the top panel of Fig 3.15 show a greater agreement in the peaks in the spectrum of the target and those of the liquid 1M target solution. The cross section of these peaks has reduced, where the ^{88}Sr* and ^{89}Zr* peaks which were small in the spectrum of the solid target have reduced in the liquid target as they did in the experimental results. The ^{87}Y* peak is more distinguishable in the simulation than in the experiment as the PMMA contribution of the 718 keV peak is not included, reducing the cross section of the background to only the water contribution. The overall behaviour of the reduction of the prompt γ-ray spectrum as the concentration is reduced is in agreement with the experimental results, as one sees in the second and third panels of Fig 3.15 of the 0.17M and 0.1M solutions. The same behavior is exhibited where the ^{88}Zr* peak is distinguishable at all concentrations. The range of the prompt γ-ray tracer enhancement contribution is greater than the narrow white space region seen in experiment as the PMMA contribution is not included. The grey water contribution at the same energy as the ^{88}Zr* emission peak is well produced in simulation and mimics the experimental results.

3.3.3 NaH_2PO_4+H_2O Liquid Target

The NaH_2PO_4+H_2O salt was dissolved at molar concentrations of 2M, 0.5M and 0.2M in 100ml of H_2O, where the corresponding mass fractions are shown in Fig 3.16. The aim was to characterise the prompt γ-ray response of the salt at a high concentration ($\approx$ 5% ^{31}P), after which the concentration was lowered and the feasibility of using the tracer was quantified by its enhancement capabilities.

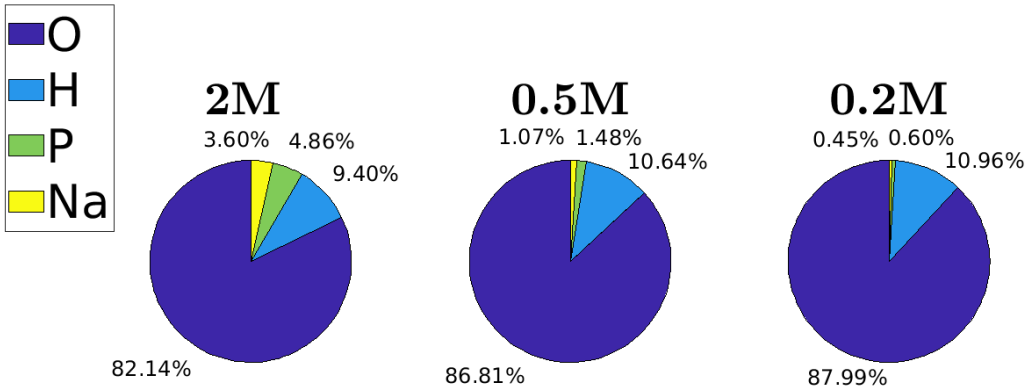

Figure 3.16: Mass fractions for the three investigated molar masses of NaH_2PO4+H_2O in 100 ml of pure water.

Figure 3.17 shows the experimental and simulation results of all three concentrations of NaH_2PO4, the water plus the element being studied in salt form. It can be seen in Fig 3.17 that the ^{31}P isotope produces many residuals via discrete γ decay, residuals which exhibit a high cross section in the low energy region ($<$ 2 MeV) where there is a low background signal originating from the oxygen isotopes present in both the salt and water. These prompt γ-ray peaks were brought about by the inelastic scattering of protons incident on the target ^{31}P, as well as that of the ^{23}Na introduced in the salt, a peak which would have proven a valuable characteristic of the salt had it not been situated within the region of many characteristic water peaks. The peaks which exhibit the highest prompt γ-ray response are labelled by colour, where the associated excitation levels observed in the bombardment of this liquid target with a 70 MeV beam are: ^{31}P(p,p'γ)^{31}P* at 1.133, 1.27 and 1.373 MeV, ^{31}P(p,α)^{28}Si* at 1.7856 (51), ^{31}P(p,nγ)^{30}P* peaks correspond to energies of 1.45 and 2.03 MeV, ^{31}P(p,pγ)^{30}Si* at 1.54 MeV, and ^{23}Na(p,p'γ)^{23}Na* at 2.235 MeV. These de-excitation levels were cross-checked against the NuDat database (7) and TALYS simulation results (seen in the solid target results in Subsection 3.2.3). The number of incident protons in simulation and experiment can be seen in Table 3.5.

	Concentration		
	2M	**0.5M**	**0.2M**
Simulation	10×10^{11}	1×10^{11}	1×10^{9}
Experiment	1.51×10^{10}	2.35×10^{10}	2.7×10^{10}

Table 3.5: Number of incident protons as used in simulation and experiment for the NaH_2PO_4 targets.

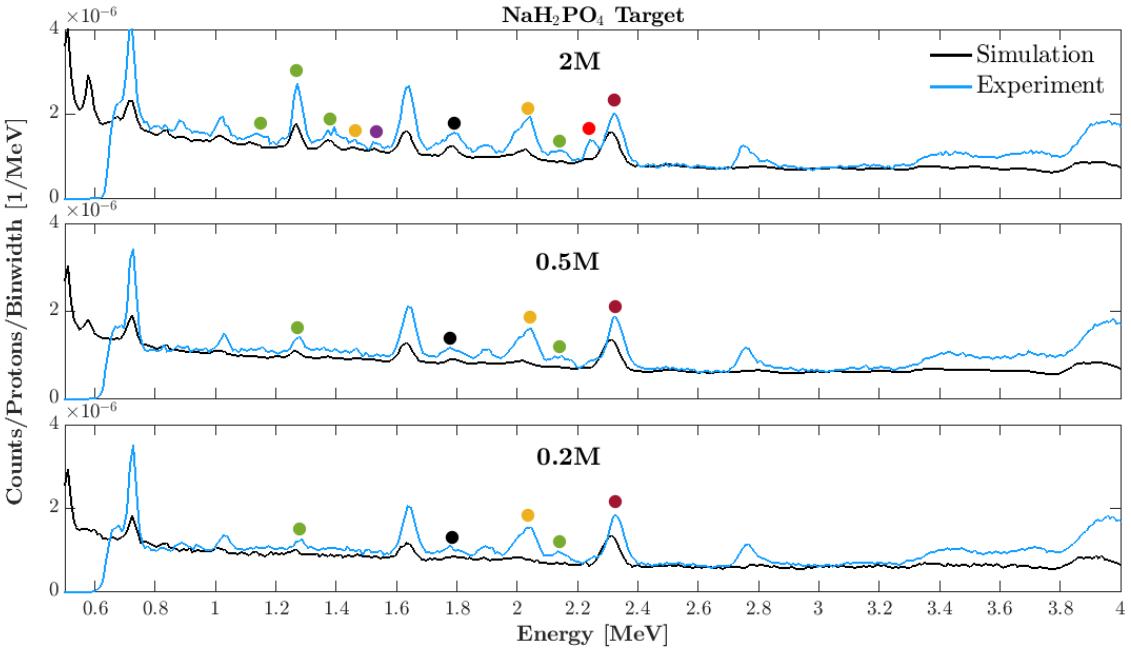

Figure 3.17: Simulations vs background subtracted experimental results for the NaH_2PO_4 liquid target at high, medium and low concentration. The labelled peaks correspond to the following fragments: ● $^{31}P^*$, ● $^{30}P^*$, ● $^{30}Si^*$, ● $^{32}S^*$, ● $^{23}Na^*$, and ● $^{28}Si^*$.

Figure 3.17 shows the results of the simulation and experiment plotted on the same axes to gain insight into the performance of the TOPAS physics lists for this tracer. The overall observed trend of the simulation spectrum is much alike that obtained in experiment. The TOPAS physics lists appear to have a good grasp of the nuclear structure. The region > 2.5 MeV sees the background emissions dominating the spectrum, where the simulation shows discrepancy in the predicted background peaks. This is exemplified at 2.79 MeV where a ^{14}N emission peak produced in experiment due to the oxygen isotope in water is not predicted in the simulation results. This is a common feature seen in the interaction of a proton beam with water and was discussed in detail in the background Subsection 3.1. The top bar of Fig 3.17 shows that the majority of the identified ^{31}P

prompt γ-ray emissions are well accounted for in simulation. The excited state of ^{31}P are in good agreement when comparing simulation to experiment, however, the cross section in simulation is lower than that obtained experimentally. The prompt γ-ray signatures which are most distinguishable in simulation are ^{31}P* at 1.27 and 1.373 MeV, and ^{28}Si* at 1.7856 MeV. The simulation did not predict the ^{23}Na* emission at 2.235 MeV with the high cross section seen in experiment. The ^{30}P* excited state at 2.03 MeV is seen as a sharp peak in experiment, with a much lower concentration in simulation. This is due to the PMMA contribution at 2 MeV which is not accounted for in simulation. For this reason, the simulation is a more reliable depiction of the ^{31}P prompt γ-ray signature in this region as it is not contaminated by the strong PMMA background. The ^{32}S* emission is seen as a peak with a good FWHM in both simulation and experiment. Although there is a contribution from this decay fragment at this energy, and which was identified as a good emission in the solid target Section 3.2.3, with the introduction of the water background this peak is now combined with the emission of ^{16}O(p,x)^{14}N* at 2.313 MeV. The middle panel of Fig 3.17 shows the 0.5M concentration where ^{31}P has a molar mass concentration of 1.48%. Here the cross section of the 1.27 MeV phosphorus excited state shows a promising signature, and which is still visible in the bottom panel at 0.2M. The identified prompt γ-ray peaks above 1.4 MeV are all contaminated by water and PMMA background. Below 1.4 MeV, the medium and low concentration solutions show two sharp peaks in the experimental spectrum. One of these peaks is the ^{31}P* labelled emission, and the other is attributed to the the 1.07 MeV PMMA ^{12}C(p,x)^{10}B*, ^{12}C(p,x)^{10}C $\rightarrow$ ^{10}B*, ^{16}O(p,x)^{10}B* state and does not appear in simulation as a result. For this reason only the 1.27 MeV peak remains a prompt γ-ray signature in the NaH_2PO_4 solution. The TOPAS physics lists predict this peak of interest accurately.

Figures 3.18 and 3.19 show the prompt γ-ray spectra of the 2M solution of NaH_2PO_4 (with the PMMA flask for experiment) and the water background (with the PMMA flask for experiment). The simulation results of the solution are plotted with the solid ^{31}P box spectrum which was not measured experimentally due to the high chemical reactivity and toxicity of this elemental material in solid form. The water background is pictured as a grey shaded region to better differentiate the prompt γ-ray response of the ^{31}P tracer element from that of water. The middle and bottom panels of each of these Figs. 3.18 and 3.19 show the prompt γ-ray spectra of the middle and low concentration solutions of NaH_2PO_4 (with the PMMA flask for experiment) and the water background (with the PMMA flask for experiment).

The experimental results in the top panel of Fig 3.18 show many prompt γ-ray signature peaks which have a high cross section that contributes to an enhancement in the low energy region. This enhancement is seen as the white space between the spectrum of the salt and that of the grey shaded water. The 1M solution, composed of 4.86% ^{31}P, presents many well defined peaks. The peaks of great interest are those situated in regions at which the PMMA and water background do not contribute distinct peaks of their own. This is characteristic of the 1.27 MeV ^{31}P excited state, where the grey background spectrum is flat at this energy where the element tracer shows a good

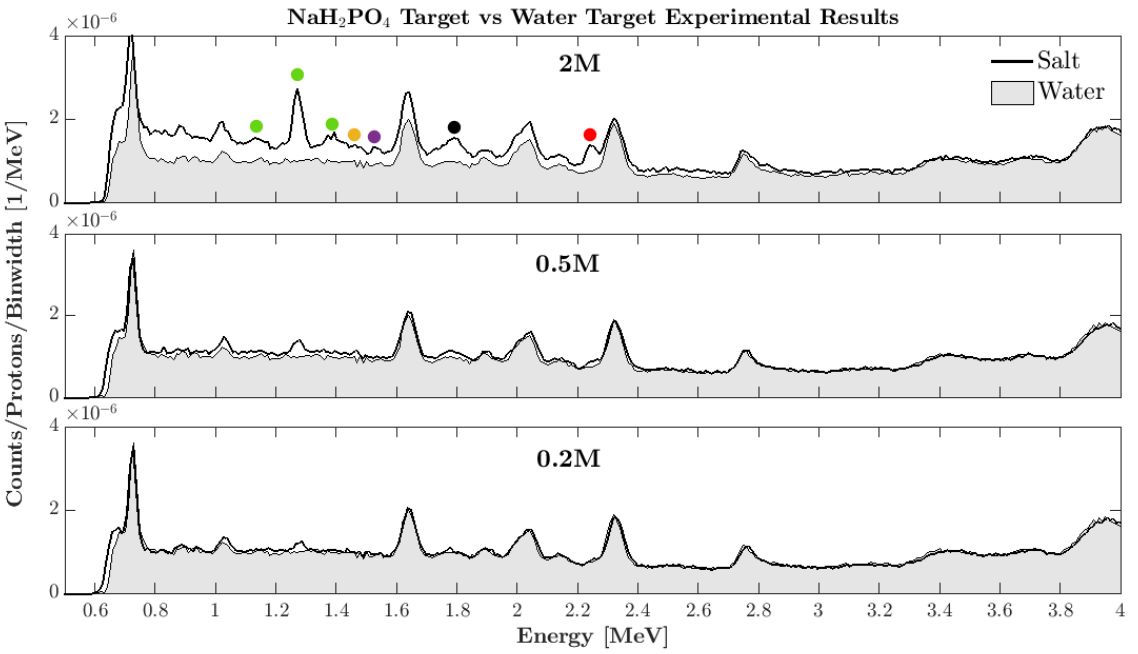

Figure 3.18: Background subtracted experimental spectra of the high, medium and low concentration results for the NaH_2PO_4 liquid target plotted with the water spectrum in PMMA flasks. The labelled peaks correspond to the following fragments: ● $^{31}P^*$, ● $^{30}P^*$, ● $^{30}Si^*$, ● $^{32}S^*$, ● $^{23}Na^*$, and ● $^{28}Si^*$.

signature. One can easily observe how quickly the signal reduces as the concentration is lowered. Paying attention to the 1.1 to 2.3 MeV region of Fig 3.18, the excited state of ^{31}P at 1.133 MeV, which was easily distinguishable with a high yield at 2M, is reduced at 0.5M and completely indiscernible at 0.2M. This is true for the majority of the other identified emission peaks too. The 1.27 MeV phosphorus emission is the only peak which contributes substantially to a prompt γ-ray signature enhancement at 0.1M, where ^{31}P comprises 0.6% of the solution. This behaviour was also seen in the yttrium and copper targets, where they too presented only one strong prompt γ-ray signal at the lowest concentration. For these other solutions, the peak was situated in an energy range where the water and PMMA background contributed background peaks which obscured the signature. It is interesting to note that in the energy range of 0.8 to 1.4 MeV, if the post-processing background analysis had not been done, the 1.27 MeV ^{31}P peak of interest would have been washed out by the $LaBr_3$:Ce internal radioactivity. Thus, if not for this post-processing (see Subsection 2.2.3 for the associated methodology), this significant enhancement would not have been made visible due to the very low signal-to-background ratio. This mass fraction of 0.6% of ^{31}P at 0.1M is still too high for a therapeutic PT application, but it is a good indication of the potential of this phosphorus solution in prompt γ-ray range verification.

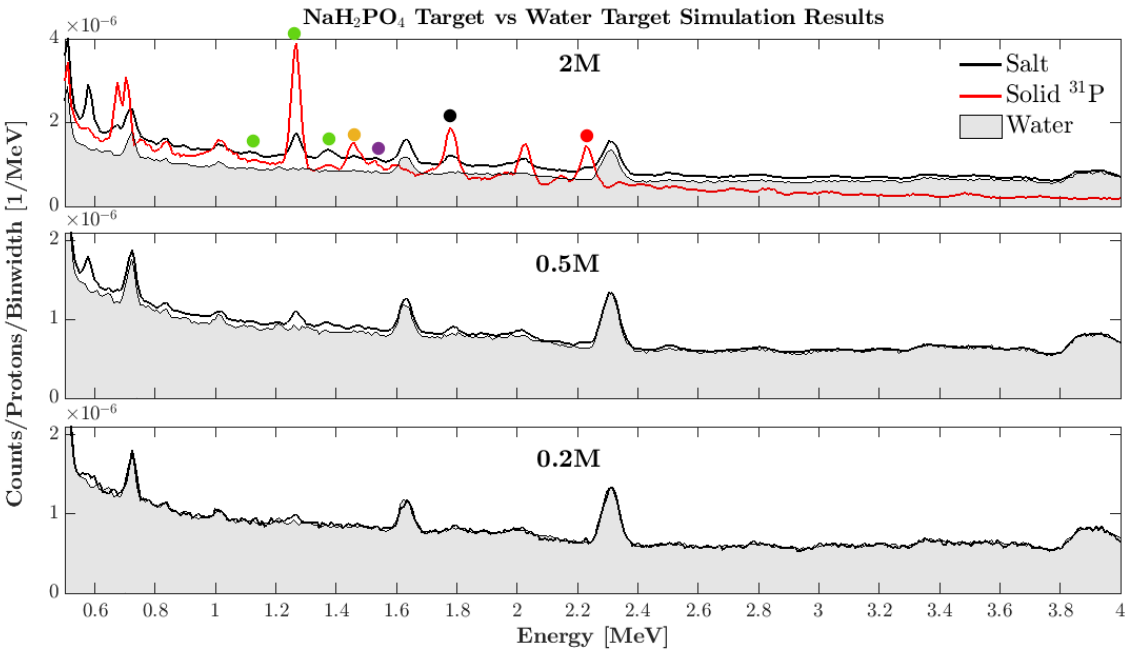

Figure 3.19: Simulation spectra of solid ^{31}P, high, medium and low concentration results for the NaH_2PO_4 liquid target plotted with the water spectrum. The top panel shows the results of the solid ^{31}P target. The labelled peaks correspond to the following fragments: ● ^{31}P*, ● ^{30}P*, ● ^{30}Si*, ● ^{32}S*, ● ^{23}Na*, and ● ^{28}Si*.

Figure 3.19 shows the prompt γ-ray spectra of the solid phosphorus rod target plotted with the results of the 2M solution of NaH_2PO_4 and the water background in the PMMA flask for the first panel, and the medium and low concentrations of the solution plotted with the water and PMMA background in the middle and bottom panels respectively. The labelled peaks correspond to prompt γ-ray signatures which are present in both the solid target with the highest natural abundance of ^{31}P and the 2M solution with a ^{31}P mass fraction percentage of 4.86%. These peaks are not present in the water prompt γ-ray spectrum and are thus discernible from background. This demonstrates that the phosphorus signature has not been lost in the change from solid to liquid target. In fact, the peaks identified in the solid target spectrum are all apparent in the solution, which was not the case for the yttrium solution. Here, as one casts their eye down the panels, it can be seen that as the concentration is reduced, the same behaviour is exhibited in the simulation as was seen in the experimental results. The simulation exhibits a good cross section when compared to the experiment suggesting that the TOPAS MC model has a good grasp of the nuclear structure of the ^{31}P isotope. This is not true for the ^{23}Na isotope as the first excited state at 2.235 MeV is not accounted for by simulation. The ^{31}P at 1.27 MeV shows a very promising signature emission at 2M which has a good FWHM and spread when compared to the other emission peaks. Overall, the simulation shows good

results at high concentration, for which a signature was preserved as the concentration was lowered. Phosphorus de-excitation levels are thoroughly recorded for energy levels > 2 MeV and the model shows surprisingly good results for very low energies.

3.3.4 Enhancement of Prompt γ-Ray Response in Liquid Targets

Enhancement calculations were performed for the high, medium and low concentrations of the liquid targets. This was done by performing an integral ratio of the counts per incident number of protons per bin over an energy deposition range of 0.8 to 1.4 MeV of the solution energy spectrum divided by water spectrum in that same range, as seen in Eq 3.1.

$$Enhancement\ \% = \frac{\int_{0.8MeV}^{1.4MeV} Salt\ dE}{\int_{0.8MeV}^{1.4MeV} Background\ dE} \times 100 - 100 \tag{3.1}$$

This low energy range was chosen in Subsection 3.2.4 as the most suitable by taking into account the regions for each chosen isotope which exhibit the strongest signature prompt γ-ray spectrum, and which is the least affected by the water and PMMA flask background. A second integral was performed in the same manner as Eq 3.1 but the range was changed to $3.4 - 4$ MeV to gain quantitative understanding into the statistical fluctuation of the water + PMMA result, where the region was chosen for exhibiting signal which originated solely from water (and PMMA in experimental results). This second integral provides insight into the fluctuation present in the low energy region integral due to the water. Figures 3.20 and 3.21 show the results of these integral ratio enhancement percentages, where the prompt γ-ray enhancement between 0.8 to 1.4 MeV is labelled by solution in colour seen in the legend, and the statistical fluctuation in the 3.4 to 4 MeV region is seen as blue. The high concentration is seen in the top row for each of the three solutions, plotted from 0 to 100% on the y-axis. The middle and bottom rows represent the middle and low concentrations respectively, and it should be noted that the y-axis range extends from 0 to 30%. These enhancement calculations are plotted for simulation and experiment and for each concentration of solution as the energy spectrum vs normalised counts in Appendix Section .2. These spectra have all been discussed previously, however, the additional plots have been provided for further reference. One observes that the statistical fluctuation in the experimental results is greater than that encountered in the simulation results. This is to be expected for calibration and environment factors will introduce their own associated errors.

Figure 3.20 shows that the highest prompt γ-ray response is attributed to $CuSO_4$, with an enhancement percentage of 74.64% at highest concentration, and with a very low statistical background fluctuation of 0.64%. The highest signal contribution corresponded to the ^{63}Cu(p,p'γ)^{63}Cu* at 0.965 MeV and ^{65}Cu(p,p'γ)^{65}Cu* at 1.025 MeV peaks which merged to form the much larger peak visible in the spectrum. The natural abundance of ^{65}Cu creates further enhancement at 1.325 MeV, which was seen in Subsection 3.3.1 as the second sharp peak of high yield. The final contribution to the enhancement in this

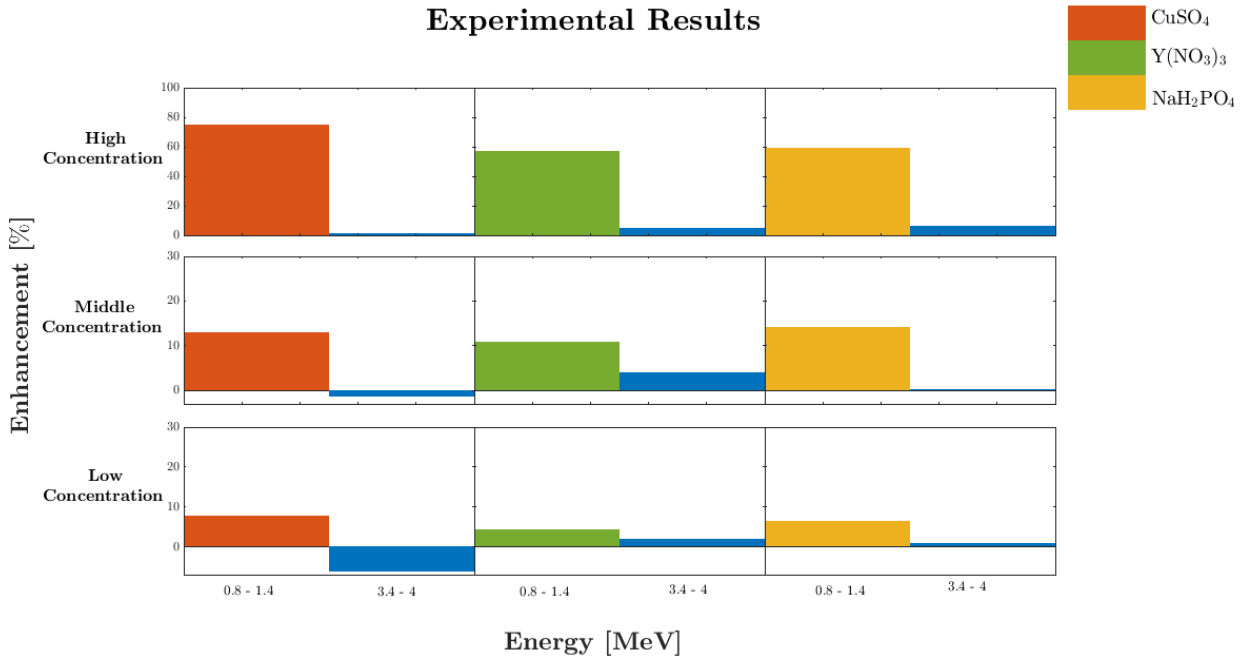

Figure 3.20: Experimental estimates of prompt γ-ray enhancement percentages and statistical fluctuation in the three salt targets.

range was due to ^{63}Cu(p,p'γ)^{63}Cu* at 1.325 MeV and ^{65}Cu(p,α)^{62}Ni* at 1.17 MeV. At high concentration the NaH_2PO_4 and $Y(NO_3)_3$ solutions see lower enhancements of 58.82% and 56.62% and with background fluctuations of 2.98% and 2.19% respectively. A large fraction of the identified prompt γ-ray peaks in the spectrum of NaH_2PO_4 were situated after 1.4 MeV. The peaks which contribute to the enhancement for this solution originated from the first three excited states of ^{31}P, as discussed in Subsection 3.3.3. This is contrary to the $Y(NO_3)_3$ solution, for which all of the identified signatures of yttrium were situated in the 0.8 to 1.4 MeV region of interest, as discussed in Subsection 3.3.2. This is interesting as the phosphorus tracer element produces few peaks of very high cross section, contributing to a high enhancement in the region of interest and which is competitive with the enhancement yield obtained with the copper and yttrium solutions. Comparing the high concentration enhancements obtained in experiment to those of simulation, the first panel of Fig 3.21 shows the high concentration results of the solutions. Here the $CuSO_4$ solution has an enhancement of 57.3%, which is substantially lower than that of experiment.

The TOPAS physics lists accurately predicted the prompt γ-ray signature peaks of the copper solution in experiment, however, the predicted cross section was observed as lower in the simulation. This reduced cross section could suggest that the physics lists do not have as robust a grasp of the nuclear structure as that which was previously assumed. This is further exhibited in the 38.4% prompt γ-ray enhancement of the NaH_2PO_4 high

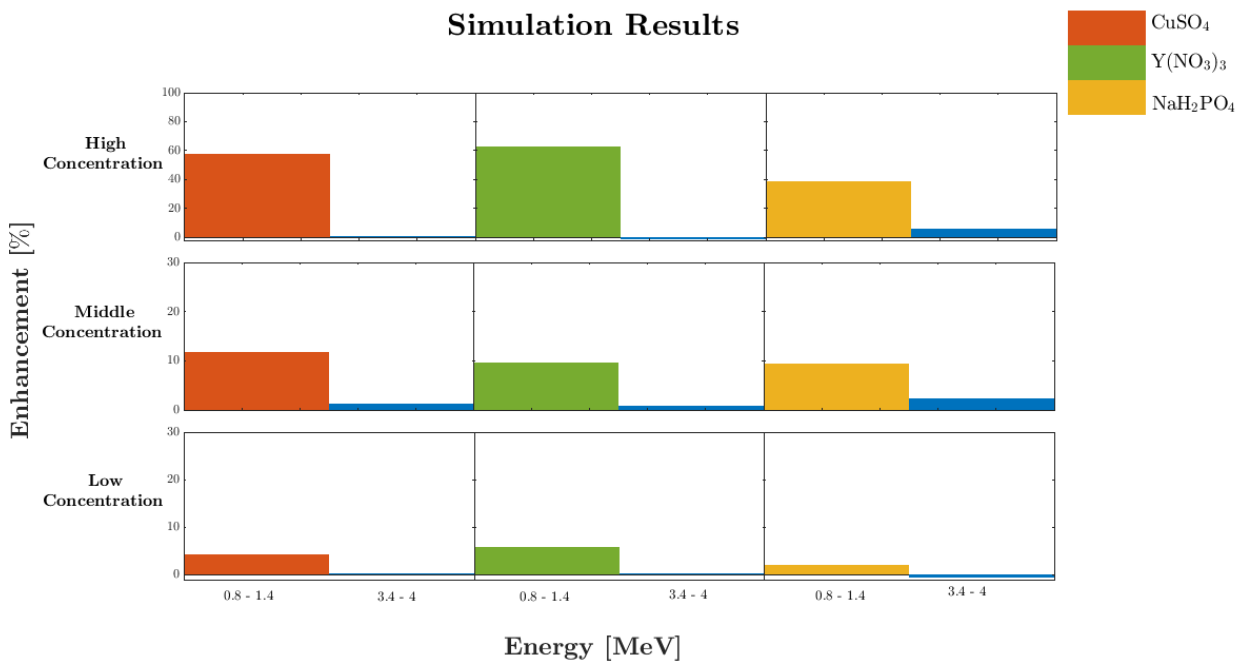

Figure 3.21: Simulation estimates of prompt γ-ray enhancement percentages and statistical fluctuation in the three salt targets.

concentration solution. This phosphorus solution, as discussed in the comparison between simulation and experiment in Subsection 3.3.3, is of lower enhancement due to the predicted low cross section of the 1.13 and 1.37 MeV excited states of ^{31}P in simulation. The peaks exhibited a greater cross section and FWHM in experimentation, which accounts for the 20% difference in enhancement percentages for this solution when comparing experiment to simulation. The $Y(NO_3)_3$ solution has an enhancement of 62.22% for the high concentration in simulation. This exceeds the enhancement of the experimental results for the same target. This is not surprising as it was discussed in Subsection 3.3.2 that the TOPAS simulation over predicted the response of the yttrium target in the solution, rendering low energy peaks of greater cross section than the experiment.

The statistical fluctuation in the high concentration results of Figs. 3.20 and 3.21 is consistently the lowest for the copper solution, with the phosphorus solution exhibiting the highest overall fluctuation. This fluctuation suggests that the phosphorus solution exhibits a lower enhancement than is calculated as the fluctuation in the background spectrum results in an over-calculation. The middle panels of Figs. 3.20 and 3.21 show the results of the middle concentrations of the solutions. Here the concentration of the element tracers in the solution are $\approx 1.4\%$ of the total mass. For this concentration the enhancement is still high, fluctuating around 10%, and the simulation and experimental results are in greater agreement. The exception is the phosphorus solution, where the

simulation has a prompt γ-ray enhancement of 9.29% and the experiment is 14.11%. This is due to the same behaviour exhibited at high concentration. The agreement between simulation and experiment is improved at medium concentration, where the discrepancy between data sets is not as large (10.79% in experiment and 9.62% in simulation) and the enhancement originates in both spectra predominantly due to the ^{88}Zr peak at 1.02 MeV. This agreement can be seen in Subsection 3.3.2 and is represented further in the Appendix Subsection .2.2 in a direct comparison between the simulation and experimental enhancements. The 0.2M medium concentration of $CuSO_4$ produced a prompt γ-ray enhancement of 12.91% in experiment and 11.73% in simulation. This agreement in enhancement values is demonstrated in Subsection 3.3.1, and well visualised in Appendix Subsection .2.1.

The enhancement results of greatest interest are those obtained at the lowest concentrations for each of the three targets. These are seen in the bottom panels of Figs. 3.20 and 3.21. These results give insight into the prompt γ-ray response above the chosen background spectrum which mimics that of the human body, providing insight into one of the criteria that qualify a tracer as a good candidate for use in PT treatment. The highest enhancement at the lowest concentration and with the east background fluctuation is attributed to the experimental results of the NaH_2PO_4 solution. The $CuSO_4$ solution sees a massive undershooting of the statistical enhancement in experiment. This undershooting is difficult to understand as it means that the salt target has fewer counts between 3.4 and 4 MeV than the water target. This should not be the case as the salt target has a marginally higher oxygen percentage than the water target and one would expect that the oxygen peaks would be the same or slightly higher in cross section at lower concentration in this region. This undershooting is not only characteristic of the copper solution, but it is the highest for this target. Irrespective of the reason for the undershooting, this behaviour suggests that the $CuSO_4$ solution might have a higher enhancement percentage in the 0.8 to 1.4 MeV region than the value which was calculated. The simulation results at low concentration of $CuSO_4$ have an enhancement of 4.3% with a low statistical fluctuation, lower than the 7.57% of the experiment that carried a fluctuation of 3.08%.

The low concentration NaH_2PO_4 solution, at 0.6% concentration of phosphorus, experiences an enhancement in the experimental results in Fig 3.20 of $\approx$ 6.39% of salt-to-water between 0.8 and 1.4 MeV. The majority of this enhancement is due to the excited state of ^{31}P at 1.278 MeV which shows very high cross section. The presence of this peak is exactly what this study aimed to find as it is easily distinguishable from the water and PMMA background and highlights the natural phosphorus solution as a promising candidate. This peak has a good FWHM and suggests the possibility of lowering the concentration of the isotope in the solution even further to obtain a therapeutic value. There is the likelihood that this percentage is a good candidate for therapeutic use already as once it is attached to a drug carrier, the uptake of that carrier in the human body would not be 100% and, thus, the toxicity may well be within a healthy range. However, studies should still be performed where the concentration is lowered further (perhaps scaled down by another 5 to 10%) to understand the performance of this prompt γ-ray signature at a

concentration which may mimic uptake in the human body with the drug carrier. There already exist drug carriers to which this isotope will bind, and which are already used. It is difficult to quantify the therapeutic range, however the toxicity effects will always be of less concern at the lowest observable concentration. The 0.6% phosphorus salt shows a greater cross section of signature peaks in experiment when compared to the 0.63% copper solution making it the overall more promising candidate of the two. Further, the presence of solely a high enhancement at low concentration does not define the viability of an element as a prompt γ-ray enhancer. The enhancement has to be accompanied by a well defined which is easily distinguishable from the background emitted by the human body. For this reason, the ^{31}P is the best candidate investigated. It is the only element which emits a signature peak which is easily distinguishable at low concentration from the water and PMMA background and with a high cross section.

3.3.5 Overview of Liquid Target Results

^{nat}Cu (^{63}Cu and ^{65}Cu), ^{89}Y and ^{31}P materials were characterised for their prompt γ-ray response as solid targets in Subsection 2.1.2. These elements were then employed in salt form as liquid targets and dissolved in pure water at concentrations of $\approx 5\%$, $\approx 1\%$ and $\approx 0.5\%$. The aim of irradiating element loaded targets was to characterise the target energy spectra, to determine which element presents the most promising prompt γ-ray signature spectrum and to compare the emission lines of the experimental data obtained to those of the TOPAS MC simulation performed in TOPAS of the experimental set-up. The liquid target was used as a reasonable solution to study not only the spectra of candidate elements, but also to investigate how the spectrum changes as a function of concentration.

The yttrium solution exhibited the least useful prompt γ-ray signature spectrum at low concentration due to the presence of a high cross sectional signature peak at an energy which corresponded to an oxygen emission, obscuring the signature in the water background. The enhancement in this target is high (5.76% in simulation and 4.36% in experiment), which emphasises the importance of both a reasonable magnitude of enhancement alongside a distinguishable emission peak as two criteria of a valuable prompt γ-ray signature. Without a visible peak, it is difficult to determine the presence of the element of interest in the background. In this instance the continuum is due to the presence of the element, but in a realistic scenario it can be caused by the presence of organic human tissue, bone, or the anatomical fluctuations between patients. The presence of solely an enhancement is not clear proof of the presence of the element but it is desirable to see a peak which is emitted by the element. Therefore, a distinctive peak structure is desirable as a proof of prompt γ-ray enhancement. The copper solution demonstrated the same lack in signature at low concentration. Both copper and yttrium are good candidates if one considers an overall enhancement, but they emit continuous spectra at a low concentration, or a prompt γ-ray signature which is situated at an energy

associated with emission due to water, where a signature peak is of interest. Due to this behaviour, it is too difficult to differentiate a true prompt γ-ray signal originating from the element from background. This negates their status as candidate elements for prompt γ-ray enhancement.

Phosphorus is the most promising as this element, apart from having application in clinics at the moment (stressing its lack of toxicity effects (49)), it emits a characteristic 1.278 MeV peak which is visible at 0.5% mass fraction of phosphorus. The 1.278 MeV peak present in the spectrum of NaH_2PO_4 solution is plotted for both experiment and simulation in Fig 3.22. The integral ratio of the counts in the region of this peak (1.24 to 1.305 MeV) for the solution at 0.2M divided by water has been performed to gauge the enhancement of this signature. The cross section of the experimental data is higher than that predicted by the TOPAS simulation model, producing enhancements of 17.667% and 5.236% respectively. Although a further 10% reduction in concentration would render a low enhancement based on the trend observed in the results investigated, the presence of the distinct peak at 1.27 MeV is the main focus. One notes that at 0.2M the NaH_2PO_4 solution saw a 6.39% enhancement in the 0.8 to 1.4 MeV range measured in experiment, which was actually a 17.667% enhancement of the distinct peak itself. The presence of a signature peak which is not lost to a continuous signal at low concentration is the main goal, which is observable in the phosphorus solution.

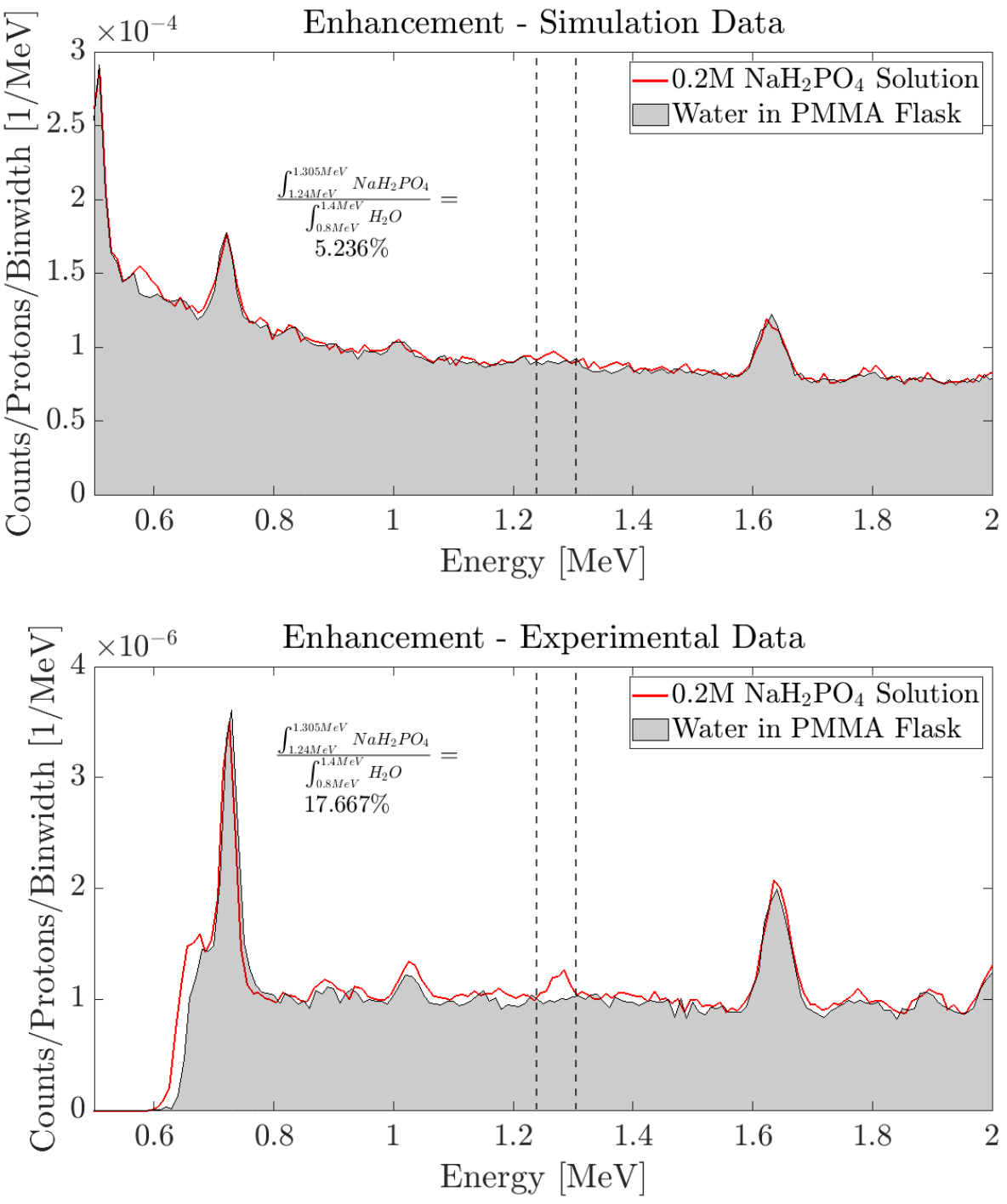

Figure 3.22: Plot of the 0.2M NaH_2PO solution showing the enhancement percentage of the prompt γ-ray signature peak at ≈ 1.278 MeV for simulation (top) and experiment (bottom).

Chapter 4

Conclusion

In this thesis I presented the results of a feasibility study on a novel strategy for real time dose verification of secondary prompt γ-ray emissions produced by way of proton–nuclear interactions within selected materials during proton irradiation by a 70 MeV proton pencil beam. This was carried out by identifying the candidate elements for the online treatment planning verification. The (p,X) reaction at tens of MeV was used to excite the nuclei and observe the relevant prompt γ-ray emissions and associated signature spectra using TALYS nuclear simulation software (5) and cross-checked against the NUDAT database (7). The element choice was the key to obtain a prompt γ-ray spectrum significantly different from the background produced by the abundant elements in the body (^{16}O, ^{12}C and ^{14}N) and for physiological considerations, i.e. uptake and toxicity effects. Water and PMMA were chosen as tissue-equivalent materials to mimic this background in the human body. This allowed for a comparison between the element prompt γ-ray spectra and a background which is similar to what would be encountered in a treatment plan.

The identified prompt γ-ray candidate elements were ^{nat}Cu, ^{89}Y and ^{31}P which were studied in both solid and liquid composition. The solid targets were in metal form with a cylindrical geometry of varying heights and radii, with the exception of ^{31}P, which had a solid box geometry. The study was then extended to resemble a more realistic medical scenario where the solid target elements were investigated in salt form so that they could be dissolved in water and PMMA to study their prompt γ-ray enhancements at concentrations which would be more viable in a treatment setting. Simulations and experiments were performed measuring the γ emission of the selected materials using different concentrations resembling the uptake of the elements in the tumor. The liquid target referred to two salt solution filled PMMA ($C_5H_8O_2$) flasks (to simulate the most abundant elements of the human body: carbon, oxygen and nitrogen) which were placed with their largest surfaces in contact to ensure the beam stopping in the target volume. The targets were created by using the salts: NaH_2PO_4, $Y(NO_3)_3$ and $CuSO_4$. The solutions were diluted to obtain different mass concentrations of the tracer elements of $\approx 5\%$, $\approx 1\%$ and $\approx 0.5\%$. The

molar mass percentages of the main elements studied were adjusted to be as close as possible to one another for accurate evaluations between salts at high, medium, and low concentrations could be undertaken.

The experiments were performed by the Nuclear Medicine Group at the Proton Therapy Center of Trento, Italy. These experiments were conducted to gain insight into the prompt γ-ray response of the elements of interest and to investigate the accuracy of the physics lists employed in the TOPAS simulation in terms of cross section. In experiment, a proton pencil beam was accelerated to 70 MeV by the cyclotron. The beam energy was pseudo-monoenergetic, with an energy spread of 0.9%. The set-up was such that after interaction with the target, the secondaries (γ-rays, protons, neutrons, etc.) were detected by a 3" $\times$ 3" $LaBr_3$:Ce detector. These secondary particles were vetoed by charge using an EJ-200 plastic scintillator situated in front of the detector and lead shielding blocks were placed in between the $LaBr_3$:Ce detector and the beam to reduce the background.

All simulations were performed using TOPAS version 3.6.1 and with the computing resources as provided by the Centre for High Performance Computing (CHPC) Lengau Cluster. The simulation environment was based on the geometry of the experiment and used to predict the prompt γ-ray spectra of the candidate elements by measuring the energy deposition on the volume of an $LaBr_3$:Ce detector originating from the irradiated target. All simulations were computed using the TOPAS default physics lists which is highly documented as the best option for PT dose calculation applications. This list includes physics models which handle all secondary particles, not only protons. It is adapted to the latest Geant4 release to render results which closely match those described in (41).

The first approach in this study was to see whether the elements chosen produce characteristic γ-rays which are different to those of water. This was done assessing the prompt γ-ray response of the solid targets. The idea was then to see if the characteristic prompt γ-ray emission spectrum would remain observable when the concentration of the element was reduced, achieved by using the liquid targets. Maximum absorption of the marker in the tumor is key, and detection of the γ particles emitted by the marker aimed at the production of a signature γ spectrum induced by the proton beam which was different to the background (^{12}C, ^{16}O and ^{14}N). I investigated the emission spectra of γ-rays exiting the target and assessed the enhancement with respect to the water background, comparing simulation and experimental results. I demonstrated how proton reactions can produce signature prompt γ-rays related to the material irradiated. The minimum material concentration required to obtain a significant enhancement was also studied.

The results show that the prompt γ-ray spectra differ significantly for each type of tissue studied. The investigation into the solid target form of the elements of interest presented interesting results. All three elements displayed a good prompt γ-ray signature spectrum which was different to the background. This prompt γ-ray signature was concentrated in the low energy region of the spectrum (0.8 - 2 MeV) and the water spectrum dominated

the higher (> 3 MeV) region, allowing for ease in distinguishing the element prompt γ-ray response from the background. The exception to this was seen in the PMMA response which presented few low energy peaks which coincide with the region of element prompt γ-ray enhancement. This contamination presented a few difficulties when investigating the prompt γ-ray response of the liquid target form of the elements. The prompt γ-ray response seen in the TOPAS simulations produced the identified peaks seen in experiment but underestimated the reaction cross section. The ^{89}Y target was an unusual case as the simulation and experiment largely disagreed. For this target the simulation of the irradiated element presented discrepancies in cross section as well as decay fragments and few fragments were common between the two data sets.

The liquid target form made it possible to study the element concentrations within the tumor region. The liquid $CuSO_4$ target showed a good agreement in the prompt γ-ray peaks produced in simulation and experimental results. Underestimation of simulation peak cross section was encountered as in the solid target results. In terms of prompt γ-ray signature, the $CuSO_4$ target produced a well-defined prompt γ-ray emission in experiment at 1.025 MeV corresponding to ^{65}Cu*, the cross section for which was low in simulation. This peak was not a true prompt γ-ray signature as the experimental cross section was a combination of the prompt γ-ray signature and a PMMA background contribution. For this reason it was observed that the simulation results presented a more true estimation of the yield. The integral enhancement of this peak in the 0.8 to 1.4 MeV region investigated was therefore seen, for the low concentration, as higher (7.57%) in experiment than in the simulation (4.3%) due to the background contribution. This background contamination of the peak obscures the prompt γ-ray signature. For this reason, this prompt γ-ray signature at low concentration of the tracer element would be very difficult to distinguish from human tissue background in a PT treatment. The $Y(NO_3)_3$ liquid target exhibited few shared prompt γ-ray peaks at high concentration which was reduced to just one which was easily distinguishable with high cross section at low concentration. This peak corresponded to ^{88}Zr* at 1.075 MeV and the signature is obscured by the same PMMA signal in the experimental results as was the case with the $CuSO_4$ target. The simulation suggests that without the PMMA signal this peak might be more defined, however, the same problem arose as with the liquid $CuSO_4$ target as the peak is not well defined due to this background contaminant. The $Y(NO_3)_3$ liquid target exhibited a high enhancement percentage at low concentration (5.76% in simulation and 4.36% in experiment), which emphasises the importance of both a reasonable magnitude of enhancement alongside a distinguishable emission peak as two criteria of a valuable prompt γ-ray signature. Without a visible peak, there is no signature evidence of the element of interest in the water. In this instance the continuum is due to the presence of the element, but in a realistic scenario it can be caused by the presence of organic human tissue, bone, or the anatomical fluctuations between patients. The presence of solely an enhancement is not proof of the presence of the element but it is desirable to see a peak which is emitted by the element. Therefore, a clear peak structure is desirable as a proof of prompt γ-ray enhancement. The copper solution demonstrates the same lack in signature at low concentration. The results of the

simulation for the $Y(NO_3)_3$ solution produced a marginally greater enhancement than the $CuSO_4$, a behaviour which was the contrary in the experimental results. The experimental results show an $\approx 20\%$ greater prompt γ-ray yield in $CuSO_4$ than $Y(NO_3)_3$, suggesting that the TOPAS physics lists greatly underestimate the nuclear structure of the ^{nat}Cu material. Both ^{nat}Cu and ^{89}Y are good candidates if one considers an overall enhancement, but they emit continuous spectra at a low concentration where a signature peak is of interest. Due to this behaviour, it is too difficult to distinguish where there is a true signal originating from the element of interest and where there exists merely background. Phosphorus is the most promising as this element, apart from having application in clinics at the moment (stressing its lack of toxicity effects as an inorganic compound (49)), it emits a characteristic 1.278 MeV peak which is visible at 0.5% mass fraction of phosphorus and which was distinguishable with high cross section when compared to the water and flask background spectrum. Further, this prompt γ-ray signature emission is not contaminated by an emission originating from the background and has a very low associated statistical background fluctuation. Phosphorus shows to be the most promising candidate for further investigation as a prompt γ-ray enhancement trace element.

In conclusion, the relative intensity of the characteristic γ-rays emitted from a given element was shown to be proportional to the concentration of each element in that solution. Further, it has been demonstrated that loading the tumor with a drug-delivered element can enhance the emission of prompt γ-rays exiting the patient. Overall, the Monte Carlo model of the Trento PT centre experimental beam-line set-up proved to be successful in replicating prompt γ-ray peak production numbers to within 1.24% at low energy. Further improvement to the current physics model by being able to fully incorporate the Doppler broadening effect of the higher energy (> 4 MeV) peaks would greatly increase the accuracy of the simulated response of water after proton bombardment and thus improve the comparison in enhancement between simulation and experiment. This study has uncovered shortfalls in the inelastic nuclear cross section data employed by TOPAS physics lists, which are relevant to clinical proton radiotherapy environment and have prompted a verification of the existing cross section data and an investigation into producing more cross section data at the energies relevant to PT. This is partly attributed to the photon evaporation libraries implemented in the TOPAS simulation physics lists, which are based on insubstantial experimental data which cause a limited accuracy. ^{31}P has been demonstrated as the promising element due to the emission of a characteristic high energetic γ after interacting with the proton beam, a peak which is easily discernible from the background at an elemental mass concentration of 0.6% of the target.

The enhancement calculations as performed in this study need to be further investigated to determine if it is a statistical fluctuation in the background present or if it is a statistically robust value which renders the results obtained. In order to investigate if the results obtained from this project have a real potential in clinical application, a detailed study on phantom that resemble human anatomy composed of a more accurate tissue equivalent material needs to be conducted. This would allow a for a more detailed understanding of whether this ^{31}P 1.278 MeV peak would still provide a signature in a

real therapeutic environment. Further assessment is required to determine a more realistic range or order of magnitude of a concentration of the element within the tumor, which is not a trivial question and requires deep knowledge into the chemistry associated with the uptake of this element of interest in the human body once it has been bound to a non-toxic drug-carrier.

Bibliography

[1] A.-C. Knopf and A. Lomax, "In vivoproton range verification: a review," *Physics in Medicine and Biology*, vol. 58, pp. R131–R160, 2013.

[2] E. T. Vitti and J. L. Parsons, "The radiobiological effects of proton beam therapy: Impact on dna damage and repair," *Cancers*, vol. 11, no. 7, 2019. [Online]. Available: https://www.mdpi.com/2072-6694/11/7/946

[3] S. Dönmez, *Radiation Detection and Measurement*, 2017. [Online]. Available: http://cms.galenos.com.tr/Uploads/Article_16396/NTS-3-3.pdf

[4] J. Krimmer, D. Dauvergne, J. M. Létang, and Testa, "Prompt-gamma monitoring in hadrontherapy: A review," *Nuclear Instruments and Methods in Physics Research, Section A: Accelerators, Spectrometers, Detectors and Associated Equipment*, vol. 878, no. May 2017, pp. 58–73, 2018. [Online]. Available: http://dx.doi.org/10.1016/j.nima.2017.07.063

[5] "Talys," 2020. [Online]. Available: https://tendl.web.psi.ch/tendl_2019/talys.html

[6] K. Alzimami, E. Abuelhia, Z. Podolyak, A. Ioannou, and N. M. Spyrou, "Characterization of labr3: Ce and lacl3: Ce scintillators for gamma-ray spectroscopy," *Journal of Radioanalytical and Nuclear Chemistry*, vol. 278, no. 3, pp. 755–759, 2008.

[7] "NuDAT (National Nuclear Data Center (NNDC)) search and plot nuclear structure and decay data interactively," https://www.nndc.bnl.gov/nudat3/.

[8] "RIVELATORE 6," 2015.

[9] J. M. Verburg, H. A. Shih, and J. Seco, "Simulation of prompt gamma-ray emission during proton radiotherapy," *Physics in Medicine and Biology*, vol. 57, no. 17, pp. 5459–5472, 2012.

[10] "Cancer," 2022. [Online]. Available: https://www.who.int/health-topics/cancer#tab=tab_1

[11] R. R. Wilson, "Radiological use of fast protons," *Radiology*, vol. 47, no. 5, pp. 487–491, 1946.

[12] J. C. Polf and K. Parodi, "Imaging particle beams for cancer treatment," *Physics Today*, vol. 68, no. 10, pp. 28–33, 2015.

[13] H. Paganetti, "Range uncertainties in proton therapy and the role of monte carlo simulations," *Physics in Medicine and Biology*, vol. 57, no. 11, pp. R99–R117, 2012.

[14] *Proton Beam Therapy*. IOP Publishing, 2017. [Online]. Available: https://dx.doi.org/10.1088/978-0-7503-1370-4

[15] D. Jones, "Radiation oncology: A physicist's-eye view radiation oncology: A physicist's-eye view , michael goitein , springer, new york," *Physics Today*, vol. 61, no. 12, pp. 55–56, 2008.

[16] F. Tommasino and M. Durante, "Proton radiobiology," *Cancers*, vol. 7, no. 1, pp. 353–381, 2015.

[17] E. L. Alpen, "Interaction of radiation with matter," *Radiation Biophysics*, pp. 50–77, 1998.

[18] H. Paganetti, "Proton relative biological effectiveness – uncertainties and opportunities," *International Journal of Particle Therapy*, vol. 5, no. 1, pp. 2–14, 2018.

[19] D. Dauvergne and A. Wronska, *Range verification by means of prompt-gamma detection in particle therapy*, 01 2020.

[20] J. C. Polf and K. Parodi, "Imaging particle beams for cancer treatment," *Physics Today*, vol. 68, no. 10, pp. 28–33, 2015.

[21] V. Ferrero, E. Fiorina, M. Morrocchi, F. Pennazio, G. Baroni, G. Battistoni, N. Belcari, N. Camarlinghi, M. Ciocca, and A. e. a. Del Guerra, "Online proton therapy monitoring: clinical test of a silicon-photodetector-based in-beam pet," *Scientific Reports*, vol. 8, no. 1, 2018.

[22] H. D. Maccabee, U. Madhvanath, and M. R. Raju, "Tissue activation studies with alpha-particle beams," *Physics in Medicine and Biology*, vol. 14, no. 2, pp. 213–224, 1969.

[23] K. Parodi, T. Bortfeld, and T. Haberer, "Comparison between in-beam and offline positron emission tomography imaging of proton and carbon ion therapeutic irradiation at synchrotron- and cyclotron-based facilities," *International Journal of Radiation Oncology*Biology*Physics*, vol. 71, no. 3, pp. 945–956, 2008.

[24] K. Parodi, H. Paganetti, H. A. Shih, S. Michaud, J. S. Loeffler, T. F. DeLaney, N. J. Liebsch, J. E. Munzenrider, A. J. Fischman, A. Knopf, and T. Bortfeld, "Patient study of in vivo verification of beam delivery and range, using positron emission tomography and computed tomography imaging after proton therapy," *Int. J. Radiat. Oncol. Biol. Phys.*, vol. 68, no. 3, pp. 920–934, 2007.

[25] J. Jeyasugiththan and S. Peterson, "Su-e-j-142: Prompt gamma emission measurements from a passively scattered proton beam on targets containing 16o, 12c and 14n," *Medical Physics*, vol. 42, no. 6Part9, pp. 3297–3297, 2015.

[26] J. C. Polf, S. Peterson, G. Ciangaru, M. Gillin, and S. Beddar, "Prompt gamma-ray emission from biological tissues during proton irradiation: a preliminary study," *Phys. Med. Biol.*, vol. 54, no. 3, pp. 731–743, 2009.

[27] M. Zarifi, S. Guatelli, D. Bolst, B. Hutton, A. Rosenfeld, and Y. Qi, "Characterization of prompt gamma-ray emission with respect to the bragg peak for proton beam range verification: A monte carlo study," *Physica Medica*, vol. 33, pp. 197–206, 2017. [Online]. Available: https://www.sciencedirect.com/science/article/pii/S1120179716311188

[28] J. C. Polf, R. Panthi, D. S. Mackin, M. McCleskey, A. Saastamoinen, B. T. Roeder, and S. Beddar, "Measurement of characteristic prompt gamma rays emitted from oxygen and carbon in tissue-equivalent samples during proton beam irradiation," vol. 58, no. 17, pp. 5821–5831, aug 2013. [Online]. Available: https://doi.org/10.1088/0031-9155/58/17/5821

[29] F. Roellinghoff, A. Benilov, D. Dauvergne, G. Dedes, N. Freud, G. Janssens, J. Krimmer, J. M. Létang, M. Pinto, and D. e. a. Prieels, "Real-time proton beam range monitoring by means of prompt-gamma detection with a collimated camera," *Physics in Medicine and Biology*, vol. 59, no. 5, pp. 1327–1338, 2014.

[30] I. Perali, A. Celani, L. Bombelli, C. Fiorini, F. Camera, E. Clementel, S. Henrotin, G. Janssens, D. Prieels, and F. e. a. Roellinghoff, "Prompt gamma imaging of proton pencil beams at clinical dose rate," *Physics in Medicine and Biology*, vol. 59, no. 19, pp. 5849–5871, 2014.

[31] J. Smeets, F. Roellinghoff, D. Prieels, F. Stichelbaut, A. Benilov, P. Busca, C. Fiorini, R. Peloso, M. Basilavecchia, T. Frizzi, J. C. Dehaes, and A. Dubus, "Prompt gamma imaging with a slit camera for real-time range control in proton therapy," *Physics in Medicine and Biology*, vol. 57, no. 11, pp. 3371–3405, 2012.

[32] C. Richter, G. Pausch, S. Barczyk, M. Priegnitz, I. Keitz, J. Thiele, J. Smeets, F. V. Stappen, L. Bombelli, C. Fiorini, L. Hotoiu, I. Perali, D. Prieels, W. Enghardt, and M. Baumann, "First clinical application of a prompt gamma based in vivo proton range verification system," *Radiotherapy and Oncology*, vol. 118, no. 2, pp. 232–237, 2016. [Online]. Available: http://dx.doi.org/10.1016/j.radonc.2016.01.004

[33] Y. Xie, E. H. Bentefour, G. Janssens, J. Smeets, F. V. Stappen, L. Hotoiu, L. Yin, D. M. Dolney, S. Avery, F. O'Grady, D. Prieels, J. E. Mcdonough, T. D. Solberg, R. A. Lustig, A. Lin, and B.-K. K. Teo, "Prompt gamma imaging for in vivo range verification of pencil beam scanning proton therapy." *International journal of radiation oncology, biology, physics*, vol. 99 1, pp. 210–218, 2017.

[34] J. Ready, V. Negut, L. Mihailescu, and K. Vetter, "Prompt gamma imaging with a multi-knife-edge slit collimator: Evaluation for use in proton beam range verification," *Medical Physics*, vol. 43, no. 6Part31, pp. 3717–3717, 2016.

[35] J. Smeets, F. Roellinghoff, G. Janssens, I. Perali, A. Celani, C. Fiorini, N. Freud, É. Testa, and D. Prieels, "Experimental comparison of knife-edge and multi-parallel slit collimators for prompt gamma imaging of proton pencil beams," *Frontiers in Oncology*, vol. 6, 2016.

[36] C. Golnik, F. Hueso-González, A. Müller, P. Dendooven, W. Enghardt, F. Fiedler, T. Kormoll, K. Roemer, J. Petzoldt, A. E. Wagner, and G. Pausch, "Range assessment in particle therapy based on prompt γ-ray timing measurements." *Physics in medicine and biology*, vol. 59 18, pp. 5399–422, 2014.

[37] J. M. Verburg, K. Riley, T. Bortfeld, and J. Seco, "Energy- and time-resolved detection of prompt gamma-rays for proton range verification," *Physics in Medicine and Biology*, vol. 58, no. 20, pp. L37–L49, 2013.

[38] "Phosphorus," 2022. [Online]. Available: https://en.wikipedia.org/wiki/Phosphorus#Compounds

[39] F. Tommasino, M. Rovituso, S. Fabiano, S. Piffer, C. Manea, S. Lorentini, S. Lanzone, Z. Wang, M. Pasini, W. J. Burger, C. La Tessa, E. Scifoni, M. Schwarz, and M. Durante, "Proton beam characterization in the experimental room of the Trento Proton Therapy facility," *Nuclear Instruments and Methods in Physics Research, Section A: Accelerators, Spectrometers, Detectors and Associated Equipment*, vol. 869, no. June, pp. 15–20, 2017. [Online]. Available: http://dx.doi.org/10.1016/j.nima.2017.06.017

[40] "Topas mc inc." 2022. [Online]. Available: http://www.topasmc.org/

[41] C. Zacharatou Jarlskog and H. Paganetti, "Physics settings for using the geant4 toolkit in proton therapy," *IEEE Transactions on Nuclear Science*, vol. 55, no. 3, pp. 1018–1025, 2008.

[42] "Characterization of large volume 3.5×8 LaBr 3:Ce detectors," *Nuclear Instruments and Methods in Physics Research, Section A: Accelerators, Spectrometers, Detectors and Associated Equipment*, vol. 729, pp. 910–921, 2013.

[43] "Lanthanum bromide detectors," 2021. [Online]. Available: https://www.ortec-online.com/products/radiation-detectors/scintillation-detectors/scintillation-detector-types/lanthanum-bromide-detectors

[44] E. I. Prosper, O. J. Abebe, and U. J. Ogri, "Characterisation of Cerium-Doped Lanthanum Bromide scintillation detector," *Am. J. Phys. Educ*, vol. 6, no. 1, p. 162, 2012. [Online]. Available: http://www.lajpe.org

[45] A. Belhout, J. Kiener, A. Coc, J. Duprat, C. Engrand, C. Fitoussi, M. Gounelle, A. Lefebvre-Schuhl, N. d. Séréville, and V. e. a. Tatischeff, "gamma-ray production by proton and alpha-particle induced reactions on c12,o16,mg24, and fe," *Physical Review C*, vol. 76, no. 3, 2007.

[46] A. Koide, J. Kataoka, T. Masuda, S. Mochizuki, T. Taya, K. Sueoka, L. Tagawa, K. Fujieda, T. Maruhashi, T. Kurihara, and T. Inaniwa, "Precision imaging of 4.4 MeV gamma rays using a 3-D position sensitive Compton camera," *Scientific Reports*, vol. 8, no. 1, pp. 1–10, 2018. [Online]. Available: http://dx.doi.org/10.1038/s41598-018-26591-2

[47] J. C. Polf, S. Peterson, M. McCleskey, B. T. Roeder, A. Spiridon, S. Beddar, and L. Trache, "Measurement and calculation of characteristic prompt gamma ray spectra emitted during proton irradiation," *Physics in Medicine and Biology*, vol. 54, no. 22, pp. 519–527, 2009.

[48] E. E. Kim, *Essentials of Nuclear Medicine Imaging*, 2008, vol. 49, no. 12.

[49] R. G. Steen, "Characterization of tumor hypoxia by 31P MR spectroscopy," *American Journal of Roentgenology*, vol. 157, no. 2, pp. 243–248, 1991.

[50] J. Källne and O. Sundberg, "Excited States of 31P and 32S Studied in the (p, p') Reaction at 185 MeV," *Physica Scripta*, vol. 4, no. 6, pp. 243–255, 1971.

[51] T. Wakatsuki, Y. Hirao, E. Okada, and I. Miura, "Gamma rays from the proton bombardment of 31p and the excited states of 31p," *Journal of the Physical Society of Japan*, vol. 16, no. 12, pp. 2385–2392, 1961. [Online]. Available: https://doi.org/10.1143/JPSJ.16.2385

Chapter 5

Appendix

.1 Listings of Some Codes as used in Simulation

```
#
# General
#
projectile p
element S
mass 32
energy 70
#
# Output
#
outspectra y
filespectrum g
outgamdis y
outpopulation y
outdiscrete y
adddiscrete y
```

Listing 1: Example of TALYS code used to gain insight into the predicted cross sections and residuals generated by a 70 MeV prootn beam irradiating a target (Here ^{32}S).

```
i:Ts/NumberOfThreads                                = 0
i:Ts/Seed                                                    = ${SEED}

#************************** WORLD
s:Ge/World/Material                                 = "Air"
d:Ge/World/HLX                                              =  1 m
d:Ge/World/HLY                                              =  1 m
d:Ge/World/HLZ                                              =  1.5 m
b:Ge/World/Invisible                                = "FALSE"

#************************** BEAM
s:So/Demo/Type                                              = "Beam"          #
    Beam, Isotropic, Emittance or PhaseSpace
s:So/Demo/Component                                 = "BeamPosition"
d:Ge/BeamPosition/TransZ                            =  0 cm           # so that
    the beam is at the center of the World
s:So/Demo/BeamParticle                              = "proton"
d:So/Demo/BeamEnergy                                = 70 MeV
u:So/Demo/BeamEnergySpread                          = 0.9             #
    Expressed in terms of percentage of the mean energy
s:So/Demo/BeamPositionDistribution      = "None"          # None, Flat or
    Gaussian
s:So/Demo/BeamAngularDistribution       = "Gaussian"      # None, Flat or
    Gaussian
d:So/Demo/BeamAngularCutoffX            = 90. deg         # X cutoff of
    angular distrib (if Flat or Gaussian)
d:So/Demo/BeamAngularCutoffY            = 90. deg         # Y cutoff of
    angular distrib (if Flat or Gaussian)
d:So/Demo/BeamAngularSpreadX            = 0.0057 rad      # X angular
    distribution (if Gaussian)
d:So/Demo/BeamAngularSpreadY            = 0.0057 rad      # Y angular
    distribution (if Gaussian)
i:So/Demo/NumberOfHistoriesInRun        = 200             # number of
    particles
i:Ts/ShowHistoryCountAtInterval         = 2000000000

#************************** MATERIALS
#isotope Cu63
i:Is/Cu63/Z                                 = 29
i:Is/Cu63/N                                 = 63
d:Is/Cu63/A                                 = 62.929597 g/mole
#element Cu63
s:El/ElCu63/Symbol                          = "ElCu63"
sv:El/ElCu63/IsotopeNames       = 1 "Cu63"
uv:El/ElCu63/IsotopeAbundances = 1 100.
#Material
sv:Ma/MatCu/Components          =4 "Copper" "Sulfur" "Hydrogen" "Oxygen"
uv:Ma/MatCu/Fractions           = 4 0.0508 0.0257 0.0976 0.8259
d:Ma/MatCu/Density                      = 1.249 g/cm3
#PMMA flask
sv:Ma/MatFlask/Components       =3 "Carbon" "Hydrogen" "Oxygen"
uv:Ma/MatFlask/Fractions        = 3 0.599848 0.080538 0.319614
d:Ma/MatFlask/Density           = 1.249 g/cm3
```

```
44
45 #************************** FLASKS
46 s:Ge/Flask1/Type                = "TsBox"
47 s:Ge/Flask1/Material            = "MatFlask"
48 s:Ge/Flask1/Parent              = "World"
49 dc:Ge/Flask1/HLX                = 2.5 cm
50 dc:Ge/Flask1/HLY                = 2.5 cm
51 dc:Ge/Flask1/HLZ                = 1.25 cm
52 dc:Ge/Flask1/TransX             = 0. m
53 dc:Ge/Flask1/TransY             = 0. m
54 dc:Ge/Flask1/TransZ             = -118.75 cm
55 dc:Ge/Flask1/RotX               = 0. deg
56 dc:Ge/Flask1/RotY               = 0. deg
57 dc:Ge/Flask1/RotZ               = 0. deg
58 sc:Ge/Flask1/DrawingStyle       = "FullWireFrame"
59 sc:Ge/Flask1/Color                     = "yellow"
60 s:Ge/Flask2/Type                = "TsBox"
61 s:Ge/Flask2/Material            = "MatFlask"
62 s:Ge/Flask2/Parent              = "World"
63 dc:Ge/Flask2/HLX                = 2.5 cm
64 dc:Ge/Flask2/HLY                = 2.5 cm
65 dc:Ge/Flask2/HLZ                = 1.25 cm
66 dc:Ge/Flask2/TransX             = 0. m
67 dc:Ge/Flask2/TransY             = 0. m
68 dc:Ge/Flask2/TransZ             = -121.25 cm
69 dc:Ge/Flask2/RotX               = 0. deg
70 dc:Ge/Flask2/RotY               = 0. deg
71 dc:Ge/Flask2/RotZ               = 0. deg
72 sc:Ge/Flask2/DrawingStyle       = "FullWireFrame"
73 sc:Ge/Flask2/Color                     = "yellow"
74
75 #************************** COPPER TARGET
76 s:Ge/Target1/Type               = "TsBox"
77 s:Ge/Target1/Material           = "MatCu"
78 s:Ge/Target1/Parent             = "Flask1"
79 dc:Ge/Target1/HLX               = Ge/Flask1/HLX - 0.113 cm
80 dc:Ge/Target1/HLY               = Ge/Flask1/HLY - 0.113 cm
81 dc:Ge/Target1/HLZ               = Ge/Flask1/HLZ - 0.113 cm
82 dc:Ge/Target1/TransX            = 0. m
83 dc:Ge/Target1/TransY            = 0. m
84 dc:Ge/Target1/TransZ            = 0 m
85 dc:Ge/Target1/RotX              = 0. deg
86 dc:Ge/Target1/RotY              = 0. deg
87 dc:Ge/Target1/RotZ              = 0. deg
88 sc:Ge/Target1/DrawingStyle      = "Solid"
89 sc:Ge/Target1/Color             = "green"
90 s:Ge/Target2/Type               = "TsBox"
91 s:Ge/Target2/Material           = "MatCu"
92 s:Ge/Target2/Parent             = "Flask2"
93 dc:Ge/Target2/HLX               = Ge/Flask2/HLX - 0.113 cm
94 dc:Ge/Target2/HLY               = Ge/Flask2/HLY - 0.113 cm
95 dc:Ge/Target2/HLZ               = Ge/Flask2/HLZ - 0.113 cm
96 dc:Ge/Target2/TransX            = 0. m
```

```
 97 dc:Ge/Target2/TransY              = 0. m
 98 dc:Ge/Target2/TransZ              = 0 m
 99 dc:Ge/Target2/RotX                = 0. deg
100 dc:Ge/Target2/RotY                = 0. deg
101 dc:Ge/Target2/RotZ                = 0. deg
102 sc:Ge/Target2/DrawingStyle        = "Solid"
103 sc:Ge/Target2/Color               = "green"
104
105 #************************** SCINTILLATOR
106 s:Ge/Scint/Type                   = "TsBox"
107 s:Ge/Scint/Parent                 = "World"
108 s:Ge/Scint/Material               = "ScintMat"
109 dc:Ge/Scint/HLX                   = 2.5 mm
110 dc:Ge/Scint/HLY                   = 5 cm
111 dc:Ge/Scint/HLZ                   = 5 cm
112 dc:Ge/Scint/TransX                = 20 cm
113 dc:Ge/Scint/TransY                = 0. m
114 dc:Ge/Scint/TransZ                = -1.20 m
115 dc:Ge/Scint/RotX                  = 45. deg
116 dc:Ge/Scint/RotY                  = 0. deg
117 dc:Ge/Scint/RotZ                  = 0. deg
118 sc:Ge/Scint/DrawingStyle          = "Solid"
119 sc:Ge/Scint/Color                        = "violet"
120 sv:Ma/ScintMat/Components         = 2 "Hydrogen" "Carbon"
121 uv:Ma/ScintMat/Fractions          = 2 0.08474 0.91526
122 d:Ma/ScintMat/Density             = 1.032 g/cm3
123
124 #************************** ALUMINIUM FRAME LABR DETECTOR
125 s:Ge/Alu/Type                              = "TsCylinder"
126 s:Ge/Alu/Material                          = "Aluminum"
127 s:Ge/Alu/Parent                            = "World"
128 dc:Ge/Alu/HL                               = 44.9 mm
129 dc:Ge/Alu/RMax                             = 43.2 mm
130 dc:Ge/Alu/TransX                           = 26 cm
131 dc:Ge/Alu/TransY                           = 0. m
132 dc:Ge/Alu/TransZ                           = -1.2 m
133 dc:Ge/Alu/RotX                            = 0. deg
134 dc:Ge/Alu/RotY                            = 90 deg
135 dc:Ge/Alu/RotZ                            = 0. deg
136 sc:Ge/Alu/DrawingStyle           = "FullWireFrame"
137 sc:Ge/Alu/Color                           = "blue"
138
139 #************************** LABR DETECTOR
140 s:Ge/Labr/Type                             = "TsCylinder"
141 s:Ge/Labr/Material                         = "LabrMat"
142 s:Ge/Labr/Parent                           = "Alu"
143 dc:Ge/Labr/HL                              = 41.9 mm
144 dc:Ge/Labr/RMax                            = 40.2 mm
145 dc:Ge/Labr/TransX                 = 0. m
146 dc:Ge/Labr/TransY                 = 0. m
147 dc:Ge/Labr/TransZ                 = 0. m
148 dc:Ge/Labr/RotX                   = 0. deg
149 dc:Ge/Labr/RotY                   = 0. deg
```

```
150 dc:Ge/Labr/RotZ                  = 0. deg
151 sc:Ge/Labr/DrawingStyle          = "Solid"
152 sc:Ge/Labr/Color                        = "red"
153 sv:Ma/LabrMat/Components         = 2 "Lanthanum" "Bromine"
154 uv:Ma/LabrMat/Fractions          = 2 0.3669 0.6331
155 d:Ma/LabrMat/Density             = 5.08 g/cm3
156
157 #************************** LEAD SHIELD
158 s:Ge/Lsc/Type                              = "TsBox"
159 s:Ge/Lsc/Parent                            = "World"
160 s:Ge/Lsc/Material                          = "Lead"
161 dc:Ge/Lsc/HLX                             = 41.9 mm
162 dc:Ge/Lsc/HLY                             = 40.2 mm
163 dc:Ge/Lsc/HLZ                             = 3 cm
164 dc:Ge/Lsc/TransX                          = 26 cm
165 dc:Ge/Lsc/TransY                          = 0. m
166 dc:Ge/Lsc/TransZ                          = -1.05 m
167 dc:Ge/Lsc/RotX                           = 0. deg
168 dc:Ge/lsc/RotY                           = 0. deg
169 dc:Ge/Lsc/RotZ                           = 0. deg
170 sc:Ge/Lsc/DrawingStyle          = "Solid"
171 sc:Ge/Lsc/Color                          = "grey"
172
173 #************************** VISUALISATION
174 s:Gr/Vis/Type                    = "OpenGL"
175 b:Ts/UseQt                                      = "True"
176 i:Gr/Vis/WindowSizeX             = 1024
177 i:Gr/Vis/WindowSizeY             = 100
178 b:Gr/Vis/IncludeAxes             = "True"
179 s:Gr/Vis/AxesComponent           = "Target2"     # Component in which to
        center the axes. Defaults to World.
180 d:Gr/Vis/AxesSize                          = 1.2 m
181 d:Gr/Vis/Theta              = 55 deg
182 d:Gr/Vis/Phi                = 20 deg
183 s:Gr/Vis/Projection              = "Perspective"
184 d:Gr/Vis/PerspectiveAngle        = 45 deg
185 u:Gr/Vis/Zoom                    = 10.
186 b:Gr/Vis/IncludeGeometry         = "True"
187 b:Ts/PauseBeforeQuit             = "True"
188
189 #************************** SCORING
190 s:Sc/MyScorer2/OutputFile                      =
        "TARGET_LaBrZPlusSurface_PS_${SEED}"
191 s:Sc/MyScorer2/OutputType                      = "ASCII"
192 b:Sc/MyScorer2/OutputAfterRun          = "True"
193 s:Sc/MyScorer2/Quantity                        = "PhaseSpace"
194 s:Sc/MyScorer2/Surface                         = "Labr/ZPlusSurface"
195 sv:Sc/MyScorer2/OnlyIncludeParticlesNamed = 3 "neutron" "gamma" "proton"
196 sv:Sc/MyScorer2/OnlyIncludeParticlesFromComponentOrSubComponentsOf = 2
        "Target1" "Target2"
197 b:Sc/MyScorer2/IncludeEventID           = "True"
198 b:Sc/MyScorer2/IncludeTrackID           = "True"
199 s:Sc/MyScorer2/IfOutputFileAlreadyExists = "Increment"
```

```
b:Sc/MyScorer2/IncludeTimeOfFlight      = "True"

s:Sc/MyScorer3/OutputFile                       =
    "TARGET_LaBrOuterCurvedSurface_PS_${SEED}"
s:Sc/MyScorer3/OutputType                       = "ASCII"
b:Sc/MyScorer3/OutputAfterRun           = "True"
s:Sc/MyScorer3/Quantity                         = "PhaseSpace"
s:Sc/MyScorer3/Surface                          = "Labr/OuterCurvedSurface"
sv:Sc/MyScorer3/OnlyIncludeParticlesNamed = 3 "neutron" "gamma" "proton"
sv:Sc/MyScorer3/OnlyIncludeParticlesFromComponentOrSubComponentsOf = 2
    "Target1" "Target2"
b:Sc/MyScorer3/IncludeEventID           = "True"
b:Sc/MyScorer3/IncludeTrackID           = "True"
s:Sc/MyScorer3/IfOutputFileAlreadyExists = "Increment"
b:Sc/MyScorer3/IncludeTimeOfFlight      = "True"

s:Sc/MyScorer4/OutputFile                       =
    "FLASK_LaBrZPlusSurface_PS_${SEED}"
s:Sc/MyScorer4/OutputType                       = "ASCII"
b:Sc/MyScorer4/OutputAfterRun           = "True"
s:Sc/MyScorer4/Quantity                         = "PhaseSpace"
s:Sc/MyScorer4/Surface                          = "Labr/ZPlusSurface"
sv:Sc/MyScorer4/OnlyIncludeParticlesNamed = 3 "neutron" "gamma" "proton"
sv:Sc/MyScorer4/OnlyIncludeParticlesFromComponentOrSubComponentsOf = 2
    "Flask1" "Flask2"
b:Sc/MyScorer4/IncludeEventID           = "True"
b:Sc/MyScorer4/IncludeTrackID           = "True"
s:Sc/MyScorer4/IfOutputFileAlreadyExists = "Increment"
b:Sc/MyScorer4/IncludeTimeOfFlight      = "True"

s:Sc/MyScorer5/OutputFile                       =
    "FLASK_LaBrOuterCurvedSurface_PS_${SEED}"
s:Sc/MyScorer5/OutputType                       = "ASCII"
b:Sc/MyScorer5/OutputAfterRun           = "True"
s:Sc/MyScorer5/Quantity                         = "PhaseSpace"
s:Sc/MyScorer5/Surface                          = "Labr/OuterCurvedSurface"
sv:Sc/MyScorer5/OnlyIncludeParticlesNamed = 3 "neutron" "gamma" "proton"
sv:Sc/MyScorer5/OnlyIncludeParticlesFromComponentOrSubComponentsOf = 2
    "Flask1" "Flask2"
b:Sc/MyScorer5/IncludeEventID           = "True"
b:Sc/MyScorer5/IncludeTrackID           = "True"
s:Sc/MyScorer5/IfOutputFileAlreadyExists = "Increment"
b:Sc/MyScorer5/IncludeTimeOfFlight      = "True"
```

Listing 2: Example of TOPAS simulation code used to generate phase-space and header files which were then used to calculate the energy deposition of prompt γ-rays at the surface of the detector. The kinetic energy, position, particle type and other quantities of neutrons, protons and γ-ray particles originating from the targets and scored on the surface of the detector (flat z-surface and curved surface of the cylinder) generated phase-space files which were then used to calculate the energy deposition. In this code, the 1M $CuSO_4$ solution was being simulated.

```
i:Ts/NumberOfThreads     = 0
i:Ts/Seed                                = ${SEED}


#************************** WORLD
s:Ge/World/Material      = "Air"
d:Ge/World/HLX                   =  1 m
d:Ge/World/HLY                   =  1 m
d:Ge/World/HLZ                   =  1.5 m
b:Ge/World/Invisible     = "FALSE"


#************************** BEAM = PHASESPACE SOURCE
b:So/MySource/LimitedAssumePhotonIsNewHistory = "true"
s:So/MySource/Type = "PhaseSpace"
s:So/MySource/Component = "World"
s:So/MySource/PhaseSpaceFileName =
    "/path/to/phasespace/file/TARGET_LaBrOuterCurvedSurface_PS_${SEED}"
i:So/MySource/PhaseSpaceMultipleUse = 2

#************************** TARGET
###TARGET COPPER 63
#isotope Cu63
i:Is/Cu63/Z                                      = 29
i:Is/Cu63/N                                      = 63
d:Is/Cu63/A                                      = 62.929597 g/mole
#element Cu63
s:El/ElCu63/Symbol                               = "ElCu63"
sv:El/ElCu63/IsotopeNames                = 1 "Cu63"
uv:El/ElCu63/IsotopeAbundances  = 1 100.
#Material Cu63
sv:Ma/MatCu63/Components                 =1 "ElCu63"
uv:Ma/MatCu63/Fractions                  = 1 1
d:Ma/MatCu63/Density                     = 8.96 g/cm3

s:Ge/Target/Type                 = "TsCylinder"
s:Ge/Target/Material             = "MatCu63"
s:Ge/Target/Parent               = "World"
dc:Ge/Target/HL                  = 1.5 cm
dc:Ge/Target/RMax                = 4.75 mm
dc:Ge/Target/TransX              = 0. m
dc:Ge/Target/TransY              = 0. m
dc:Ge/Target/TransZ              = -1.2 m
dc:Ge/Target/RotX                = 90. deg
dc:Ge/Target/RotY                = 0. deg
dc:Ge/Target/RotZ                = 0. deg
sc:Ge/Target/DrawingStyle        = "Solid"
sc:Ge/Target/Color                       = "yellow"

###TARGET YTTRIUM 89
#isotope Y89
i:Is/Y89/Z                                               = 39
i:Is/Y89/N                                               = 89
```

```
d:Is/Y89/A                                              = 88.90584 g/mole
#element Y89
s:El/ElY89/Symbol                                 = "ElY89"
sv:El/ElY89/IsotopeNames                  = 1 "Y89"
uv:El/ElY89/IsotopeAbundances    = 1 100.
#Material Y89
sv:Ma/MatY89/Components                   =1 "ElY89"
uv:Ma/MatY89/Fractions                    = 1 1
d:Ma/MatY89/Density                       = 4.472 g/cm3

###TARGET PHOSPHORUS 31
#isotope P31
i:Is/P31/Z                                              = 15
i:Is/P31/N                                              = 16
d:Is/P31/A                                              = 30.973762 g/mole
#element P31
s:El/ElP31/Symbol                                 = "ElP31"
sv:El/ElP31/IsotopeNames                  = 1 "P31"
uv:El/ElP31/IsotopeAbundances    = 1 100.
#Material P31
sv:Ma/MatP31/Components                   =1 "ElP31"
uv:Ma/MatP31/Fractions                    = 1 1
d:Ma/MatP31/Density                       = 1.82 g/cm3


#************************** SCINTILLATOR
s:Ge/Scint/Type                   = "TsBox"
s:Ge/Scint/Parent                 = "World"
s:Ge/Scint/Material               = "ScintMat"
sv:Ma/ScintMat/Components         = 2 "Hydrogen" "Carbon"
uv:Ma/ScintMat/Fractions          = 2 0.08474 0.91526
d:Ma/ScintMat/Density             = 1.032 g/cm3
dc:Ge/Scint/HLX                   = 2.5 mm
dc:Ge/Scint/HLY                   = 5 cm
dc:Ge/Scint/HLZ                   = 5 cm
dc:Ge/Scint/TransX                = 20 cm
dc:Ge/Scint/TransY                = 0. m
dc:Ge/Scint/TransZ                = -1.20 m
dc:Ge/Scint/RotX                  = 45. deg
dc:Ge/Scint/RotY                  = 0. deg
dc:Ge/Scint/RotZ                  = 0. deg
sc:Ge/Scint/DrawingStyle          = "Solid"
sc:Ge/Scint/Color                       = "magenta"


#************************** ALUMINIUM CASING AROUND DETECTOR
s:Ge/Alu/Type                     = "TsCylinder"
s:Ge/Alu/Material                 = "Aluminum"
s:Ge/Alu/Parent                   = "World"
dc:Ge/Alu/HL                      = 44.9 mm
dc:Ge/Alu/RMax                    = 43.2 mm
dc:Ge/Alu/TransX                  = 26 cm
dc:Ge/Alu/TransY                  = 0. m
```

```
dc:Ge/Alu/TransZ                = -1.2 m
dc:Ge/Alu/RotX                  = 0. deg
dc:Ge/Alu/RotY                  = 90 deg
dc:Ge/Alu/RotZ                  = 0. deg
sc:Ge/Alu/DrawingStyle  = "FullWireFrame"
sc:Ge/Alu/Color                 = "blue"

#************************** LABR DETECTOR
s:Ge/LaBr/Type                          = "TsCylinder"
s:Ge/LaBr/Material                      = "LaBrMat"
sv:Ma/LaBrMat/Components        = 2 "Lanthanum" "Bromine"
uv:Ma/LaBrMat/Fractions         = 2 0.3669 0.6331
d:Ma/LaBrMat/Density            = 5.08 g/cm3
s:Ge/LaBr/Parent                        = "Alu"
dc:Ge/LaBr/HL                           = 41.9 mm
dc:Ge/LaBr/RMax                         = 40.2 mm
dc:Ge/LaBr/TransX               = 0. m
dc:Ge/LaBr/TransY               = 0. m
dc:Ge/LaBr/TransZ               = 0. m
dc:Ge/LaBr/RotX                 = 0. deg
dc:Ge/LaBr/RotY                 = 0. deg
dc:Ge/LaBr/RotZ                 = 0. deg
sc:Ge/LaBr/DrawingStyle         = "Solid"
sc:Ge/LaBr/Color                        = "red"


#************************** LEAD SHIELD
s:Ge/LeadShield/Type                    = "TsBox"
s:Ge/LeadShield/Parent                  = "World"
s:Ge/LeadShield/Material                = "Lead"
dc:Ge/LeadShield/HLX                    = 41.9 mm
dc:Ge/LeadShield/HLY                    = 40.2 mm
dc:Ge/LeadShield/HLZ                    = 3 cm
dc:Ge/LeadShield/TransX                 = 26 cm
dc:Ge/LeadShield/TransY                 = 0. m
dc:Ge/LeadShield/TransZ                 = -1.05 m
dc:Ge/LeadShield/RotX                   = 0. deg
dc:Ge/LeadShield/RotY                   = 0. deg
dc:Ge/LeadShield/RotZ                   = 0. deg
sc:Ge/LeadShield/DrawingStyle   = "Solid"
sc:Ge/LeadShield/Color                  = "grey"


#************************** SCORER
s:Sc/MyEdepScorer/OutputFile
                                                =
    "Edep_TARGET_LaBrOuterCurvedSurface_${SEED}"
s:Sc/MyEdepScorer/OutputType
                                                = "ASCII"
b:Sc/MyEdepScorer/OutputAfterRun
                                                = "True"
s:Sc/MyEdepScorer/Quantity
                                                        = "TsEnergyDeposit"
```

```
154 sv:Sc/MyEdepScorer/OnlyIncludeIfParticleOrAncestorNamed
                        = 1 "gamma"
155 s:Sc/MyEdepScorer/Component
                                                = "LaBr"
156 s:Sc/MyEdepScorer/IfOutputFileAlreadyExists
                                  = "Increment"
157 b:Sc/MyEdepScorer/IncludeTimeOfFlight
                                       = "True"
```

Listing 3: Example of TOPAS simulation code used to calculate the energy deposition of γ-ray particles. In this example the energy deposition of γ-rays originating from the outer curved surface of the detector was calculated for each phase-space file corresponding to the kinetic energy at that point in space-time. The time-stepped energy deposition was measured using an in-house Geant4 macro. In this code, the 1M $CuSO_4$ solution was being simulated.

```
1  // Scorer for TsEnergyDeposit
2  //
3  // ********************************************************************
4  // *                                                                  *
5  // *                                                                  *
6  // * This file was obtained from Topas MC Inc under the license       *
7  // * agreement set forth at http://www.topasmc.org/registration       *
8  // * Any use of this file constitutes full acceptance of              *
9  // * this TOPAS MC license agreement.                                 *
10 // *                                                                  *
11 // ********************************************************************
12 //
13
14 #include "TsEnergyDeposit.hh"
15
16 #include "TsTrackInformation.hh"
17
18 #include "G4PSDirectionFlag.hh"
19 #include "G4VProcess.hh"
20
21 TsEnergyDeposit::TsEnergyDeposit(TsParameterManager* pM,
       TsMaterialManager* mM, TsGeometryManager* gM, TsScoringManager* scM,
       TsExtensionManager* eM,
22                           G4String scorerName, G4String quantity, G4String
                                 outFileName, G4bool isSubScorer)
23                          : TsVNtupleScorer(pM, mM, gM, scM, eM,
                               scorerName, quantity, outFileName,
                               isSubScorer)
24 {
25     //SetSurfaceScorer();
26         pM->SetNeedsSteppingAction();
27
28         fNtuple->RegisterColumnF(&fEnergyDeposit, "EnergyDeposit", "MeV");
29         //fNtuple->RegisterColumnF(&fWeight, "Weight", "");
30         //fNtuple->RegisterColumnI(&fPType, "PDG");
31     //fNtuple->RegisterColumnI(&fTrackID_Current, "TrackID");
32     //fNtuple->RegisterColumnI(&fEventID, "EventID");
33
34     fTrackID_Current = 1;
35     fTrackID_Past = 1;
36 }
37
38
39 TsEnergyDeposit::~TsEnergyDeposit() {;}
40
41
42 G4bool TsEnergyDeposit::ProcessHits(G4Step* aStep,G4TouchableHistory*)
43 {
44     if (!fIsActive) {
45         fSkippedWhileInactive++;
46         return false;
47     }
48
```

```
49      ResolveSolid(aStep);
50
51      G4double edep = aStep->GetTotalEnergyDeposit();
52
53
54          fEnergyDeposit += edep;
55
56
57      return true;
58  }
59
60  void TsEnergyDeposit::UserHookForEndOfEvent()
61  {
62      fNtuple->Fill();
63      fEnergyDeposit = 0.;
64  }
```

Listing 4: Source file of the macro extension read in by the TOPAS energy deposition simulations which was used to calculate time-stepped energy deposition.

```
1  //
2  // ********************************************************************
3  // *                                                                  *
4  // *                                                                  *
5  // * This file was obtained from Topas MC Inc under the license       *
6  // * agreement set forth at http://www.topasmc.org/registration       *
7  // * Any use of this file constitutes full acceptance of              *
8  // * this TOPAS MC license agreement.                                 *
9  // *                                                                  *
10 // ********************************************************************
11 //
12
13 #ifndef TsEnergyDeposit_hh
14 #define TsEnergyDeposit_hh
15
16 #include "TsVNtupleScorer.hh"
17
18 class TsEnergyDeposit : public TsVNtupleScorer
19 {
20 public:
21     TsEnergyDeposit(TsParameterManager* pM, TsMaterialManager* mM,
          TsGeometryManager* gM, TsScoringManager* scM, TsExtensionManager*
          eM,
22                 G4String scorerName, G4String quantity, G4String
                       outFileName, G4bool isSubScorer);
23
24     virtual ~TsEnergyDeposit();
25
26     G4bool ProcessHits(G4Step*,G4TouchableHistory*);
27     void UserHookForEndOfEvent();
28
29 private:
30         // Output variables
31         G4float fEnergyDeposit;
32         G4float fWeight;
33         G4int fPType;
34     G4int fTrackID_Current;
35     G4int fTrackID_Past;
36     G4int fEventID;
37 };
38 #endif
```

Listing 5: Header file of the macro extension read in by the TOPAS energy deposition simulations which was used to calculate time-stepped energy deposition.

```
1 EnergyDeposition = [Gamma_Curved_DetectorSurface;
      Gamma_ZPlane_Detector_Surface];
2 a = -0.69335;
3 b = 0.367334;
4 Sigma = (a + b*sqrt(EnergyDeposition*1000))/1000;
5 Esize = size(EnergyDeposition, 1);
6 smearing = Sigma .* randn(Esize, 1);
7 SmearedEnergyGamma_CuSO4_1M = EnergyDeposition + smearing;
```

Listing 6: Example MATLAB code for the smearing of the energy deposition on the $LaBr_3$:Ce detector surface as obtained in TOPAS simulation.

.2 Further Liquid Target Enhancement Plots

.2.1 $CuSO_4$

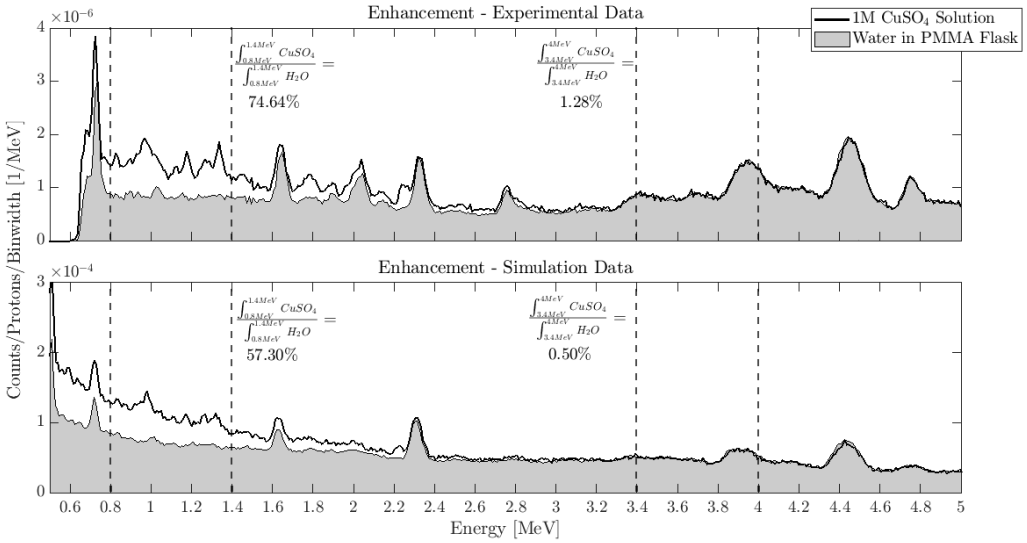

Plot of the experimental (top) and simulation (bottom) results of the 1M $CuSO_4$ solution vs water in the energy deposition range of 0.5 to 5 MeV. The vertical lines represent the enhancement range (0.8 to 1.4 MeV) and statistical fluctuation range (3.4 to 4 MeV). The associated enhancement and fluctuation is labelled on the plot.

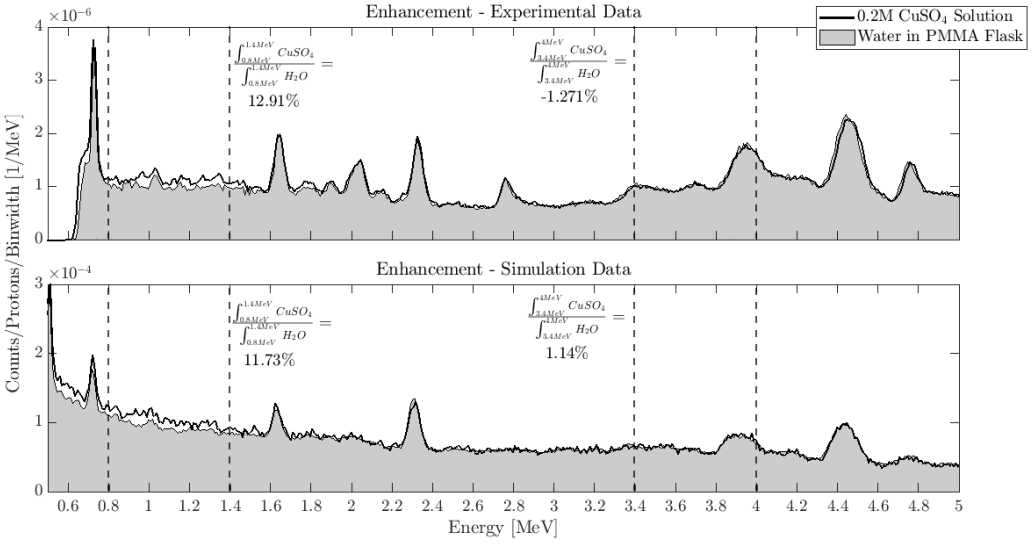

Plot of the experimental (top) and simulation (bottom) results of the 0.2M $CuSO_4$ solution vs water in the energy deposition range of 0.5 to 5 MeV. The vertical lines represent the enhancement range (0.8 to 1.4 MeV) and statistical fluctuation range (3.4 to 4 MeV). The associated enhancement and fluctuation is labelled on the plot.

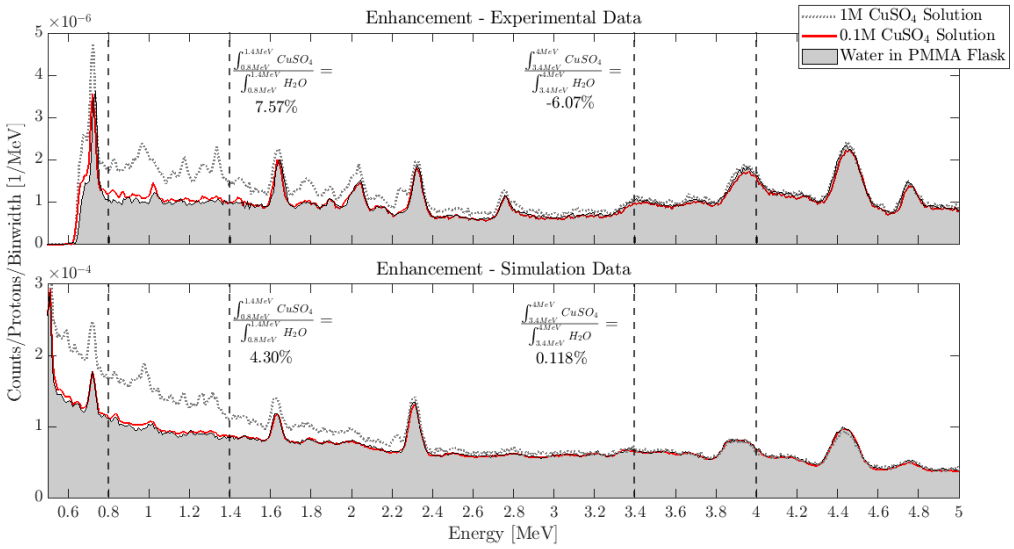

Plot of the experimental (top) and simulation (bottom) results of the 0.1M $CuSO_4$ solution vs water in the energy deposition range of 0.5 to 5 MeV. The vertical lines represent the enhancement range (0.8 to 1.4 MeV) and statistical fluctuation range (3.4 to 4 MeV). The associated enhancement and fluctuation is labelled on the plot.

.2.2 $Y(NO_3)_3$

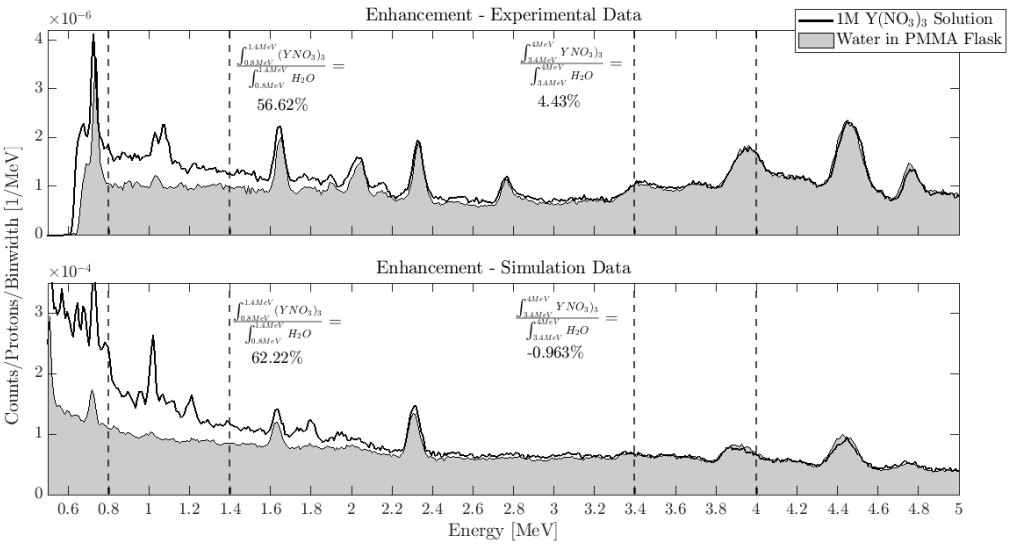

Plot of the experimental (top) and simulation (bottom) results of the 1M $Y(NO_3)_3$ solution vs water in the energy deposition range of 0.5 to 5 MeV. The vertical lines represent the enhancement range (0.8 to 1.4 MeV) and statistical fluctuation range (3.4 to 4 MeV). The associated enhancement and fluctuation is labelled on the plot.

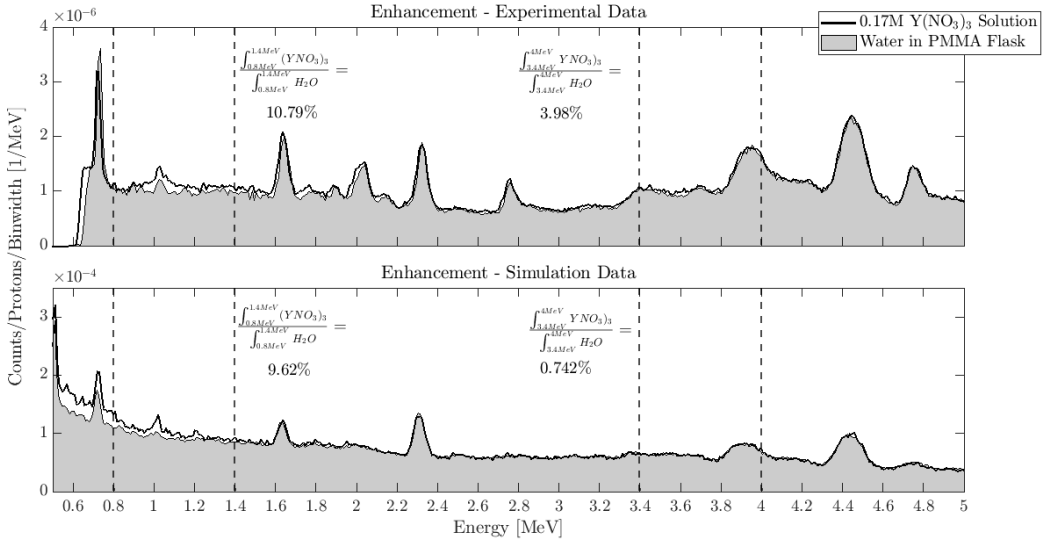

Plot of the experimental (top) and simulation (bottom) results of the 0.17M $Y(NO_3)_3$ solution vs water in the energy deposition range of 0.5 to 5 MeV. The vertical lines represent the enhancement range (0.8 to 1.4 MeV) and statistical fluctuation range (3.4 to 4 MeV). The associated enhancement and fluctuation is labelled on the plot.

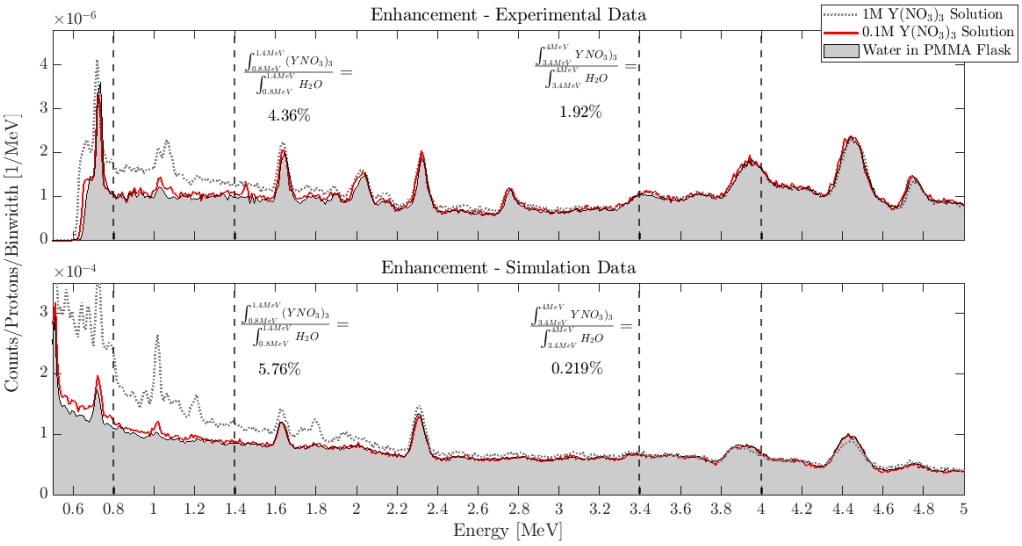

Plot of the experimental (top) and simulation (bottom) results of the 0.1M $Y(NO_3)_3$ solution vs water in the energy deposition range of 0.5 to 5 MeV. The vertical lines represent the enhancement range (0.8 to 1.4 MeV) and statistical fluctuation range (3.4 to 4 MeV). The associated enhancement and fluctuation is labelled on the plot.

.2.3 NaH_2PO_4

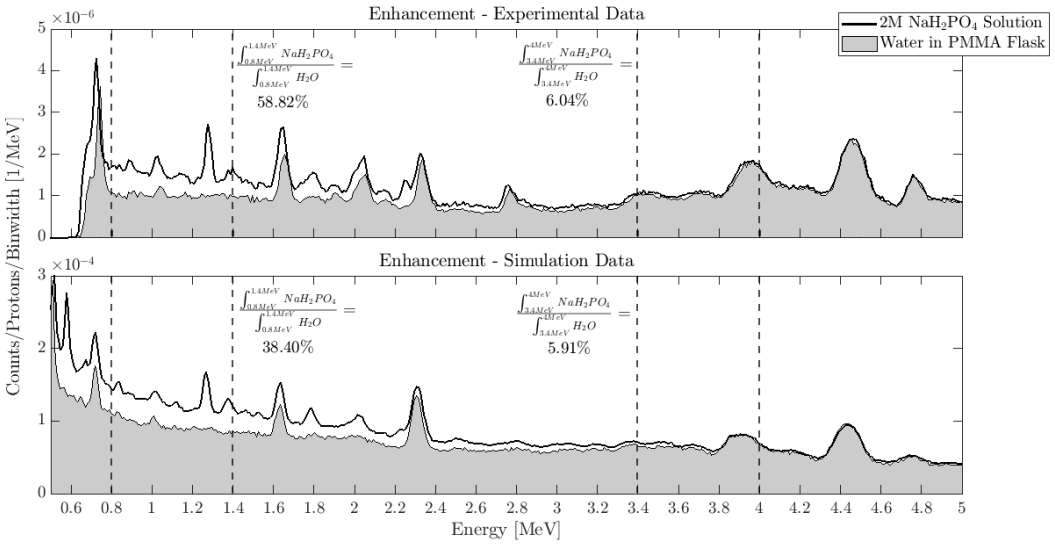

Plot of the experimental (top) and simulation (bottom) results of the 2M NaH_2PO_4 solution vs water in the energy deposition range of 0.5 to 5 MeV. The vertical lines represent the enhancement range (0.8 to 1.4 MeV) and statistical fluctuation range (3.4 to 4 MeV). The associated enhancement and fluctuation is labelled on the plot.

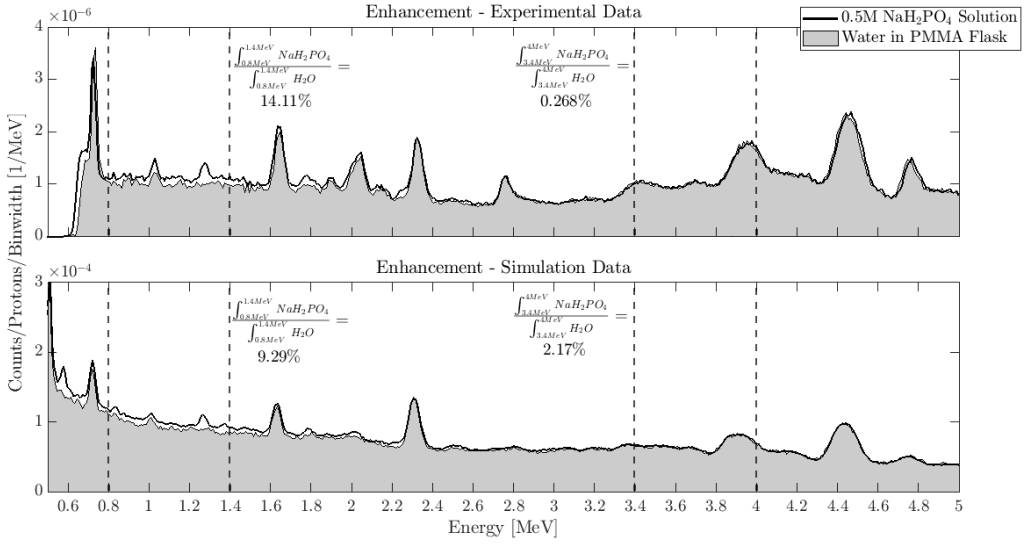

Plot of the experimental (top) and simulation (bottom) results of the 0.5M NaH_2PO_4 solution vs water in the energy deposition range of 0.5 to 5 MeV. The vertical lines represent the enhancement range (0.8 to 1.4 MeV) and statistical fluctuation range (3.4 to 4 MeV). The associated enhancement and fluctuation is labelled on the plot.

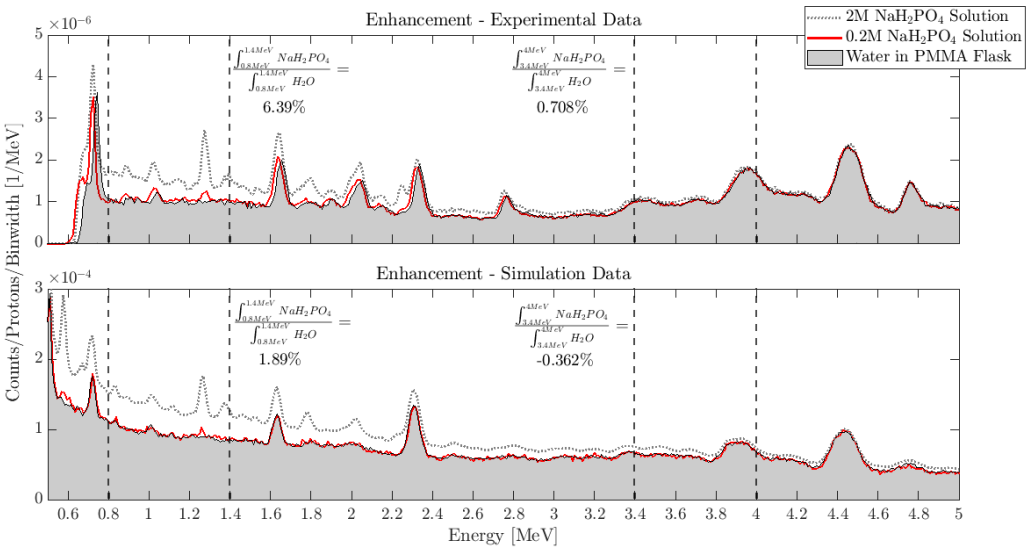

Plot of the experimental (top) and simulation (bottom) results of the 0.2M NaH_2PO_4 solution vs water in the energy deposition range of 0.5 to 5 MeV. The vertical lines represent the enhancement range (0.8 to 1.4 MeV) and statistical fluctuation range (3.4 to 4 MeV). The associated enhancement and fluctuation is labelled on the plot.